
Creation of α -oxygen during the N_2O decomposition over Mn-ZSM-5

*Vorming van α -zuurstof species tijdens de afbraak
van N_2O over Mn-ZSM-5*

(met een samenvatting in het Nederlands)

Proefschrift

ter verkrijging van de graad van doctor aan de Universiteit Utrecht
op gezag van de rector magnificus, prof. dr. J. C. Stoof,
ingevolge het besluit van het college voor promoties in het openbaar te
verdedigen op maandag 29 October 2007 des middags te 2.30 uur

door

Cornel Daniel Radu

geboren op 28 mei 1979 te Ramnicu Sarat, Roemenie

Promotor: prof. dr. ir. B. M. Weckhuysen

Co-promotor: dr. F. M. F. de Groot

Creation of α -oxygen during the N_2O decomposition over Mn-ZSM-5

The research described in this PhD thesis was financially supported by
NWO - CW and NRSCC.

ISBN-13: 978-90-393-4655-6

Cover lay-out by Daniel Radu

Drukkerij Ponsen en Looijen, Wageningen

Content

Chapter 1	General Introduction	1
Chapter 2	Characterization Techniques	25
Chapter 3	Catalytic Decomposition of Nitrous Oxide on Mn-ZSM-5: Linking the 18500 cm ⁻¹ UV-vis Band to Catalytic Activity	47
Chapter 4	On the Nature of Manganese in Mn-S-1 and Mn-ZSM-5 Zeolites	75
Chapter 5	High-resolution Mn K edge X-ray absorption of Mn- ZSM-5 systems	99
Chapter 6	A. Summary	124
	B. Conclusions	126
	C. Look into the Future	131
	D. Samenvatting	135
	Dankwoord	139
	Curriculum Vitae	141
	List of Publications and Presentations	142

1

General Introduction

1.1. Catalysis

Starting with the industrial revolution from the early 19th century our society has been characterized by an increasing demand of materials and energy. Catalysis has played and still plays a primordial role in the production of materials, chemicals and energy carriers. A catalytic process is the acceleration of a chemical reaction by means of a substance, called a **catalyst** that is itself not consumed by the overall reaction. A catalyst decreases the activation energy of a chemical reaction. **Catalysis** is a concept based on the usage of a catalyst in order to produce useful materials and also to eliminate or minimize waste. Catalysis is divided into three fields: biocatalysis, homogeneous catalysis and heterogeneous catalysis. Biocatalysis involves the use of natural catalysts, mainly in the form of **enzymes**, which are proteins integrated in living organisms that are capable of catalyzing chemical reactions. During the natural evolution of the hosting organisms, enzymes became a specialized catalyst material capable of high turnover frequency (TOF) numbers combined with close to 100% selectivity to the desired product. A typical enzyme can be characterized by an active part - several amino acids connected to e.g. a transition metal - that is able to bind a substrate, and then carries out the reaction and a 'spectator part' formed by linear chains of amino acids that fold in a specific manner to produce a three-dimensional structure which has a role in the selection of the substrate. Homogeneous and heterogeneous catalysts are built on similar principles, where often the active centre is a transition metal surrounded by organic ligands (homogeneous catalysts), inorganic matrices (heterogeneous catalysts) or a combination of both.

1.2. Zeolites and their functionalization

Zeolites are the aluminosilicate members of the family of microporous solids known as “molecular sieves”. The term molecular sieve refers to a particular property of these materials, i.e. the ability to selectively sort molecules based primarily on the size exclusion principle. This is due to a very regular pore structure of molecular dimensions. The maximum size of the molecular or ionic species that can enter the pores of a zeolite is controlled by the diameters of the channels. The primary building units are Si tetrahedrons that are interconnected via Si-O-Si oxygen bridges and combined they form multi-dimensional structures and different shapes, channels and cavities, giving a wide range of porous materials. Zeolite MFI is characterized by a two-dimensional channel system formed by two types of 10-membered ring channels, one straight and one type sinusoidal, being situated perpendicular to the first type (Figure 1). ZSM-5 zeolite (Zeolite Synthesis Mobile Five) possesses the MFI topology, in which Al^{3+} replaces a Si^{4+} ion without affecting the zeolite structure. This replacement induces a negative charge into the framework, which can be compensated by extra-framework cations, such as Na^+ and NH_4^+ . The presence of these cations gives the ZSM-5 zeolite a new property i.e. the property to exchange the compensated cations present in zeolite channels with other cations, including transition metal ions.

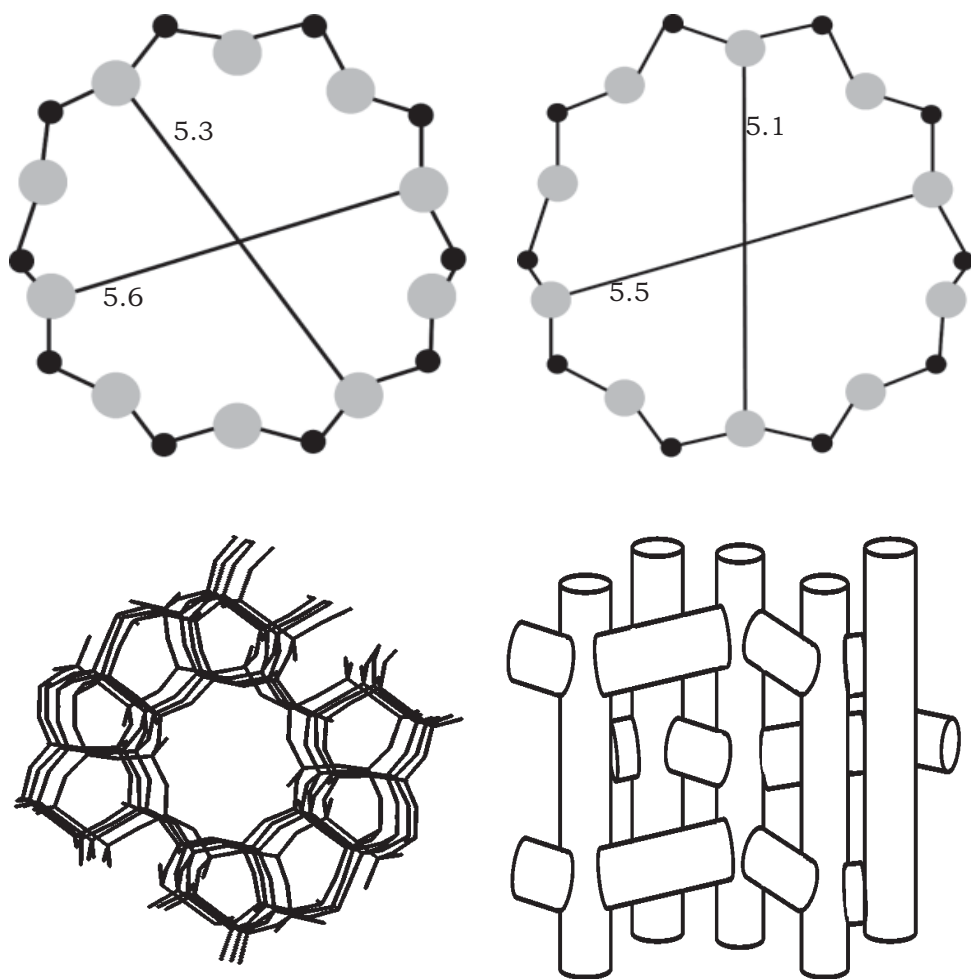


Figure 1. Schematic representation of the channel structure of MFI (top), and a view along zeolite channels (bottom left) together with a scheme of the channel alignment (bottom right).

There are two distinctive procedures in which a transition metal ion can be introduced into a zeolite: by means of a direct synthesis method or by using a post-synthesis treatment. These methods will be explained bellow. They are schematically presented in Figure 2.

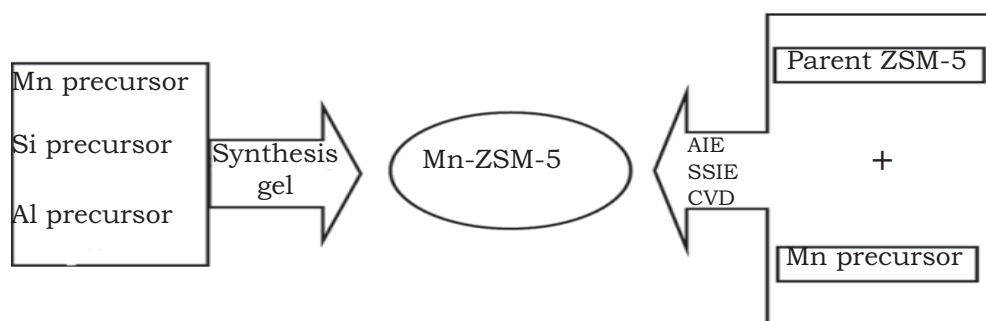


Figure 2. Scheme of the preparation of Mn-ZSM-5 catalyst materials. The left side presents the direct synthesis method, while the post synthesis method is shown in the right panel of the scheme and includes Aqueous Ion Exchange (AIE), Solid State Ion Exchange (SSIE) and Chemical Vapour Deposition (CVD).

1.2.1. Direct synthesis

The direct synthesis method involves the introduction of the transition metal ion during zeolite preparation. The most common way to synthesize a zeolite is the hydrothermal method. In this method a gel is prepared by adding a silica source, organic template and sodium hydroxide to an aqueous solution in which a salt of aluminium and the desired transition metal are dissolved. The obtained gel is introduced into an autoclave and heated for a number of days yielding a crystalline zeolite material. A more detailed presentation of this procedure is discussed in **Chapter 4** of this PhD - thesis, where the optimisation of the preparation of Mn-silicalite-1 and Mn-ZSM5 synthesis is discussed.

1.2.2. Post synthesis via ion exchange

The post-synthesis method is based on the ion exchange properties of the zeolite. This preparation method consists of exchanging the compensating cations with chosen mono- or multivalent cations. Three different routes can be distinguished.

Aqueous ion exchange (AIE) consists in immersing and stirring the zeolite crystals in an aqueous solution of the desired metal salt. The most

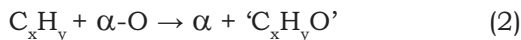
common salts used in this method are sulphates, nitrates, carbonates and chlorinated salts. In some cases, salts with complexing ligands, such as acetate, are used. By using different pH values or different concentration solutions the exchange degree can be varied. After the ion exchange procedure, the zeolite is filtrated and washed in order to remove the excess salt solution followed by an activation step. This method is presented in more detail in **Chapter 3** of this PhD - thesis.

In this PhD-thesis, we did not make use of two alternative exchange routes, namely Solid State Ion Exchange (SSIE) and Chemical Vapour Deposition (CVD). SSIE is based on the ion exchange properties of the zeolite using a solid metal precursor that is subjected to a thermal treatment. The CVD technique is based on the sublimation properties of the metal precursor.

1.3. Fe and Cu in ZSM-5 zeolites

1.3.1. Fe-ZSM-5 Zeolite

In 1993, Panov et al. [1] published a paper in which Fe-ZSM-5 materials were used in order to oxidize benzene to phenol in one step at room temperature. They demonstrate that Fe-ZSM-5 can generate an α -oxygen form similar to Fe-based enzymes, with the difference that Fe-ZSM-5 uses N_2O instead of O_2 as the source of oxygen. This discovery led to an increased number of studies to identify the active phase and the nature of α -oxygen in Fe-ZSM-5 and related systems [2-11]. Studies show that α -oxygen is able to yield single oxygenated compounds, using starting materials including alkanes [12] and halogen-aromatic compounds [13]. In addition, Fe-ZSM-5 has been used to create C-H bonds as is the case for the methane to benzene conversion [14,15]. The selective oxidation studies mentioned above also revealed that Fe-ZSM-5 is active in the N_2O decomposition reaction [4,7,16-24]. Finally, this activity towards nitrogen containing compounds makes Fe-ZSM-5 a suitable candidate for the removal of nitrogen oxides by Selective Catalytic Reduction (SCR) [19,25-29]. The general reaction scheme of the active site in Fe-ZSM-5 zeolite can be represented by two interconnected reactions:



In reaction (1), a nitrous oxide, N_2O , NO or NO_2 is stripped of its oxygen at an α -vacancy (α) thereby creating an α -oxygen site ($\alpha-O$). In reaction (2), the α -oxygen site subsequently oxidises a hydrocarbon. For the oxidation of methane reaction (1) provides the α -oxygen sites needed for the selective oxidation and in SCR de- NO_x the α -vacancies are created by reducing the α oxygen sites by hydrocarbons.

1.3.2. Cu-ZSM-5 Zeolite

In 1986, Iwamoto et al. [30] presented Cu-ZSM-5 as a material, which is characterized by a very high and stable catalytic activity for the NO decomposition reaction. Motivated by the high catalytic activity of these materials, numerous research groups have studied the nature of the Cu sites and their redox chemistry [31-42]. As expected, these materials are also active in the catalytic decomposition of N_2O [43,44]. In 1998, Chajar et al. [45] presented the oxidation of C_3H_8 on Cu-ZSM-5 using NO or O_2 as an oxygen source. The series of hydrocarbons which were oxidized using Cu-ZSM-5 combined with different oxygen sources includes phenol [46], or methane [47]. Studies using different characterisations techniques identified the active centre to be a bis-(μ -oxo) complex [48-50] similar to that present in Cu-based enzymes.

1.4. Catalytic reactions with Mn oxides and Mn-based zeolites

1.4.1. Manganese oxides

In Table 1 we present an overview of the reactions in which manganese oxides are used as catalyst components. One of the reactions is the decomposition of ozone over manganese oxides. Ozone decomposition is of practical significance because ozone is a toxic substance and can be found

in human environments including aircraft cabins, near photocopiers, laser printers, sterilizers, etc. Most of the research involving O_3 decomposition is reported in the patent literature. However, some studies involving the identification of the ozone decomposition mechanism can be found [51-54]. In 2004 Einaga et al. used the ozone decomposition reaction for the catalytic oxidation of benzene [55]. A similar concept was used also by Oyama et al. for acetone oxidation [56]. Since the recognition of N_2O as a greenhouse effect gas in the 1990's numerous research projects were started in order to identify an active material for N_2O removal. The first report for N_2O decomposition over manganese compounds dates from 1958 [57]. Since then, the activity of manganese oxides was tested by different groups [58,59]. However, due to the low surface area of the oxides, different compounds that contain manganese atoms were also investigated, including supported manganese oxides on activated carbon [60], manganese - exchanged zeolites [61] or hydrotalcite - based compounds [62,63]. For the same reasons NO_x removal started to be of interest. Although V_2O_5/TiO_2 is a very effective industrial catalyst for NO_x removal, the high temperature conditions at which this catalyst performs (> 623 K) has led to the development of new catalyst materials that can operate at lower temperatures. Manganese oxides proved to perform excellent in the selective catalytic reduction of NO with molecules, such as NH_3 [64,65] at 393 K, CH_4 [66-68] at temperature ranging from 300 K to 800 K or CO [69] at the same temperature ranges.

Table 1. Overview of the reactions in which manganese oxides are used as catalyst component.

Catalyst material	Catalytic Reaction	Reference
Mn/polyoxometalate	Selective epoxidation of alkenes	[70]
NiMnO ₃ ilmenite NiMn ₂ O ₄ -spinel	Complete oxidation of hydrocarbons	[71,72]
Fe,Co/S-1 doped with Mn	Conversion of syn-gas to light olefins	[73]
Mn ₂ O ₃ /H-ZSM-5	Low-temperature deep oxidation of dichloromethane and trichloroethylene	[74]
MnO/K ₂ O/Fe/S-2	Production of light alkenes from CO ₂ hydrogenation	[75]
MnO _x /Co/TiO ₂	Fischer-Tropsch synthesis	[76,77]

1.4.2. Mn-based zeolites

The discovery that bis-(μ -oxo) manganese dimers and tetramers are important in Photosystem II, led to increased research in homogeneous catalysis in which bis-(μ -oxo) manganese dimers were synthesized. The majority of these complexes are used in fine chemical processes due to their affinity to catalyse selective oxidation reactions on complex substrates. The high activity of bis-(μ -oxo) manganese dimers can be explained by the fact that manganese can change easily between its oxidation state. As a result, in a bis-(μ -oxo) centre one or both manganese atoms are capable of changing their oxidation state. In order to introduce these active centres also in the field of heterogeneous catalysis two routes can be distinguished:

- encapsulation of an active Mn complex in zeolite cages and/or channels [78];
- connecting these active complexes to a functionalized silica material [79].

These approaches are based on the concept of single site catalysis, in other words, the reaction takes place only on one active centre – in most cases a transition metal, while the other components stabilize the structure or perform other functions such as the selection of the substrates. With the discovery of TS-1 [80] it was shown that this single site catalysts can be obtained by the introduction of the transition metal into the zeolite framework. In follow-up studies, manganese ions were introduced in different zeolite matrices in a similar manner. Table 2 presents an overview of Mn-based materials and also the catalytic reactions in which these materials are active.

Table 2. Overview of the reactions in which manganese-containing zeolites are used as catalysts.

Zeolite matrix	Synthesis procedure	Catalytic Reaction	Reference
MCM-41	Chemical vapour deposition	Oxidation of trans-stilbene to trans-stilbene oxide	[81]
		Diphenylmethane to benzophenone	[82]
MCM-41	Impregnation	Vapour phase oxidation of isopropylbenzene	[83,84]
MCM-41	Chemical vapour deposition	Oxidation of CO to CO ₂	[85]
AlPO-4	Hydrothermal	Etherification	[86]
SBA-15	Hydrothermal	Oxidation ethylbenzene with tert butyl hydroperoxide	[87]
A/X/Y/USY/Beta/ ZSM-5	Ion exchange	SO ₂ oxidation	[88]
X	Ion exchange	Oxidative conversion of methane to C ₂ hydrocarbons	[89]

1.5. Biological analogies

In this section the potential analogies of metal ions in ZSM5 with biological systems are discussed. This is particularly of interest because the work on α -oxygen in Fe-ZSM-5 has been closely linked with mono-oxygenases in the papers of Panov and co-workers [90]. We will discuss here the biological analogs of Fe-ZSM-5, Cu-ZSM-5 and Mn-ZSM-5. Fe-ZSM-5 and Cu-ZSM-5 have been linked to Methane Mono-Oxygenase (MMO) enzymes and we will investigate a potential similarity between Mn-ZSM-5 and the oxygen evolving complex in Photosystem II (PSII). The metal ion doped ZSM-5 systems can be considered as heterogeneous catalyst systems that are biomimetic to these enzymes. A much wider field of research is the synthesis of inorganic analogs of the active sites of enzymes, attempting to mimic the local metal-cluster binding of the enzyme [91]. These coordination systems are much closer to the biological systems concerning their detailed local structure. A difference between enzymes and these coordination complex analogs is that the enzyme has additional functionalities, one of which is to control what molecules are able to reach the active site. In this sense the analogy with heterogeneous catalysts is closer, where in our case the ZSM-5 zeolite structure takes the role of controlling access to the active sites, though this control is far less detailed and advanced than in enzymes. Methane Mono-Oxygenases (MMO) are enzymes that are able to activate the C-H bond in methane [92]. This implies that these catalysts possess a very reactive oxygen atom, similar to α -oxygen. MMO breaks up molecular oxygen and uses this to react with the activated methane molecule. There are two forms of MMO: the soluble form (sMMO) and the particulate form (pMMO). The extended research made in this field led to the determination of the active center for the soluble form of the MMO. Using spectroscopic studies, the active site in sMMO was identified to be a di-iron center bridged by exogenous hydroxide and acetate ligands, being further coordinated by four glutamate residues, two histidine residues and a water molecule (Figure 3) [93].

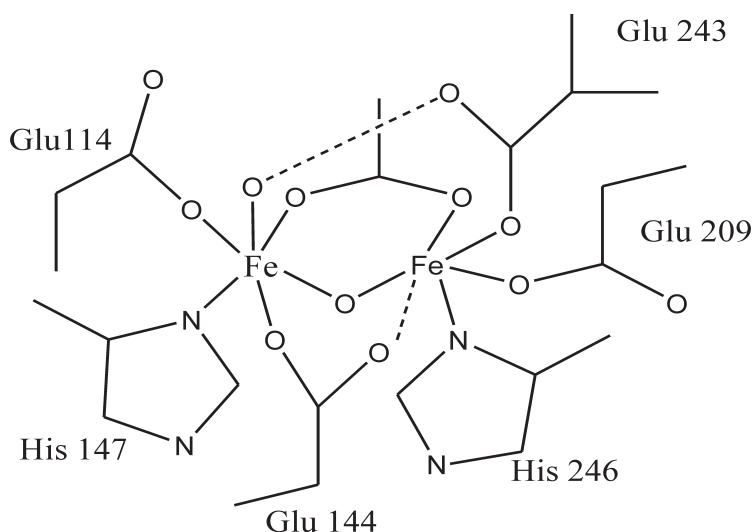


Figure 3. The Fe₂ active site of sMMO from Rosenzweig et al. [93].

Being non-soluble, the pMMO form presents a much more challenging problem to resolve. Using electron paramagnetic resonance (EPR) two overlapping signals were uncovered. One signal was attributed to a normal type 2 copper centers, the second signal being the contribution of a copper cluster. In these experiments it was observed that the intensity of the copper cluster correlates with the pMMO activity. This observation led to a preliminary hypothesis that the copper cluster represents the active site of the pMMO [94, 95]. Rosenzweig et al. [96, 97] revealed using anomalous (or resonant) X-ray diffraction and X-ray absorption spectroscopy (XAS) that pMMO has indeed two main copper centers, one being a mononuclear copper center (Figure 4b), while the above mentioned copper cluster is actually a di-nuclear copper center (Figure 4a). Until now, the identity of the active catalytic center remains a major question.

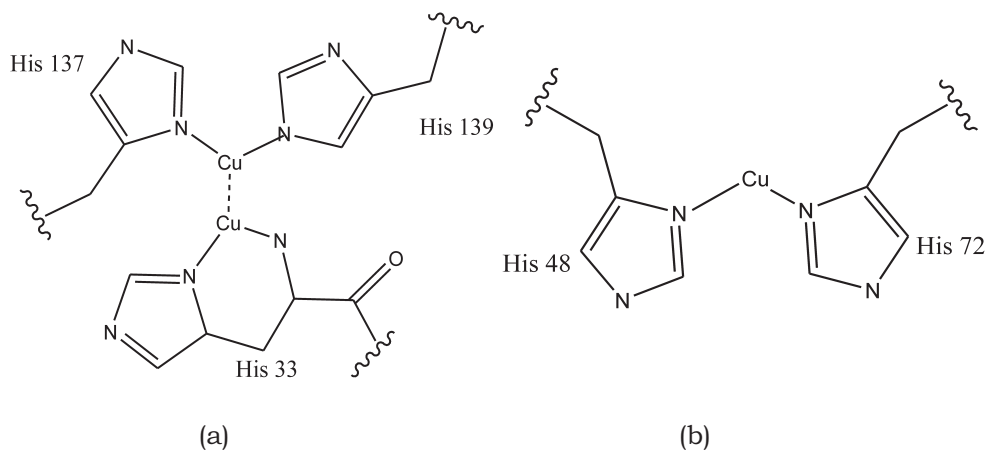


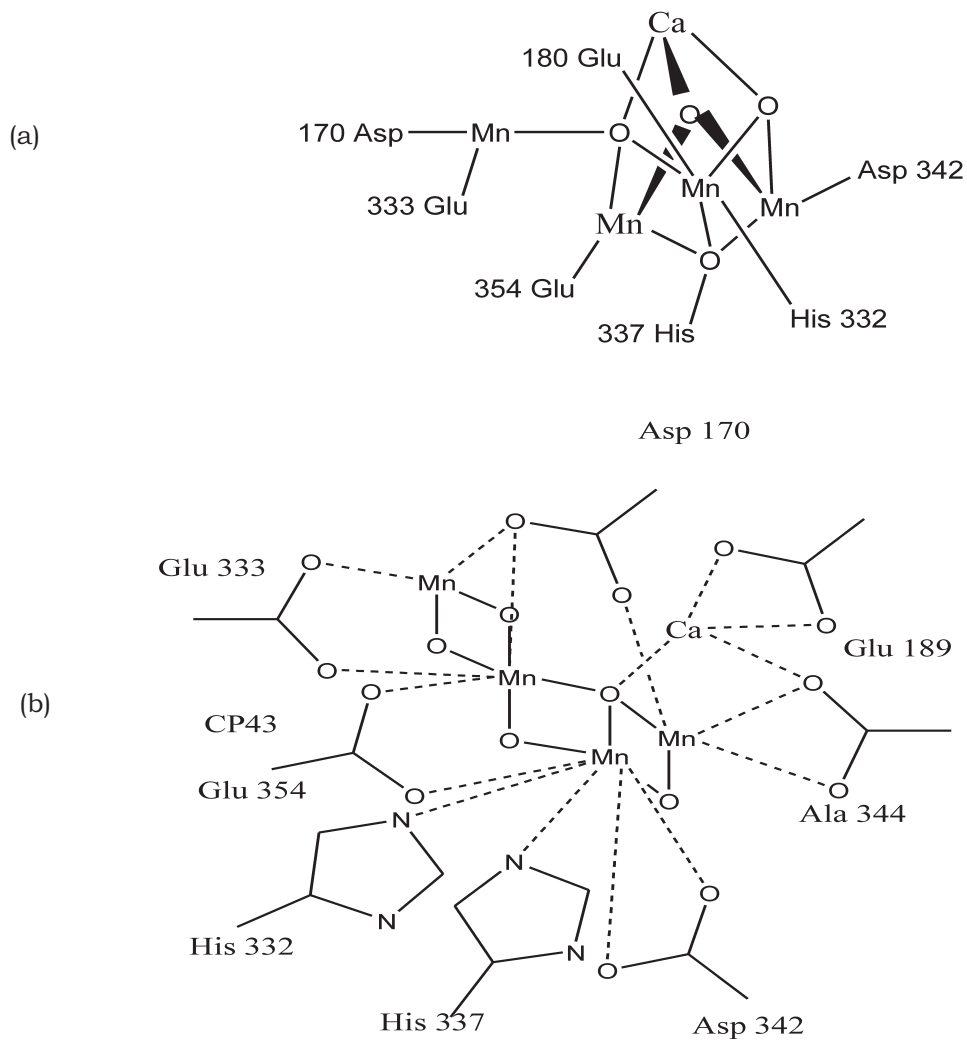
Figure 4. The (a) Cu_2 and (b) Cu_1 active site of pMMO from Rosenzweig et al. [96, 97].

Although the active centers of these enzymes are formed by different transition metals, both forms can be characterized by an equivalent behavior during the catalytic reaction. This behavior consists in an increase in the oxidation state of the transition metal from 1 to 2 in the case of Cu-PmmO [97] and from 2 to 3 for Fe-sMMO [93] during the formation of α -oxygen, and the decrease to the initial values of the oxidation state once the α -oxygen is removed. These di-iron and di-copper centers have raised the interest of chemists in the synthetic analogues of these structures. Great progress was made in the preparation of the diamond-shaped $[\text{M}_2(\mu\text{-O})_2]^{n+}$ core structures using different ligands and iron, copper or manganese as metal ions [91]. These structures have been demonstrated to be active in oxidations of various organic functionalities in reactions of biological relevance. The synthesis of these complexes has opened a new chapter in bioinorganic field, and showed that the bio-mimetic studies can have an important role in understanding the original metalloenzyme systems.

We will now turn to a potential biological analog of Mn-ZSM-5. Here we focus on the oxygen-evolving complex in Photosystem II (PS II). PS II is present in green plants and it is capable to catalyze a light-driven water oxidation reaction to generate molecular oxygen. The active center is

proposed to be composed of 4 oxygen-bridged manganese atoms coupled to a Ca atom. From XRD, also called Protein X-ray Crystallography (PX), one has concluded that the active site is organized in a cubane-like Mn_3CaO_4 cluster, with each metal ion in this cluster having three- μ -oxo bridges connected to another Mn ion by a mono- μ -oxo bridge [98, 101]. At this moment this structure is at the center of a fierce debate, where it is used as evidence to show that essentially all metal clusters in enzymes as determined from PX are wrong, or at least can not expected to be correct without additional evidence. The reason being the enormously high X-ray dose that has to be used to determine the protein structure. Radiation damage is a widely studied phenomenon in PX, but it has recently been shown that in typical PX data of PSII the radiation damage is low enough to assume that the enzyme remains intact, but high enough to destroy the metal site [102]. The reason that the metal site is much more fragile to X-rays is that (1) exactly there the X-ray absorption is up to 100 times higher due to the presence of heavier elements, coupled to the fact (2) that the metal valence is in a delicate balance, which can be completely destroyed by the X-ray. This implies that while the bulk of the enzyme can be accurately determined by PX, exactly at the metal sites the structure can be significantly modified due to the valence changes of the metal ions and the corresponding reaction to it by the liganding complexes. The structure that is ultimately determined can not be expected to bear much resemblance to the original structure. This phenomenon has been nicely demonstrated for PSII [102, 103], where one has used EXAFS to track the changes from the undamaged site to the site that is determined in PX (by exposing PSII to ever higher X-ray doses). In addition, they have used polarized EXAFS to determine to non-damaged structure of PSII. The polarized EXAFS data leaves a number of options for the active site that have been bound to protein fragments and fine tuned with the existing PX data. Because of radiation damage of the PX data, it is not clear that the protein fragments found from PX are correct, which leaves some uncertainty at this moment. In addition, a recent theoretical study [104] indicates that there exist a number of isomeric structures of similar energy that can transfer into each other. Crystallization then can cause preferential freezing-out of a certain structure. This is an intrinsic problem for all measurements on protein crystals, i.e. both for PX and polarized

EXAFS.



Extrapolating the results from Yano on X-ray doses and the resulting drastic damage to the metal site, it can be extrapolated that all PX data that uses similar X-ray doses will have metal sites that are likely drastically damaged. Thus while the overall protein structure will be correct, the metal sites as determined from PX can not be trusted without additional evidence.

Table 3. The comparison between the three enzyme systems with ZSM-5 systems. Columns 2 and 6 give the metal atom and cluster size, columns 3 and 7 the redox couple in the reaction, and columns 4 and 8 the main neighbor atom.

Enzyme	Metal	Redox	Main Ligand	Zeolite	Metal	Redox	Main Ligand
sMMO	Fe_2	2-3	O	FeZSM5	Fe_n	2-3	O
pMMO	Cu_2	1-2	N	CuZSM5	Cu_n	1-2	O
PSII	Mn_4	3-4	O	Mn-ZSM-5	Mn_n	?	?

In Table 3 we compare some characteristic aspects of the active sites in the enzymes compared to the ZSM-5 systems. The metal clusters in ZSM-5 have been indicated with Fe_n , where n depends on the preparation method and reaction conditions and where typically a range of values of n will occur simultaneously. In case of iron, there is an analogy in the redox couple and the oxygen liganding. In addition, it is claimed that the Fe_2 complex occurs frequently in Fe-ZSM-5 [90]. In case of Cu-ZSM-5, a major difference is the important role of nitrogen neighbors for pMMO that differs drastically from Cu-ZSM-5. In the case of Mn-ZSM-5 remains to be established the characteristics of the active sites in order to be compared with his correspondent in the PSII enzyme.

Scope of the PhD - thesis and outline

This PhD - thesis entitled 'Creation of α -oxygen during the N_2O decomposition over Mn-ZSM-5' intends to contribute to the knowledge on (1) the preparation methods capable to mimic active cores of different enzymes, and (2) the combination of spectroscopic tools capable to reveal the electronic and geometric structure of the active centre. These spectroscopic tools are selected in order to offer a wide range of information including bulk information, chemical composition combined with details on the oxidation state and site geometry of the active centre. The fundamental basis for the spectroscopic techniques used is presented in **Chapter 2**.

As presented in this introduction chapter there are two principal methods of preparation - a post synthesis method and a direct synthesis method. **Chapter 3** is based on the post synthesis method, where Mn-ZSM-5 materials were prepared using an ion exchange procedure. Catalytic testing indicates the generation of α -oxygen species obtained using the N_2O decomposition reaction. The reactivity of these α -oxygen species is studied using the NO oxidation reaction as a test reaction.

Chapter 4 deals with the preparation of Mn-MFI materials using hydrothermal synthesis method. Both Mn-S-1 and Mn-ZSM-5 materials are prepared and tested for catalytic activity for N_2O decomposition. Mn-S-1 presents an average activity of about 1.5% but without the generation of α -oxygen species, while Mn-ZSM-5 shows a lower activity. During NO exposure, Mn-S-1 is active in a disproportionation reaction, having 75% selectivity towards N_2O .

Chapter 5 presents a detailed and complete analysis for high-resolution Mn K edge X-ray absorption spectra for sample prepared as mentioned in Chapter 3 and 4. Using this technique, we can determine the electronic and structural characteristics of the manganese sites function of preparation procedure and function of the nature of gas treatments.

A summary, general conclusions and a look into the future are presented in **Chapter 6**.

References

- [1] G. A. Sheveleva; A. S. Kharitonov; G. I. Panov; V. I. Sobolev; N. L. Razdobarova; Y. A. Paukshtis; V. N. Romannikov, *Petroleum Chemistry*, 33, **(1993)**, 516.
- [2] G. Centi; S. Perathoner; R. Arrigo; G. Giordano; A. Katovic; V. Pedula, *Appl. Catal. A Gen.*, 307, **(2006)**, 30.
- [3] G. Centi; S. Perathoner; F. Pino; R. Arrigo; G. Giordano; A. Katovic; V. Pedula, *Catal. Today*, 110, **(2005)**, 211.
- [4] E. Hensen; Q. J. Zhu; P. H. Liu; K. J. Chao; R. A. Van Santen, *J. Catal.*, 226, **(2004)**, 466.
- [5] G. Centi; G. Giordano; P. Fejes; A. Katovic; K. Lazar; J. B. Nagy; S. Perathoner; F. Pino. Active and spectator iron species in Fe/MFI catalysts for benzene selective hydroxylation with N₂O. In *Recent Advances in the Science and Technology of Zeolites and Related Materials, Pts A - C*, 2004; Vol. 154; pp 2566.
- [6] E. Selli; I. Rossetti; D. Meloni; F. Sini; L. Forni, *Appl. Catal. A Gen.*, 262, **(2004)**, 131.
- [7] W. X. Zhang; M. J. Jia; C. L. Zhang; L. H. Zhang; T. H. Wu; T. Sun; H. Yahiro; M. Iwamoto, *Chemical Journal of Chinese Universities-Chinese*, 19, **(1998)**, 1112.
- [8] S. Perathoner; F. Pino; G. Centi; G. Giordano; A. Katovic; J. B. Nagy, *Top. Catal.*, 23, **(2003)**, 125.
- [9] D. Meloni; R. Monaci; V. Solinas; G. Berlier; S. Bordiga; I. Rossetti; C. Oliva; L. Forni, *J. Catal.*, 214, **(2003)**, 169.
- [10] V. I. Sobolev; K. A. Dubkov; E. A. Paukshtis; L. V. Pirutko; M. A. Rodkin; A. S. Kharitonov; G. I. Panov, *Appl. Catal. A Gen.*, 141, **(1996)**, 185.
- [11] A. S. Kharitonov; T. N. Aleksandrova; G. I. Panov; V. I. Sobolev; G. A. Sheveleva; E. A. Paukshtis, *Kinet. Catal.*, 35, **(1994)**, 270.
- [12] K. A. Dubkov; V. I. Sobolev; G. I. Panov, *Kinet. Catal.*, 39, **(1998)**, 72.
- [13] A. Costine; T. O'sullivan; B. K. Hodnett, *Catal. Today*, 99, **(2005)**, 199.
- [14] B. M. Weckhuysen; D. J. Wang; M. P. Rosynek; J. H. Lunsford, *J. Catal.*, 175, **(1998)**, 338.
- [15] B. M. Weckhuysen; D. J. Wang; M. P. Rosynek; J. H. Lunsford, *J.*

Catal., 175, **(1998)**, 347.

[16] J. Perez-Ramirez; E. V. Kondratenko, *Chem. Commun.*, **(2003)**, 2152.

[17] Y. Tian; E. Ogawa; A. Ikuo; T. Shishido; Q. H. Zhang; Y. Wang; K. Takehira; S. Hasegawa, *Chem. Lett.*, 35, **(2006)**, 544.

[18] I. Melian-Cabrera; S. Espinosa; J. C. Groen; B. Van De Linden; F. Kapteijn; J. A. Moulijn, *J. Catal.*, 238, **(2006)**, 250.

[19] T. Nobukawa; M. Yoshida; S. Kameoka, *J. Phys. Chem. B*, 108, **(2004)**, 4071.

[20] A. Lebail; H. Duroy; J. L. Fourquet, *Mater. Res. Bull.*, 23, **(1988)**, 447.

[21] M. Haneda; M. Shinriki; Y. Nagao; Y. Kintaichi; H. Hamada, *Bull. Chem. Soc. Jpn.*, 76, **(2003)**, 2329.

[22] T. Nobukawa; S. Tanaka; S. Ito; K. Tomishige; S. K. Kimio; K. Kunimori, *Catal. Lett.*, 83, **(2002)**, 5.

[23] Q. Zhu; B. L. Mojet; R. A. J. Janssen; E. J. M. Hensen; J. Van Grondelle; P. Magusin; R. A. Van Santen, *Catal. Lett.*, 81, **(2002)**, 205.

[24] W. M. H. Sachtler; R. A. V. Santen; El-M.El-Malki, *J. Catal.*, 196, **(2000)**, 212.

[25] A. A. Battiston; J. H. Bitter; D. C. Koningsberger, *J. Catal.*, 218, **(2003)**, 163.

[26] K. Krishna; G. B. F. Seijger; C. M. Van Den Bleek; M. Makkee; G. Mul; H. P. A. Calis, *Catal. Lett.*, 86, **(2003)**, 121.

[27] C. Pophal; T. Yogo; K. Yamada; K. Segawa, *Appl. Catal. B Envir.*, 16, **(1998)**, 177.

[28] G. Centi; F. Vazzana, *Catal. Today*, 53, **(1999)**, 683.

[29] C. Pophal; T. Yogo; K. Tanabe; K. Segawa, *Catal. Lett.*, 44, **(1997)**, 271.

[30] M. Iwamoto; H. Furukawa; Y. Mine; F. Uemura; S. Mikuriya; S. Kagawa, *J. Chem. Soc. Chem. Commun.*, **(1986)**, 1272.

[31] Y. Teraoka; C. Tai; H. Ogawa; H. Furukawa; S. Kagawa, *Appl. Catal. A Gen.*, 200, **(2000)**, 167.

[32] C. Dossi; A. Fusi; S. Recchia; R. Psaro; G. Moretti, *Micropor. Mesopor. Mat.*, 30, **(1999)**, 165.

[33] G. L. Price; V. Kanazirev; D. F. Church, *J. Phys. Chem.*, 99, **(1995)**, 864.

[34] B. I. Palella; L. Lisi; R. Pirone; G. Russo; M. Notaro, *Kinet. Catal.*, 47,

(2006), 728.

[35] R. Pirone; P. Ciambelli; B. Palella; G. Russo. A kinetic study of NO decomposition on Cu-ZSM5. In *Oxide-Based Systems at the Crossroads of Chemistry*, 2001; Vol. 140; pp 377.

[36] B. Moden; P. Da Costa; D. K. Lee; E. Iglesia, *J. Phys. Chem. B*, 106, **(2002)**, 9633.

[37] P. Da Costa; B. Moden; G. D. Meitzner; D. K. Lee; E. Iglesia, *Phys.Chem. Chem. Phys.*, 4, **(2002)**, 4590.

[38] B. Moden; P. Da Costa; D. K. Lee; E. Iglesia, *Abstracts of Papers of the American Chemical Society*, 223, **(2002)**, U648.

[39] B. Moden; P. Da Costa; B. Fonfe; D. K. Lee; E. Iglesia, *J. Catal.*, 209, **(2002)**, 75.

[40] X. Solans-Monfort; V. Branchadell; M. Sodupe, *J. Phys. Chem. B*, 106, **(2002)**, 1372.

[41] P. T. Fanson; M. W. Stradt; W. N. Delgass; J. Lauterbach, *Catal. Lett.*, 77, **(2001)**, 15.

[42] B. Ganemi; E. Bjornbom; J. Paul, *Appl. Catal. B Envir.*, 17, **(1998)**, 293.

[43] P. Ciambelli; A. Di Benedetto; R. Pirone; G. Russo, *Chem. Eng. Sci.*, 54, **(1999)**, 4521.

[44] P. Ciambelli; A. Di Benedetto; R. Pirone; G. Russo, *Chem. Eng. Sci.*, 54, **(1999)**, 2555.

[45] Z. Chajar; M. Primet; H. Praliaud, *J. Catal.*, 180, **(1998)**, 279.

[46] Z. Gabelica; S. Valange, *Micropor. Mesopor. Mat.*, 30, **(1999)**, 57.

[47] M.H.Groothaert; P. J. Smeets; B. F. Sels; P. A. Jacobs; R. A. Schoonheydt, *J. Am. Chem. Soc.*, 127, **(2005)**, 1394.

[48] M. H. Groothaert; K. Lievens; J. A. Van Bokhoven; A. A. Battiston; B. M. Weckhuysen; K. Pierloot; R. A. Schoonheydt, *Chem. Phys. Chem.*, 4, **(2003)**, 626.

[49] M. H. Groothaert; J. A. Van Bokhoven; A. A. Battiston; B. M. Weckhuysen; R. A. Schoonheydt, *J. Am. Chem. Soc.*, 125, **(2003)**, 7629.

[50] M. H. Groothaert; K. Pierloot; A. Delabie; R. A. Schoonheydt, *Phys. Chem. Chem. Phys.*, 5, **(2003)**, 2135.

[51] T. S. Oyama; R. Radhakrishnan, *J. Catal.*, 199, **(2001)**, 282.

[52] T. S. Oyama; R. Radhakrishnan, *J. Phys. Chem. B*, 105, **(2001)**, 4245.

- [53] T. S. Oyama; W. Li; G. V. Gibbs, *J. Am. Chem. Soc.*, 120, **(1998)**, 9041.
- [54] T. S. Oyama; C. Heising; W. Zhang, *Appl. Catal. B Envir.*, 14, **(1997)**, 117.
- [55] H. Einaga; S. Futamura, *J. Catal.*, 227, **(2004)**, 304.
- [56] X. Yan; R. Corey; K. L. Yong; T. S. Oyama, *J. Phys. Chem.*, 109, **(2005)**, 17587.
- [57] L. Rheaume; P. G., *J. Phys. Chem.*, 63, **(1958)**, 264.
- [58] A. Cimino; R. Bosco; V. Indovina; M. Schiavello, *J. Catal.*, 5, **(1966)**,
- [59] T. Yamashita; A. Vannice, *J. Catal.*, 161, **(1996)**, 254.
- [60] S. A. Carabineiro; F. B. Fernandes; J. S. Vital; A. M. Ramos; I. M. Fonseca, *Appl. Catal. B Envir.*, 59, **(2005)**, 181.
- [61] Y. J. Li; J. N. Armor, *Appl. Catal. B Envir.*, 1, **(1992)**, L21.
- [62] L. Obalova; K. Jiratova; F. Kovanda; K. Pacultova; Z. Lacny; Z. Mikulova, *Appl. Catal. B Envir.*, 60, **(2005)**, 289.
- [63] L. Obalova; K. Jiratova; F. Kovanda; M. Valaskova; J. Balabanova; K. Pacultova, *J. Mol. Catal. A Chem.*, 248, **(2006)**, 210.
- [64] G. Marban; T. Valdes-Solis; A. B. Fuertes, *J. Catal.*, 226, **(2004)**, 138.
- [65] G. Qi; R. T. Yang, *J. Catal.*, **(2003)**, 434.
- [66] A. T. Bell; A. W. Aylor; L. J. Lobree; J. A. Reimer, *J. Catal.*, 170, **(1997)**, 390.
- [67] M. C. Campa; D. Pietrogiacomini; S. Tuti; G. Ferraris; V. Indovina, *Appl. Catal. B Envir.*, 18, **(1998)**, 151.
- [68] W. M. H. S. Sachtler, Qi, *Appl. Catal. B Envir.*, 42, **(2003)**, 393.
- [69] N. B. Stankova; M. S. Khristova; D. R. Mehandjiev, *J. Colloid Interface Sci.*, 241, **(2001)**, 439.
- [70] R. Ben-Daniel; L. Weiner; R. Neumann, *J. Am. Chem. Soc.*, 124, **(2002)**, 8788.
- [71] D. Mehandjiev; E. Zchecheva; G. Ivanov; R. Ioncheva, *Appl. Catal. A Gen.*, 167, **(1998)**, 277.
- [72] D. Mehandjiev; A. Naydenov; G. Ivanov, *Appl. Catal. A Gen.*, 206, **(2001)**, 13.
- [73] D. Das; G. Ravichandran; D. K. Chakrabarty, *Catal. Today*, 36, **(1997)**, 285.
- [74] J. I. G. Ortiz; R. L. Fonseca; U. Aurrekoerxea; J. R. G. Velasco, *J. Catal.*, 218, **(2003)**, 148.

- [75] L. Y. Xu; Q. X. Wang; D. B. Liang; X. Wang; L. W. Lin; W. Cui; Y. D. Xu, *Appl. Catal. A Gen.*, 173, **(1998)**, 19.
- [76] F. Morales; F. M. F. de Groot; P. Glatzel; E. Kleimenov; H. Bluhm; M. Havecker; A. Knop-Gericke; B. M. Weckhuysen, *J. Phys. Chem. B*, 108, **(2004)**, 16201.
- [77] F. Morales; O. L. J. Gijzeman; F. M. F. de Groot; B. M. Weckhuysen. *Stud. Surf. Sci. Catal.*, 147, **(2004)**, 271.
- [78] R. Ganesan; B. Viswanathan, *J. Mol. Catal. A Chem.*, 223, **(2004)**, 21.
- [79] F. S. Vinhado; C. M. C. Prado-Manso; H. C. Sacco; Y. Iamamoto, *J. Mol. Catal. A Chem.*, 174, **(2001)**, 279.
- [80] M. Taramasso; G. Perego; B. Notari, *U.S. Patent 4410501*, 1983.
- [81] V. Caps; S. C. Tsang, *Catal. Today*, 61, **(2000)**, 19.
- [82] Q. H. Zhang; Y. Wang; S. Itsuki; T. Shishido; K. Takehira, *J. Mol. Catal. A Chem.*, 188, **(2002)**, 189.
- [83] S. Vetrivel; A. Pandurangan, *Appl. Catal. A Gen.*, 264, **(2004)**, 243.
- [84] S. Vetrivel; A. Pandurangan, *J. Mol. Catal. A Chem.*, 227, **(2005)**, 269.
- [85] D. Gleeson; R. Burch; N. A. Cruise; S. C. Tsang, *NanoStructured Materials*, 12, **(1999)**, 1007.
- [86] H. Ren; F. Xin, *Catal. Commun.*, 7, **(2006)**, 848.
- [87] G. S. Kumar; M. Palanichamy; M. Hartmann; V. Murugesan, *Catal. Commun.*, 8, **(2007)**, 493.
- [88] J. Garcia-Martinez; D. Cazorla-Amoros; A. Linares-Solano, *Appl. Catal. B Envir.*, 47, **(2004)**, 203.
- [89] P. Kovacheva; N. Davidova, *React. Kinet. Catal. Lett.*, 53, **(1994)**, 277.
- [90] G. I. Panov, *CATTECH*, 4, **(2000)**, 18.
- [91] L. Que Jr; W. B. Tolman, *Angew. Chem. Int. Ed.*, 41, **(2002)**, 1114.
- [92] J. J. R. F. D. Silva; R. J. P. Williams *The biological chemistry of the elements: The inorganic chemistry of life*; Oxford University Press: Oxford, **2001**.
- [93] A. C. Rosenzweig; C. A. Frederick; S. J. Lippard; P. Nordlund, *Nature*, 366, **(1993)**, 537.
- [94] S. I. Chan; H. H. T. Nguyen; A. K. Shiemke; M. E. Lindstrom, *Bioinorganic Chemistry of Copper*, K. D. Karlin; Z. Tyeklar, Eds., Chapman & Hall, New York, **1993**, 184.
- [95] H. H. T. Nguyen; A. K. Shiemke; S. J. Jacobs; B. J. Hales; M. E.

Lindstrom; S. I. Chan, *J. Biol. Chem.*, 269, **(1994)**, 14995.

[96] R. L. Lieberman; A. C. Rosenzweig, *Nature*, 434, **(2005)**, 177.

[97] R. L. Lieberman; k. C. Kondapalli; D. B. Shrestha; A. S. Hakemian; S. M. Smith; J. Telser; J. Kuzelka; R. Gupta; A. S. Borovik; S. J. Lippard; B. M. Hoffman; A. C. Rosenzweig; T. L. Stemmler, *Inorg. Chem.*, 45, **(2006)**, 8372.

[98] K. N. Ferreira; T. M. Iverson; K. Maghlaoui; J. Barber; S. Iwata, *Science*, 303, **(2004)**, 1831.

[99] J. P. McEvoy; G. W. Brudvig, *Phys. Chem. Chem. Phys.*, 6, **(2004)**, 4754.

[100] I. J. Hewitt; J. K. Tang; N. T. Madhu; R. Clerac; G. Buth; C. E. Anson; A. K. Powell, *Chem. Commun.*, **(2006)**, 2650.

[101] E. M. Sproviero; J. A. Gascon; J. P. McEvoy; G. W. Brudvig; V. S. Batista, *Curr. Opin. Struct. Biol.*, 17, **(2007)**, 173.

[102] J. Yano; J. Kern; K.D. Irrgang; M.J. Latimer; U. Bergmann; P. Glatzel; Y. Pushkar; J. Biesiadka; B. Loll; K. Sauer; J. Messinger; A. Zouni; V. K. Yachandra, *PNAS*, 102, **(2005)**, 12047.

[103] J. Yano; J. Kern; K.D. Irrgang; M.J. Latimer; U. Bergmann; P. Glatzel; Y. Pushkar; J. Biesiadka; B. Loll; K. Sauer; J. Messinger; A. Zouni; V. K. Yachandra, *Science*, **(2006)**, 821.

[104] S. Petrie; R. Stranger; P. Gatt; R. J. Pace, *Chem. Eur. J.*, 13, **(2007)**, 5082.

Characterisation Techniques

The materials under study have been characterized by a number of techniques, using respectively X-rays, electrons and visible light as probing sources. In this chapter, a brief overview is given of the capabilities and limitations of the techniques that have been used throughout this PhD - thesis, respectively XAS, XRD, XRF, SEM, STEM-EELS and UV-vis DRS.

Table 1. Spectroscopic and microscopic techniques for studying Mn-ZSM-5 zeolites together with their spatial resolution as used in this thesis.

Spectros. technique	Oxid. state	Coord.	Spatial Resol.	Elem. Spec.	Comments
XANES	+	+	-*	+	Local symmetry
EXAFS	+/-**	+	-*	+	Local geometry
XRF	-	-	-*	+	High sensitivity
XRD	+/-**	-	-*	-	Crystal lattice
SEM	-	-	5 nm	-	Surface texture
TEM	-	-	0.2 nm	-	Crystal texture
EELS	+	-	0.5 nm	+	Local symmetry
UV-vis DRS	+	+	-*	-	Local symmetry

*XANES, EXAFS, XRF, XRD and UV-vis DRS have not been used as a spectro-microscopic technique.

** EXAFS and XRD derive the nearest neighbour distance, which in many cases can be correlated with the metal valence.

2.1. X-ray techniques

In the energy range of hard X-ray experiments (3-100 keV) three important processes are taking place:

1. Elastic, or Rayleigh-Thompson, scattering gives rise to interference effects in crystalline materials and is the basis for X-ray Diffraction (XRD).
2. Inelastic, or Compton, scattering is used to determine momentum distribution of electrons and is not used in this thesis.
3. The Photo-electric effect excites a core electron to an empty state. This is the basis for X-ray Absorption Spectroscopy (XAS). The decay of shallow core electrons to deeper core holes is the basis for X-Ray Fluorescence (XRF).

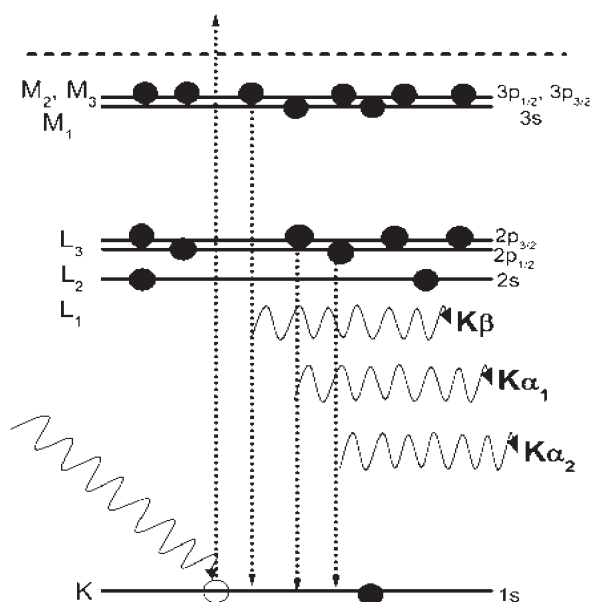
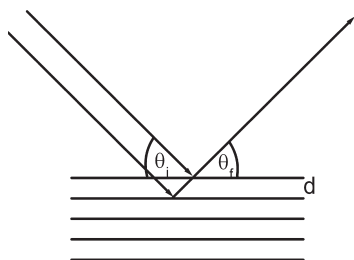


Figure 1. Indicated is the creation of a 1s core hole (K edge) and the subsequent emission of a fluorescence photon from the shallow L_{2,3} (Kα₁ and Kα₂) and M_{2,3} (Kβ) core states.

Figure 1 indicates the consequences of the photo-electronic effect, the excitation of a core electron in XAS and the subsequent decay of the core hole in XRF. XAS measures the excitation of a core electron to an empty state and as such probes the empty states. XRF tracks the various emission channels and as such measures the amount of core holes that are created. XRF is discussed in section 2.1.3, while XAS is discussed in section 2.1.4.

2.1.1. X-ray diffraction

X-ray Powder Diffraction (XRD) is an efficient analytical technique used to identify and characterize unknown crystalline materials [1]. Monochromatic x-rays are used to determine the interplanar spacing of materials. Samples are analysed as powders with grains in random orientations to insure that all crystallographic directions are “sampled” by the beam.



$$n\lambda = 2d\sin\theta \quad (\text{eq. 1})$$

When the Bragg conditions for constructive interference are fulfilled (see above and eq. 1), a peak is found. The x-ray pattern generated by this technique provides a structural fingerprint of the unknown system. Mixtures of crystalline materials can also be analysed and the relative peak heights may be used to obtain semi-quantitative estimates of abundances. A glancing x-ray beam may also be used to obtain structural information of thin films on surfaces.

2.1.2. Rietveld refinement

From XRD one can extract the cell parameters corresponding to the crystal structure of the sample. A method able to extract these parameters is the Rietveld refinement method, which uses a least squares approach to refine a theoretical line profile until it matches the measured profile. This theoretical line profile is created based on the peak shape, position, and peak width contribution. All these parameters are calculated as indicated below. When monochromatic X-ray sources are used, the convolution of the various effects has been found to result in a peak almost exactly Gaussian in shape. If this distribution is assumed then the contribution of a given peak to the profile y_i at position $2\theta_i$ is:

$$y_i = I \exp \left[-4 \ln \left(\frac{2}{H_k^2} \right) (2q_i - 2q_k)^2 \right] \quad (\text{eq. 2})$$

where H_k is the full width at half peak height (full-width half-maximum), $2\theta_k$ is the centre of the peak, and I_k is the calculated intensity of the peak (determined from the structure factor, the Lorentz factor, and multiplicity of the reflection). The width of the diffraction peaks is found to broaden at higher Bragg angles. This angular dependency was originally represented by

$$H_k^2 = U \tan^2 \theta_k + V \tan \theta_k + W \quad (\text{eq. 3})$$

where U , V and W are the half width parameters and may be refined during the fit. The principle of the Rietveld Method is to minimise a function M that represents the difference between a calculated profile $y(\text{calc})$ and the observed data $y(\text{obs})$. Rietveld defined such an equation as:

$$M = \sum_i W_i \left\{ y_i^{\text{obs}} - \frac{1}{c} y_i^{\text{calc}} \right\}^2 \quad (\text{eq. 4})$$

where W_i is the statistical weight and c is an overall scale factor such that $y^{\text{calc}} = cy^{\text{obs}}$ [2].

2.1.3. X-ray fluorescence

X-ray Fluorescence (XRF) is the emission of characteristic fluorescent X-rays from a material where a core hole has been created by high-energy X-rays or electrons. In electron microscopy, XRF is usually indicated as Energy Dispersive X-ray (EDX) analysis. The removal of a core electron renders the electronic structure of the excited atom unstable, and electrons in higher orbitals quickly fill the hole left behind, where the energy is released in the form of a photon. The emitted energy is equal to the energy difference of the two orbitals involved, implying that the material emits radiation, which has an energy characteristic of the atoms present. Each element has orbitals of characteristic energy. As indicated in Figure 1, the main XRF channels in 3d transition metals are $K\alpha$ and $K\beta$.

The fluorescent radiation can be analysed either by sorting the energies of the photons (energy-dispersive analysis) or by separating the wavelengths of the radiation (wavelength-dispersive analysis). Once sorted, the intensity of each characteristic radiation is related to the amount of each element in the material. XRF is a non-destructive analytical technique, and as a process control tool in many extractive and processing industries. In principle, the lightest element that can be analysed is beryllium ($Z = 4$), but due to instrumental limitations and low X-ray yields for the light elements, it is often difficult to quantify elements lighter than sodium ($Z = 11$). In this PhD thesis we consider Mn-ZSM-5 zeolite and the important elements are Mn, Si and Al. The ratios of these elements are determined with XRF that is a check to determine the Mn loading.

2.1.4. X-ray Absorption Spectroscopy

In this work we use X-ray Absorption Spectroscopy (XAS) to study the Mn K edge at ~6540 eV. XAS provides detailed information on the oxidation state and the coordination environment of the Mn ions [3-9]. Bond distances and coordination numbers can be determined with high precision and no long range ordering is required as in the case of XRD. Disadvantages are that advanced data-analysis is required to extract the information from the spectra and that only an average structure can be inferred, which is often a problem since different coordination environments and oxidation states can co-exist.

In XAS, the incoming X-ray photon is absorbed by a core that is excited to an empty state, either an 'excitonic state' at the edge or to the continuum. This process occurs if the energy of the X-ray photon is larger than the binding energy of the core electron, which implies that XAS is element specific. For excitation to continuum states the outgoing electron can be approximated as a (spherical) electron wave. When the photon energy is equal to the binding energy, a sharp rise in the absorption curve will be observed. This sharp rise is called the absorption edge (E_{edge}), illustrated in Figure 3a, for an isolated atom. When the atom is put into a matrix of surrounding atoms, for instance Mn in ZSM-5, the XAS spectrum is modulated by the neighbouring atoms (Figure 3b). The result is an absorption spectrum in which the total absorption exhibits a fine structure above the absorption edge. This fine structure is indicated as Extended X-ray Absorption Fine Structure (EXAFS) and is further discussed below.

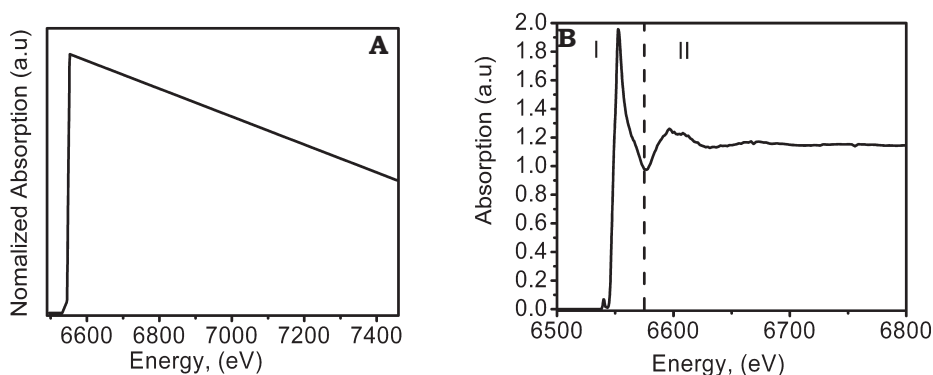


Figure 3. (A) X-ray absorption curve for an isolated atom. (B) Typical X-ray absorption spectrum: Absorption versus the energy, relative to the absorption edge (E_{edge}). I: The X-ray absorption near edge structure (XANES) and II: The Extended X-ray absorption fine structure (EXAFS).

Figure 3B indicates a manganese K edge of Mn-ZSM-5. This spectrum is usually divided into two parts:

- The region near the absorption edge, i.e. the X-ray Absorption Near Edge Structure (XANES)
- The EXAFS region, starting some 30 eV above the edge.

In case of metal K edges, the XANES region is further divided into a pre-edge structure and an edge structure. The pre-edge relates to a quadrupole transition from the 1s core state to an empty 3d state. The edge transition is a dipole transition to the lowest empty p-states. The quadrupole transition is ~ 100 times weaker than dipole transitions and as such yield only small pre-edge features [10]. The pre-edge peaks can be used to determine the coordination and the oxidation state of Mn. The absorption edge position can be determined in several ways, for example by the first maximum in the second derivative, the point halfway the edge jump or a characteristic feature in the edge. The choice is rather arbitrary as long as all related spectra are treated the same way.

The position of the pre-edge peaks and the edge position shift with the oxidation state of the manganese. When the oxidation state increases both the pre-edge and edge shift to higher energy. As is shown in Figure 4, the shift of the edge is larger (ca. 7 eV for $\text{Mn}^{2+} \rightarrow \text{Mn}^{4+}$) than the shift of the pre-edge (ca. 2 eV for $\text{Mn}^{2+} \rightarrow \text{Mn}^{4+}$). Thus, the difference between the edge

and pre-edge energy can be considered as an internal measure for the Mn oxidation state. The XANES part of the spectrum reflects the empty p-states of the Mn-ZSM-5 system.

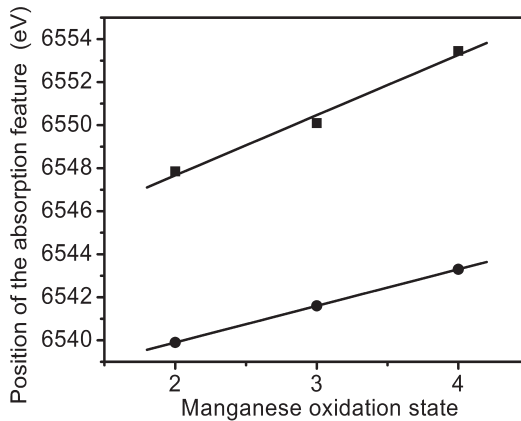


Figure 4: Energy positions of the pre-edge peak (1s → 3d) (●) and the absorption edge (■) versus the oxidation state.

2.1.5. EXAFS analysis

The EXAFS part contains all features observed in the spectrum starting at ~30 eV above the edge and higher. The modulation of the XAS spectrum can be effectively described by (single) scattering of the free electron on neighbouring atoms in the matrix. The electron wave function of the ejected electron is a superposition of the outgoing and backscattered electron wave. Depending on the phase difference, constructive and destructive interference takes place between the outgoing and the backscattered electron wave. The interference induces differences in the final state of the electron wave function as a function of the photon energy and thus modulates the absorption coefficient.

At energies of the incident X-ray beam higher than E_0 , the kinetic energy of the photoelectron is:

$$E_{kin} = h\nu - E_0 \quad (\text{eq. 5})$$

This photo-electron can be regarded as a spherical electronic wave, and the kinetic energy (E_{kin}) of the photoelectron determines the wavelength λ , defined as $2\pi/k$, where k is the photo-electron wave vector that is proportional to the square root of the kinetic energy:

$$k = \left[\left(\frac{8\pi^2 m}{h^2} \right) (h\nu - E_0) \right]^{1/2} \quad (\text{eq. 6})$$

Where m is the electron mass and h is Planck's constant. The XAS cross section (μ) is reformulated as a function of k . To better isolate the wiggles, the atomic cross section $\mu_0(k)$ is subtracted. This yields the EXAFS function $\chi(k)$, using:

$$\mu(k) = \mu_0(k) \{1 + \chi(k)\} \quad (\text{eq. 7})$$

Since there is usually more than one neighbouring atom around the absorber atom the $\chi(k)$ function is the sum of all waves resulting from the interferences of the electron wave between the absorber atom and all its neighbouring atoms. Atoms of the same type and with the same distance to the absorber atom are considered as one shell. The EXAFS function therefore consists of a summation over all shells:

$$\chi(k) = \sum_{j=1}^{\text{Shells}} A_j(k) \sin \delta_j(k) \quad (\text{eq. 8})$$

It gives information on the average coordination around an absorbed atom, indicating the bulk character of the technique. In the $\chi(k)$ function the $\sin \delta_j$ (eq. 9) describes the interference pattern:

$$\sin \delta_j(k) = \sin[2kR_j + \varphi_j(k)] \quad (\text{eq. 9})$$

The argument of the $\sin \delta_j$ function consists of the inter-atomic distance and a phase factor. The phase factor is determined by the potential experienced

by the emitted electron from the backscattering atom and by the leaving and re-entering the absorber atom potential. A_j (eq. 10) is the amplitude of the EXAFS function.

$$A_j(k) = \frac{N_j}{kR_j^2} S_0^2 F_j(k) e^{-2k^2\sigma_j^2} e^{-2R_j/\lambda(k)} \quad (\text{eq. 10})$$

The amplitude of the EXAFS function contains the coordination number (N) and the disorder (σ). Each has a unique electron configuration and thus a unique backscattering pattern, which is expressed in $F_j(k)$, the backscattering amplitude. S_0^2 is an amplitude reduction factor that accounts for many body effects and relaxation processes. The exponential term containing λ (the mean free path of the photo-electron) represents the finite lifetime of the excited state.

We have applied EXAFS to the study of Mn in Mn-ZSM-5. The EXAFS analysis has been used mainly to determine the average distances to the neighbours (R) and the coordination number (N). R correlates with the Mn valence and from N the average particle size can be determined.

2.1.6. Experimental aspects of XAS

The XAFS spectrum can be measured by detecting the absorption of the primary beam (transmission) or by collecting X-ray fluorescence. Further alternatives exist (Auger decay and ion decay), but these are not used in this PhD thesis. The transmission of x-rays is described by Lambert Beer's law:

$$dI = -\mu(E)I dx \quad (\text{eq. 11})$$

$$I = I_0 \exp(-\mu(E)x) \quad (\text{eq. 12})$$

dI is the decrease in intensity of an x-ray beam through the path length dx . I is the intensity of the attenuated beam, I_0 of the initial x-ray beam and x the path length through the medium.

In case of diluted samples, such as Mn-ZSM-5, the XAS of the low

loaded Mn atoms is small compared to the large background absorption of Si, Al and O. Dilute samples are best measured with X-ray fluorescence detection. The relation of fluorescence yield (I_f) and the absorption cross-section is described by the following equation:

$$I_f = \frac{\mu_x(E)}{\mu_x(E) + \mu_b(E) + \mu_x(E_f) + \mu_b(E_f)} \quad (\text{eq. 13})$$

where μ_b and μ_x are respectively the background and edge absorption at the excitation energy (E) and at the dominant emission energy (E_f). For diluted samples the μ_b dominates the absorption at a certain edge (μ_x) and the measured intensity is equivalent to the absorption coefficient of the target atom ($I_f \sim \mu_x$). For samples with a higher metal oxide loading saturation effects can alter the spectrum.

In this work the XAS spectrum is measured with $K\alpha$ and $K\beta$ fluorescence detection. All spectra, other than the references, relate to low Mn loadings where the fluorescence intensity is proportional to the XAS cross section. We have also used high-resolution detection of the $K\alpha$ and $K\beta$ fluorescence, which yields a number of new possibilities.

2.2. Scanning electron microscopy

Scanning electron microscopy (SEM) is a type of electron microscopy capable of producing high resolution images of a sample surface. Due to the manner in which the image is created, SEM images have a characteristic three-dimensional appearance and are useful for judging the surface structure of the sample [11].

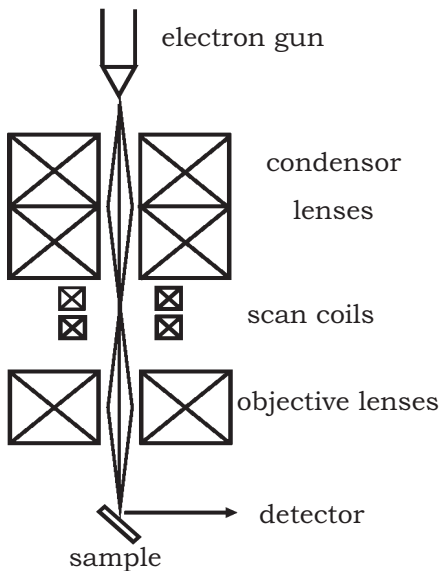


Figure 5. Schematic set-up of an electron microscope for scanning mode.

In a typical SEM, electrons are thermionically emitted from a cathode and are accelerated towards an anode; alternatively electrons can be emitted via field emission (FE). The electron beam, which typically has an energy ranging from a few hundred eV to 50 keV, is focused by one or two condenser lenses into a beam with a very fine focal spot sized 1 nm to 5 nm. The beam passes through pairs of scanning coils in the objective lens, which deflect the beam in a raster fashion over a rectangular area of the sample surface. Through these scattering events, the primary electron beam effectively spreads and fills a teardrop-shaped volume, known as the interaction volume, extending from less than 100 nm to around 5 μm into the surface. Interactions in this region lead to the subsequent emission of electrons that are then detected to produce an image. The most common imaging mode monitors low energy (<50 eV) secondary electrons. Due to their low

energy, these electrons originate within a few nanometres from the surface. The electrons are detected by a scintillator-photomultiplier device and the resulting signal is rendered into a two-dimensional intensity distribution that can be viewed and saved as a digital image. This process relies on a raster-scanned primary beam. The brightness of the signal depends on the number of secondary electrons reaching the detector. If the beam enters the sample perpendicular to the surface, then the activated region is uniform about the axis of the beam and a certain number of electrons "escape" from within the sample. As the angle of incidence increases, the "escape" distance of one side of the beam will decrease, and more secondary electrons will be emitted. Thus steep surfaces and edges tend to be brighter than flat surfaces, which results in images with a well-defined, three-dimensional appearance. Using this technique, resolutions less than 1 nm are possible. In addition to the secondary electrons, backscattered electrons can also be detected.

2.3. Scanning transmission electron microscopy combined with energy loss spectroscopy

Scanning Transmission Electron Microscopy combined with Energy Loss Spectroscopy (STEM-EELS) is a combined technique in which transmission EELS spectra are used to investigate the electronic structure of solids. Core-level EELS spectroscopy yields information on transitions from one well defined atomic orbital to a vacant state above the Fermi level: it is a probe of the energy distribution of unoccupied states in a solid. In Figure 6 a typical EELS spectrum is shown. As the excited electron is promoted from a given atomic orbital on a well-defined site, the corresponding final state must first satisfy the dipolar selection rules valid for small scattering angles. Thus s-type electrons are promoted to p-type states, p-type electrons predominantly go to d-type or s-type vacant states and so on [12].

EELS measurements can be performed on all kinds of specimens, for example, biological tissues, inorganic materials and polymers. The sample preparation (in order to get a thin foil, typically less than 50 nm in thickness) is likewise as for conventional transmission electron microscopic observation. The recorded data originate from selected areas, which can

otherwise be characterized by imaging and diffraction for complementary information on the structure of the investigated specimen. EELS is an elemental and chemical specific bulk technique.

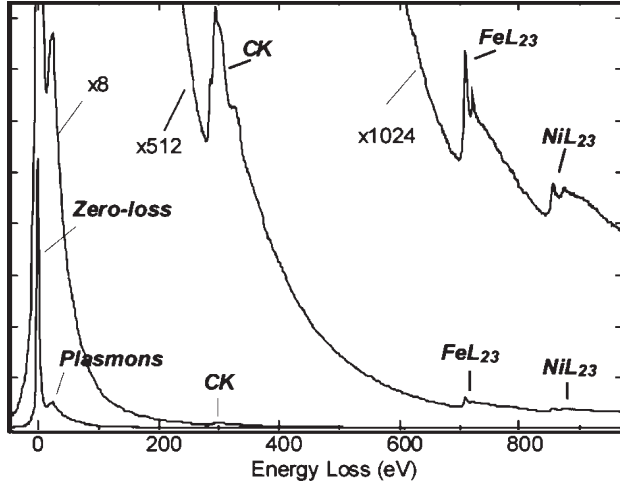


Figure 6. EELS spectrum of NiFe particles encapsulated in carbon [13,14]. The whole spectrum extending over 1000 eV covers 4 orders of magnitude in intensity when comparing the non-saturated zero-loss peak and the details of overlapping Ni and Fe edges around 800 eV.

In a transmission experiment, a beam of monochromatic particles impinges on a specimen and one measures the change in energy and momentum that the particles suffer, while propagating through the thin sample foil (Figure 7). For small momentum transfers $q \rightarrow 0$, where q is the momentum, and EELS measures the same solid properties as in far UV or soft X-ray absorption spectroscopy with the advantage that the spectroscopic information can easily be correlated to a detailed structural and topographical knowledge of the specimen. Using the Fermi golden rule in the single-electron and dipole approximations, the inelastic cross section and, heretorelated the intensity I , can be written in terms of matrix elements:

$$I \cong \frac{1}{q^2} |\langle f | \mathbf{e}_q \cdot \mathbf{r} | i \rangle|^2 \rho_f(\Delta E) \quad (\text{eq. 14})$$

with the initial $|i\rangle$ and the final $|f\rangle$ states of the transition and $\rho_f(\Delta E)$ designating the density of accessible final states for the energy loss ΔE .

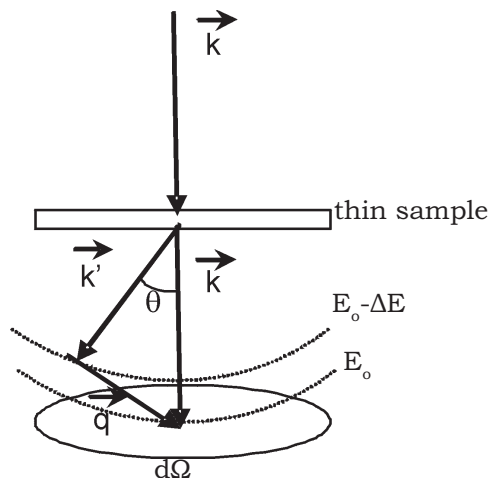


Figure 7. Scattering geometry of an electron energy loss experiment in a STEM. A primary electron of energy E_0 and wave vector k is inelastically scattered into a state of energy $E_0 - \Delta E$ and wave vector k' . The energy loss is ΔE and the momentum transfer is ηq . The scattering angle θ varies from 0 to θ limit as depicted. The scattered electrons are collected within an aperture of solid angle $d\Omega$ to be analysed by the spectrometer.

The term e_q is the unit vector in the direction of the momentum transfer and the total term $e_q \cdot r$ is the dipole operator. This dependence can be used to investigate the transitions allowed along given reciprocal space directions. Inelastic scattering data are related to the excitation spectra of the different electron populations in the target. If the incident beam is focused into a small sized probe on the sample, the momentum distribution is partially lost, but one can then select the information from an area as small as a fraction of a nanometre [15]. The spectra obtained with EELS can be used to perform quantitative elemental analysis or to calculate atomic ratios of elements present in a sample.

EELS studies have gained a wide increase in popularity, since the analysers became available as an attachment to an electron microscope (EM). This configuration offers access on the same instrument to the standard EM capabilities for image and diffraction characterisation. A magnetic prism spectrometer with a design involving second-order aberration corrections is most suitable for standard EELS analysis. Attached on scanning transmission electron microscopes of the latest generation, it provides the acquisition of EEL spectra with an energy resolution of the order of 0.4 eV (mostly limited by the natural energy distribution of the field-emitted primary beam) with

ultra-high spatial resolution (defined by the diameter of the focussed beam issued from the field emission gun).

In the 100 kV STEM instrument in operation in Orsay and used in this work a probe of 0.5 nm in is diameter focussed on the entrance surface of the specimen can carry a few tenths of nA, adequate to provide spectra of a signal-to-noise ratio within a short acquisition time (typically 10 to 500 ms for the plasmon region and 100 ms to 10 s for the core-loss region). In Figure 8 a schematic representation of the equipment is shown. In most core-loss spectra, the practical energy resolution is in the order of 0.5 to 0.7 eV, providing the possibility of resolving fine structures separated by 0.8 to 1.0 eV.

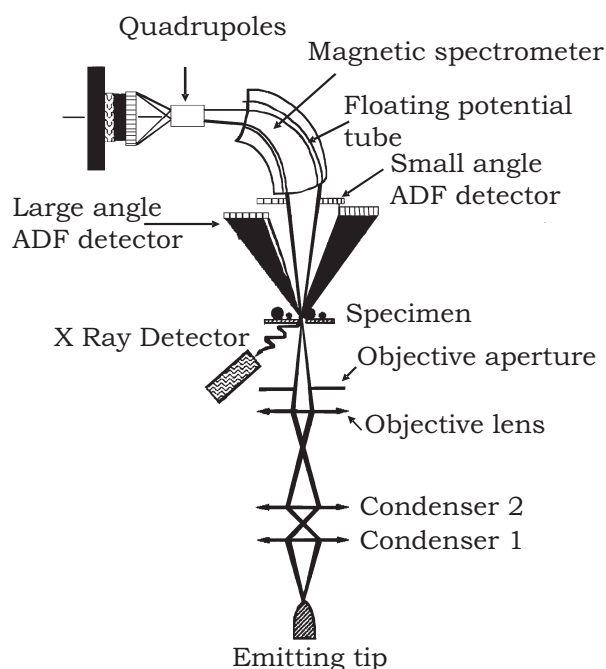


Figure 8. Basic components of the dedicated STEM equipped with an EELS spectrometer and a parallel detector array, in operation in Orsay. It offers the simultaneous capability of visualising the object topography through the annular detectors (small angle for diffraction contrast, large angle for Z-contrast) and of analysing with the magnetic spectrometer the energy loss distribution of forwardly transmitted electrons.

2.4. Ultraviolet-Visible Diffuse Reflectance Spectroscopy

Ultraviolet-Visible (UV-vis) spectroscopy measures the electronic excitations between the energy levels that correspond to the molecular orbitals of the system. The energy associated with the electronic excitations creates vibrations of the molecule and the transitions are thereby broadened. Light in the UV-vis region of the electromagnetic spectrum can be used to study the electronic transitions of a sample. According to the nature of the electronic jumps, the electronic excitations can be classified into several groups:

- (a) Metal - metal transitions.
- (b) Metal - ligand charge transfer transitions (MLCT) and ligand-metal charge transfer transitions (LMCT).
- (c) Ligand - ligand transitions.

The metal - metal transitions are mainly the transitions within the 3d-manifold. The ligand states involve σ and π bonding states, non-bonding (n) states and σ^* and π^* anti-bonding states. Below we will present a few characteristics of the above transitions [16,17].

(a) $d \rightarrow d$ transitions represents the transition of an electron in the d orbitals. According to crystal field theory, the coordination environment has an influence on the position of the d orbitals. This is depicted in Figure 9. So, for a six coordinated species (octahedral symmetry) the d orbitals are splitted in two sets, the t_{2g} (d_{xy} , d_{xz} , d_{yz}) and e_g (d_{z^2} and $d_{x^2-y^2}$), where e_g is higher in energy than t_{2g} . In the case of tetrahedral symmetry the t_2 orbitals are situated at higher energy then the e orbitals [18].

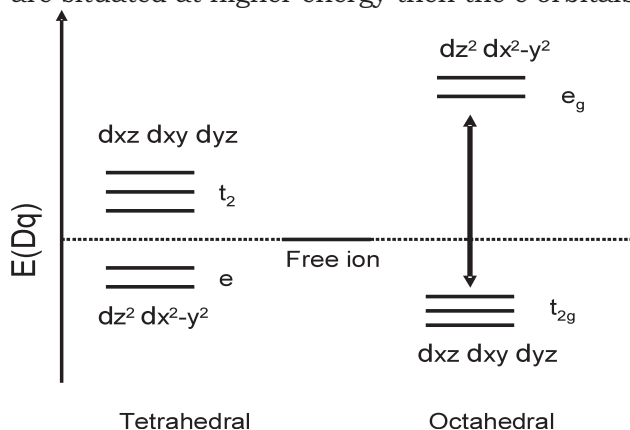


Figure 9. Position of the d orbitals in the case of a tetrahedral and octahedral symmetry.

Tanabe and Sugano were the first who used the crystal field multiplet equations in order to construct a comprehensive diagram that can interpret the electronic spectra. The Tanabe-Sugano diagram describes the states in a $3d^n$ multiplet including all atomic multiplet and crystal field interactions. It is presented as a function of E/B (where E is the energy of the state and B the Racah parameter) versus the cubic crystal field, indicated as Δ/B . A vertical line to an excited state is a measurement of the transition energy in terms of Δ and B . An experimental spectrum can be interpreted from this diagram by relating the energies of the observed bands to the allowed transitions.

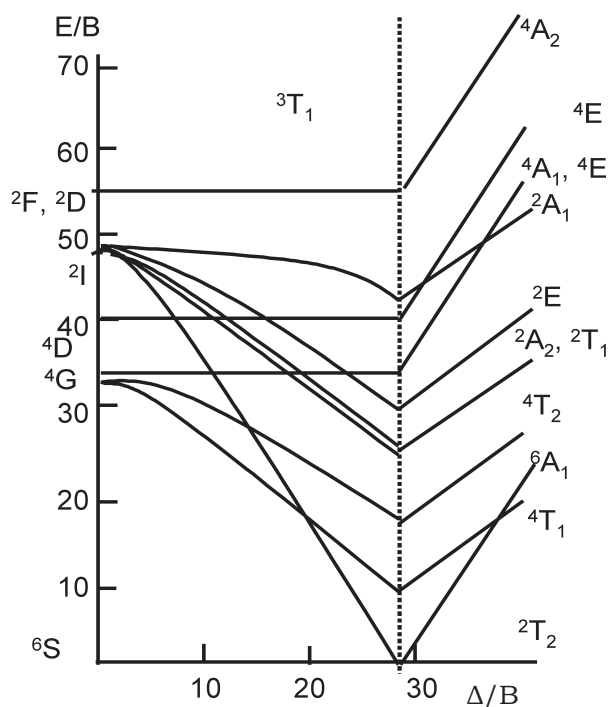


Figure 10. The Tanabe-Sugano diagram for d^5 in octahedral symmetry.

(b) Charge transfer transitions are due to the electron transfer from an orbital mainly localized on the metal to that mainly localized on the ligand ($M \rightarrow L$ transfer), usually occurs when the ligand has low π^* orbitals [19]; or in the opposite direction ($L \rightarrow M$ transfer) when the ligand has a lone pairs or the metal has low lying empty orbitals [16]. These $L \rightarrow M$ charge transfer are most common for transitional metal ions. The energies of these transitions are higher than that for $d \rightarrow d$ transitions being situated in the

UV region of the spectra.

(c) There are a large number of ligand-ligand transitions possible. This includes all transitions from occupied to empty states, for example $\sigma \rightarrow \sigma^*$, $n \rightarrow \sigma^*$, $n \rightarrow \pi^*$ and $\pi \rightarrow \pi^*$ transitions. In the case of transition metal oxides, these transitions are weaker than d - d and charge transfer transitions.

2.4.1. UV-vis detection methods

The measurements of UV-Vis spectra can be performed in transmission and in reflection mode. In the case of liquid samples transmission mode is the most used method. In this case, the transmittance T of the sample is determined by the difference between the intensity of the incident beam and the intensity of the transmitted beam [20]. Knowing the transmittance T , the absorbance of the sample can be determined via the formula:

$$A = -\log T \quad (\text{eq. 15})$$

The absorbance can be expressed as a function of the molar absorption (ϵ) the path length of the sample (b) and the concentration of the compound in solution (c) using Lambert-Beer's law:

$$A = \epsilon bc \quad (\text{eq. 16})$$

Due to the direct proportionality of the absorbance with the concentration of the sample, the transmission mode can be used both in a qualitative and quantitative manner.

When solids are to be measured the transmission mode is not suitable since the sample does not transmit light very well. In this case the reflection mode – or diffuse reflectance spectroscopy (DRS) – is used [19]. DRS is based on the theory that the light will diffuse and reflect on the particles which form the solid sample and the resulting diffuse reflected light will be detected using e.g. an integrated sphere. The principle is illustrated in Figure 11.

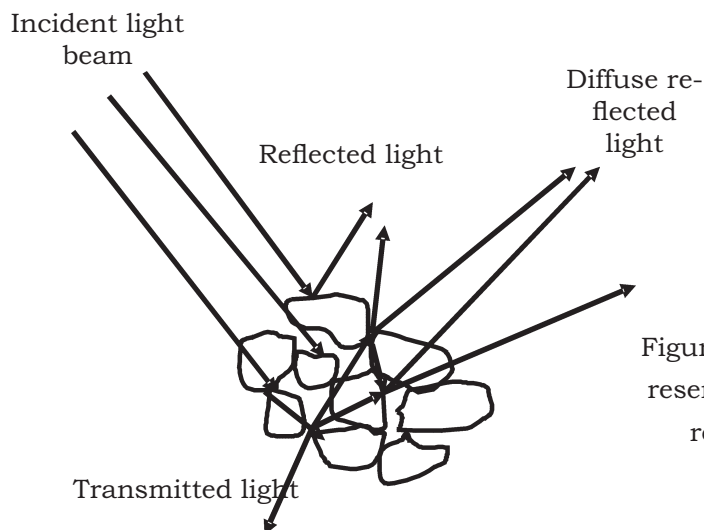


Figure 11. Schematic representation of the diffuse reflectance theory.

This diffuse reflected light is not proportional to the concentration of the compound, and in order to determine the concentration a mathematical conversion is used, namely the Kubelka-Munk transformation [21,22]:

$$F(R_{\infty}) = \frac{(1 - R_{\infty})^2}{2R_{\infty}} = \frac{K}{S} \quad (\text{eq.17})$$

Where R is the absolute reflectance of the sampled layer, K is the molar absorption coefficient and S is the scattering coefficient.

The absorption and scattering coefficients, K and S , do not have a physical meaning, but in the case of diffuse reflected light, they are related to the intrinsic absorbing ($a = 1/2 K$) and scattering ($s = S$) coefficients of the sample [23]. R_{∞} is usually determined by dividing the intensity of the light reflected by the sample by the light reflected from an ideally white reference (MgO , BaSO_4 or Halon).

References

- [1] C. Hammond, *The Basics of Crystallography and Diffraction*, Oxford University Press, Oxford, **1998**.
- [2] H. M. Rietveld, *J. Appl. Crystallogr.*, 2, **(1969)**, 65.
- [3] M. Ruitenbeek; F. M. F. de Groot; A. J. V. Dillen; D. C. Koningsberger, *Stud. Surf. Sci. Catal.*, 130D, **(2000)**, 3101.
- [4] M. Ruitenbeek; A. J. van Dillen; F. M. F. de Groot; I. E. Wachs; J. W. Geus; D. C. Koningsberger, *Top. Catal.*, 10, **(2000)**, 241.
- [5] K. Inumaru; M. Misono; T. Okuhara, *Appl. Catal. A Gen.*, 149, **(1997)**, 133.
- [6] T. Okuhara; K. Inumaru; M. Misono; N. Matsubayashi; H. Shimada; A. Nishijima, *Catal. Lett.*, 20, **(1993)**, 73.
- [7] K. Inumaru; T. Okuhara; M. Misono; N. Matsubayashi; H. Shimada; A. Nishijima, *J. Chem. Soc., Faraday Trans.*, 88, **(1992)**, 625.
- [8] K. Inumaru; T. Okuhara; M. Misono; N. Matsubayashi; H. Shimada; A. Nishijima, *J. Chem. Soc., Faraday Trans.*, 87, **(1991)**, 1807.
- [9] R. Kozlowski; R. F. Pettifer; J. M. Thomas, *J. Phys. Chem.*, 87, **(1983)**, 5176.
- [10] J. Wong; F. W. Lytle; R. P. Messmer; D. H. Maylotte, *Phys. Rev. B.*, 30, **(1984)**, 5596.
- [11] J. W. Niemantsverdriet, *Spectroscopy in Catalysis*; Wiley-VCH, Weinheim **2000**.
- [12] P. Rez; X. D. Weng; M. Hong, *Microscopy Microanalysis Microstructures*, 2, **(1991)**, 143.
- [13] W. Teunissen; J. W. Geus, *Stud. Surf. Sci. Catal.*, 121, **(1998)**, 185
- [14] W. Teunissen; A. A. Bol; J. W. Geus, *Catal. Today*, 48, **(1999)**, 329.
- [15] C. Colliex; NATO ASI Series, Series B: Physics Vol. 345, Editors: P.S. Bagus, G. Pacchioni and F. Parmigiani, 213.
- [16] R. M. Edreva-Kardjieva, *Bulg. Chem. Comm.*, **(1992)**, 166.
- [17] D. F. Shriver; P. W. Atkins; C. H. Langford, *Inorganic Chemistry*; Oxford University Press, Oxford, **1995**.
- [18] W. W. Porterfield, *Inorganic Chemistry: a unified approach*, Academic Press, San Diego, **1993**.
- [19] B. M. Weckhuysen; P. van de Voort; G. Catana (Eds.), *Spectroscopy of Transition Metal Ions on Surfaces*; Leuven University Press, Leuven, **2000**.
- [20] D. C. Harris, *Quantitative Chemical Analysis*, W. H. Freeman and Company, New York, **1995**.

- [21] P. Kubelka, *J. Opt. Soc. Am.*, 38, **(1948)**, 448.
- [22] P. Kubelka; F. Munk, *Z. Tech. Phys.* , 12, **(1931)**, 593.
- [23] X. T. Gao; J. M. Jehng; I. E. Wachs, *J. Catal.*, 209, **(2002)**, 43.

3

Catalytic Decomposition of Nitrous Oxide on Mn-ZSM-5: Linking the 18500 cm⁻¹ UV-vis Band to Catalytic Activity

Abstract

Manganese-containing Mn-ZSM-5 zeolites have been synthesized using an ion exchange procedure. The activity of this material was investigated for the decomposition of N₂O. It was found that this reaction indeed takes place with the generation of α -oxygen species, which gives rise to an UV-vis band at around 18500 cm⁻¹. The reactivity of the generated α -oxygen species was tested using the NO oxidation reaction. In-situ XAS experiments shows that the active phase is formed from manganese atoms involved in a redox cycle, whose oxidation state alter between Mn³⁺ during α -oxygen generation and Mn²⁺ after α -oxygen removal. Scanning transmission electron microscopy (STEM) electron energy-loss spectroscopy (EELS) shows that Mn is spread over the external surface of the zeolite material.

3.1. Introduction

Starting from the 1990's, N_2O was recognized as an environmental pollutant contributing to the ozone depletion and enhancing the greenhouse effect [1]. Principal pollution sites are combustion processes and chemical production sites for adipic acid. Due to the stationary character of these sources, catalytic decomposition of N_2O is an attractive solution to eliminate or reduce the N_2O emissions. Various metal and metal oxides have been screened in order to identify active catalysts for the catalytic decomposition reaction [2]. These experiments determined that a key parameter in this reaction is the need for labile oxygen at the catalyst surface in order to complete the catalytic cycle, which is directly connected to the oxidation state of the transition metal ion used.

Manganese oxides are known for their oxidation-reduction chemistry, based on which Yamashita et al. [3] showed that they are active in N_2O decomposition, having relatively high activities for catalytic systems with low surface area. It was also shown that N_2O decomposition occurs over all Mn oxides, but stable behavior was observed only for Mn_2O_3 and Mn_3O_4 . The reactivity of these manganese oxides can be extended to the Selective Catalytic Reduction (SCR) methods of NO_x removal with ammonia [2,4-9]. Experiments by Cimino et al. [10] and Stone et al. [11] show that by introducing low amounts of transition metal ions in inert oxide matrices (< 1 transition metal ion per 100 cations), the catalytic activity increases. At higher transition metal ion amounts, the activity resembles that of the corresponding pure oxides. Following this idea, interesting results are obtained using zeolites. Panov and co-workers [12] have used Fe-ZSM-5 to decompose N_2O into stoichiometric amounts for N_2 and O_2 at temperatures above 523 K [13]. However, at temperatures below 523 K, N_2O decomposes to N_2 plus atomically adsorbed oxygen bound to extra-framework Fe-species. The adsorbed oxygen formed in this way can be used to oxidize other molecules such as methane [14,15] or benzene [16]. Similar results have been obtained for copper - loaded zeolites. For example, experiments using Cu-ZSM-5 [17,18] suggest that zeolites are good replacement for amorphous oxide matrices, being able to provide a better dispersion of the metal ion over a higher surface area. In this chapter, we present results obtained on Mn-ZSM-5 zeolites.

3.2. Experimental

3.2.1. Catalyst preparation

A series of Mn-ZSM-5 zeolites differing in their Mn/Al molar ratios have been prepared via ion exchange starting from NH_4 -ZSM-5 (ZEOLISTS, Si/Al ratio of 17.5, surface area of $361 \text{ m}^2/\text{g}$ and pore volume of $0.124 \text{ cm}^3/\text{g}$). The samples prepared, together with their sample code, Mn loading and Mn/Al molar ratios are summarized in Table 1. As a manganese source, manganese acetate tetrahydrate ($\text{Mn}(\text{ac})_2 \cdot 4\text{H}_2\text{O}$) (99+%, Acros) was used. The ion exchange step was carried out for 24 h at a pH of 6.5 in a stirring reactor placed in a double wall vessel connected to a water bath to maintain a constant temperature of 343 K. After ion exchange, the zeolite samples were washed with de-ionized water, and dried at 373 K for 24 h. Before calcination the samples were pressed and sieved in order to obtain a particle size fraction between 150 and $212 \mu\text{m}$. For sample activation, a procedure denoted as “mild calcination” was applied and consists of heating up the sample to 823 K with a ramp of 0.5 K/min in an 800 ml/min flow of N_2 . At 473 K, 200 ml/min O_2 flow has been introduced to the gas mixture. Once a temperature of 823 K was reached the zeolite sample was kept under the same experimental conditions for 3 h, after which the zeolite sample was cooled down to room temperature with a ramp of 10 K/min .

After each step in the catalyst preparation procedure, the samples were measured with X-ray diffraction (XRD). As reference compounds for these XRD measurements the following oxides were selected: MnO (99%, Aldrich), Mn_2O_3 (99%, Aldrich) and MnO_2 (99.99%, Aldrich).

Table 1. Mn-ZSM-5 samples under study, including their sample codes together with the Mn loadings as measured by XRF and Mn/Al ratios.

Sample code	Mn loading (wt %)	Mn/Al molar ratio
MnZ-0.00	0.00	0.00
MnZ-0.13	0.64	0.13
MnZ-0.15	0.74	0.15
MnZ-0.19	0.98	0.19
MnZ-0.22	1.11	0.22
MnZ-0.24	1.20	0.24
MnZ-0.26	1.30	0.26
MnZ-0.30	1.44	0.29

3.2.2. Catalyst characterization

X-ray diffraction

XRD patterns of the zeolite samples were measured using an Enraf-Nonius CPS 120 powder diffraction apparatus with Co K α radiation ($\lambda = 1.789\text{\AA}$).

X-ray fluorescence spectroscopy

Elemental analysis was carried out using a Goffin Meyvis spectroX-lab 2000 X-Ray Fluorescence (XRF) spectrometer in order to determine the Mn loading and the Si and Al content in the synthesized materials.

Diffuse reflectance UV-Vis-NIR spectroscopy

After activation, the zeolite samples were introduced in a quartz flow cell equipped with a UV-Vis-NIR transparent window. Two O-ring valves were used in order to make the cell airtight and allow us to make in-situ measurements. All Mn-containing samples after dehydration were treated for 1 h in an 80 ml/min flow of 0.375%N₂O/He at 623 K. The cell was

closed and a UV-Vis spectrum was recorded. After this, the cell was flushed with He for 10 min in order to remove the traces of N_2O and an 80 ml/min flow of 0.375%NO/He was introduced for another hour. This procedure was repeated three times, and after each treatment DRS spectra of the catalyst sample were measured. UV-Vis-NIR diffuse reflectance (DRS) spectra were recorded on a Varian Cary 500 spectrometer in the range 5000 – 50000 cm^{-1} (200-2200 nm). In order to eliminate the potential spectral contributions of the zeolite material, a spectrum of the quartz cell containing a dehydrated ZSM-5 zeolite sample was used as a white reference standard.

Transmission electron microscopy and electron energy loss spectroscopy

Scanning transmission electron microscopy (STEM) electron energy-loss spectroscopy (EELS) measurements were performed in Orsay (France) with a 100 keV STEM instrument (VG HB 501) equipped with a field emission electron source. Mounted on the STEM instrument was a parallel electron energy-loss spectrometer (Gatan 666) optically coupled to a CCD camera generating an EELS spectrum with a 0.5-0.7 eV energy resolution and 0.5 nm spatial resolution within a typical acquisition time down to 1 ms per pixel. In these experiments, the oxygen K edge, silicon L edge and manganese L edge were monitored. The solids were first sonicated in ethanol and then dropped on a holey amorphous carbon film supported on a copper grid. After the sample was scanned, appropriate areas were selected for the measurement of detailed 2-D STEM-EELS images. An integrated energy range of 15 eV was used to quantify the EELS spectra.

3.2.3. Catalytic testing

Catalytic activity of the zeolite sample with a particle size between 150 and 212 μm was measured using a quartz flow reactor in which typically 0.1 g catalyst was placed on a frit. The reactor was placed in an oven that can be controlled within ± 1 K from the desired temperature using a West 6810 temperature controller. Concentrations and flow rate (total flow rate of 80 ml/min) were controlled by means of Brooks mass flow controllers. The inlet concentration of N_2O was 3750 ppm balanced with He till the desired flow.

When NO was used, the inlet concentration of NO was 3750 ppm balanced with He. Before each run the catalyst was pre-treated by heating up to 673 K in He flow and kept there for 1 h. Then the catalyst was cooled down to the reaction temperature. A typical catalytic experiment consists of exposures to N_2O for 1 h, followed for 10 minutes flushing with He in order to eliminate the traces of N_2O from the system. At the end of the flushing period, 3750 ppm of NO was introduced in the gas flow for 1 h, followed again by a 10 minutes period of flushing with helium. These steps were repeated 3 times, giving 3 consecutive cycles of N_2O /NO treatments. Product analysis was carried out using an Interscience Compact GC system, equipped with two different columns (a Molsieve 5A and a Porabond Q) each having a TCD detector. Also, a Thermo Environment Instruments 42C NO_x chemiluminescence analyzer was connected in parallel with the GC in order to determine the NO and NO_x concentrations and could be operated simultaneously.

3.3. Results

3.3.1. X-ray Diffraction

The XRD patterns of Mn-loaded ZSM-5 samples after calcination are all similar and as an example we show in Figure 1 the XRD pattern of MnZ-0.26. This figure compares the XRD pattern of MnZ-0.26 with those of bare ZSM-5, MnO (99%, Aldrich), Mn_2O_3 (99%, Aldrich) and MnO_2 (99.99%, Aldrich). The diffraction pattern of the Mn-loaded ZSM-5 indicates that no destruction of the zeolite lattice took place during catalyst preparation. No additional peaks due to the presence of Mn oxide phases could be found within the experimental sensitivity of XRD.

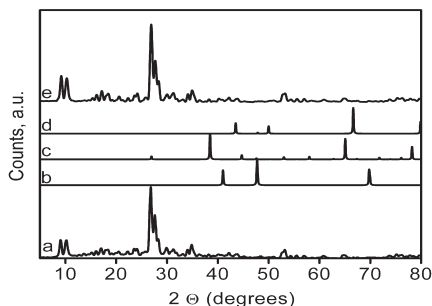


Figure 1. XRD patterns of the parent ZSM-5 sample (a); MnO (b); Mn_2O_3 (c); MnO_2 (d) and MnZ-0.26 (e).

3.3.2. UV-Vis-NIR Diffuse Reflectance Spectroscopy

Each Mn-containing sample was exposed to a gas treatment as presented in the experimental section. Two representative spectra are shown in Figure 2 for MnZ-0.26, but similar spectra have been obtained for the other Mn-loadings. It is evident from Figure 2 that after N_2O treatment a relatively intense absorption band situated at $\sim 18500\text{ cm}^{-1}$ appears in the spectrum. This band disappears when NO was flushed over Mn-ZSM-5, but it is restored with every N_2O treatment.

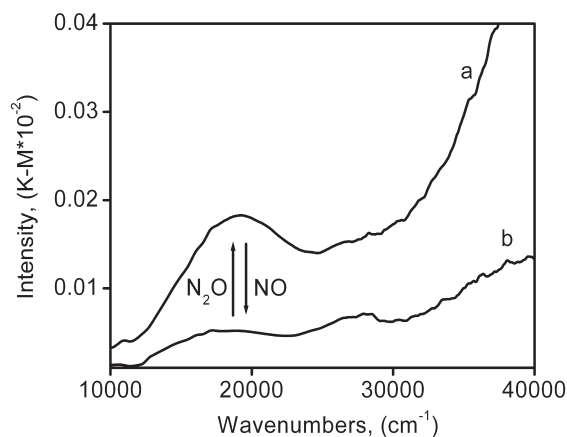


Figure 2. DRS spectra of MnZ-0.26 after different gas treatments: (a) represents the sample after N_2O treatment at 623 K for 1 h and (b) represents the sample after a subsequent NO treatment at 623 K for 1h.

The attempts to generate this band at temperatures below 623 K were unsuccessful. Also, when instead of N_2O , molecular oxygen was used in the temperature range of 298 - 673 K no UV-Vis band has been observed.

When reproducibility of this band was investigated, it was observed that the activation conditions have an important role in obtaining good quality samples. Figure 3 presents two reproducibility experiments, where in the first case (left) the oxygen flow during the activation procedure was altered, resulting in a different UV-Vis band, while in a second case (Figure 3 - right) the activation parameters were used according to the procedure presented in the catalyst preparation section.

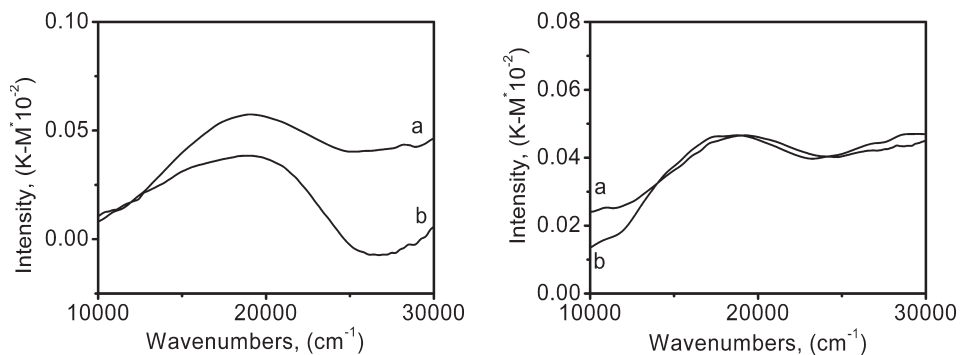


Figure 3. Left - DRS spectra of the MnZ-0.22 (a) and a reproduced sample (b) after 1 h of N_2O gas treatment at 623 K. Right - DRS spectra of the MnZ-0.24 (a) and a reproduced sample (b) after 1 h of N_2O gas treatment at 623 K.

In order to assign the absorption band at $\sim 18500\text{ cm}^{-1}$ a literature investigation has been performed. Table 2 summarizes the UV-Vis-NIR absorption bands of a set of manganese-containing oxides and their corresponding spectral assignments. It can be seen that several trivalent manganese reference compounds possess an absorption band at around 20000 cm^{-1} .

Table 2. Absorption maxima of UV-Vis-NIR bands of manganese-containing oxides, together with their spectral assignments.

Compound	Valence state	Absorption maximum (cm ⁻¹)	Spectral assignment	Reference
MnO	2+	16400 20800 23800	${}^6A_1 \rightarrow {}^4T_2$ ${}^6A_1 \rightarrow {}^4T_2$ ${}^6A_1 \rightarrow {}^4A_1$	[19]
Mn(Ac) ₂ ·4H ₂ O	2+	18500 22700 24740	${}^6A_1 \rightarrow {}^4T_2$ ${}^6A_1 \rightarrow {}^4T_2$ ${}^6A_1 \rightarrow {}^4A_1$	[20]
Mn ₂ O ₃	3+	13250 20610 27027	${}^5B_{1g} \rightarrow {}^5A_{1g}$ ${}^5B_{1g} \rightarrow {}^5E_g$ ${}^5B_{1g} \rightarrow {}^5B_{2g}$	[21]
Mn/Al ₂ O ₃	3+	20600 23700	${}^5E_g \rightarrow {}^5T_{2g} (\parallel)$ ${}^5E_g \rightarrow {}^5T_{2g} (\perp)$	[22]
MnAPO-34	3+	20400	${}^5E_g \rightarrow {}^5T_{2g}$	[23]
Mn(PO ₃) ₃	3+	11450 18870 20060	${}^5B_{1g} \rightarrow {}^5A_{1g}$ ${}^5B_{1g} \rightarrow {}^5B_{1g}$ ${}^5B_{1g} \rightarrow {}^5E_g^{2g}$	[24]
Mn/Al ₂ O ₃	4+	21300	${}^4A_{2g} \rightarrow {}^4T_{2g}$	[25]

As seen in Table 2, Mn²⁺ with a 3d⁵ configuration has only spin forbidden transitions, which are inherently weak. In the case of MnO these bands are located at ~16400 cm⁻¹ and 20800 cm⁻¹. Several reference compounds with Mn³⁺ in an octahedral 3d⁴ configuration possess an absorption band at ~20000 cm⁻¹.

In Mn-ZSM-5 we identify two transitions situated at ~16000 cm⁻¹ and ~20000 cm⁻¹ (Figure 4). We can interpret these bands as similar to an elongated tetragonal Mn³⁺ system, where these transitions relate to respectively ${}^5B_{1g} \rightarrow {}^5B_{2g}$ and ${}^5B_{1g} \rightarrow {}^5E_g$. In octahedral symmetry this relates to a ${}^5E_g \rightarrow {}^5T_{2g}$ transition, where the T_{2g} states are split into B_{2g} and E_g by the tetragonal distortion. In Mn-ZSM-5 systems, the surroundings can be understood as 5-fold square pyramidal with significant variations in the angles and distances. Effectively this yields a series of sites that have transitions similar to ${}^5B_{1g} \rightarrow {}^5B_{2g}$ and ${}^5B_{1g} \rightarrow {}^5E_g$.

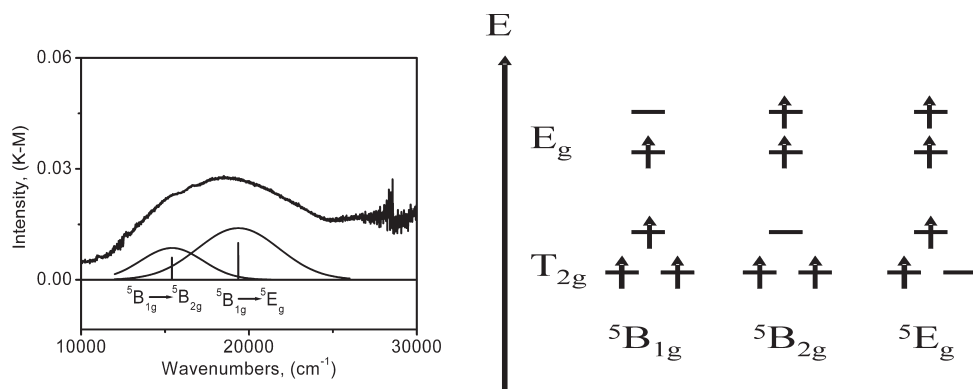


Figure 4. UV-Vis-NIR DR band intensity at 18500 cm⁻¹ of the MnZ-0.19 together with the fitted contributions of the observed transitions (left). (right) Energy levels of the assigned transitions.

Based on this assignment, the obtained UV-Vis spectra were analyzed using the GRAMS AI spectroscopy software, in order to obtain detailed information regarding the observed UV-Vis band. In a typical analysis the entire UV-Vis spectrum was fitted using the lowest number of Gaussian functions as possible in order to have a good fit value higher the 0.99 (Figure 5).

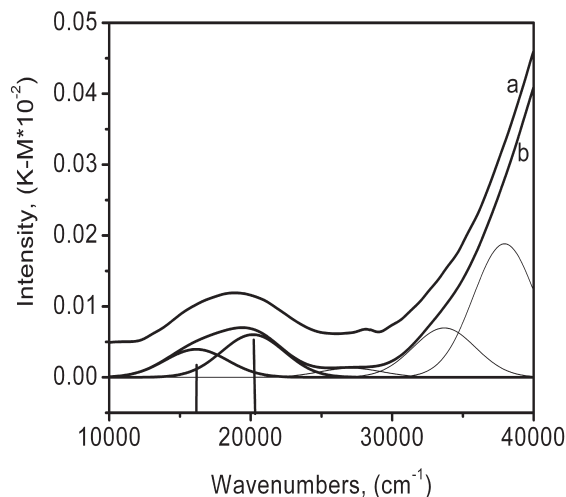


Figure 5. UV-Vis-NIR spectra of the MnZ-0.15 (a) together with the result of fitting (b) and the main contributions of the observed transitions. The lines indicate the centre of the main contributions for the UV-Vis band, while the Gaussians functions presented in thinner lines are used in order to obtain the final fit of the spectra. For a clearer picture the UV-Vis spectra is shifted to a higher intensity. No baseline correction was used for this procedure.

In Table 3 we present the values for wavenumber and integrated areas of the fitted contribution, which contribute to the 18500 cm^{-1} UV-Vis band for each of the investigated samples.

Table 3. Values of the integrated areas of the fitted contributions after N_2O exposure. The fitting procedure used involves non-inclusion of a baseline correction.

Sample code	% area for the fitted contribution at $\sim 16000\text{ cm}^{-1}$	% area for the fitted contribution at $\sim 20000\text{ cm}^{-1}$	Total area of the $\sim 18500\text{ cm}^{-1}$ band given by the sum of the two contributions
MnZ-0.00	0	0	0
MnZ-0.10	68.9	31.1	50.8
MnZ-0.15	39.6	60.4	55.1
MnZ-0.19	50.7	49.3	82.2
MnZ-0.22	42.8	57.2	157.0
MnZ-0.24	47.0	53	258.3
MnZ-0.26	39.1	60.9	414
MnZ-0.30	37.8	62.2	180

The results representing the total area of the 18500 cm^{-1} band can be reproduced if the treatment and the quantity of the measured sample are identical to those presented in the experimental section.

Figure 6 compares the intensity of the 18500 cm^{-1} UV-Vis band obtained for the Mn-ZSM-5 samples loaded with different amounts of Mn and treated in N_2O at 623 K for 1 h . It was found that the UV-Vis-NIR DR band increases with the increasing amount of manganese exchanged, reaches a maximum at a Mn/Al molar ratio of 0.26. Increasing the Mn/Al molar ratio further does not result in an increase of the 18500 cm^{-1} UV-Vis band intensity.

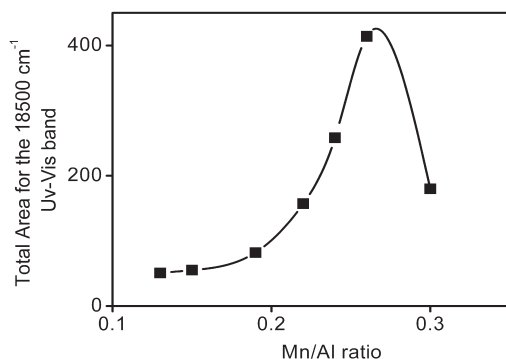


Figure 6. Total area of the UV-Vis-NIR DR band at 18500 cm^{-1} as a function of the Mn/Al molar ratio in Mn-ZSM-5 samples loaded with different amounts of Mn and treated in N_2O at 623 K for 1 h.

To observe the evolution of this band as a function of time, an experiment is performed where DRS spectra were collected at an interval of 10 min during a 80 min N_2O treatment, followed by a similar NO treatment. As seen in Figure 7A during N_2O treatment the UV-Vis band intensity is increasing in intensity with the time spent under the treatment. After 1 h of treatment the intensity of the band has reached a constant value. The zero point of the graph represents the absence of the UV-Vis band of the sample before the N_2O treatments. During the NO treatment the total area of the band has a constant decreasing trend as a function of the reaction time, reaching a minimum after 1 h. As observed in Figure 7B this minimum is not zero, which indicates that the NO treatment is not able to restore the initial state of the sample.

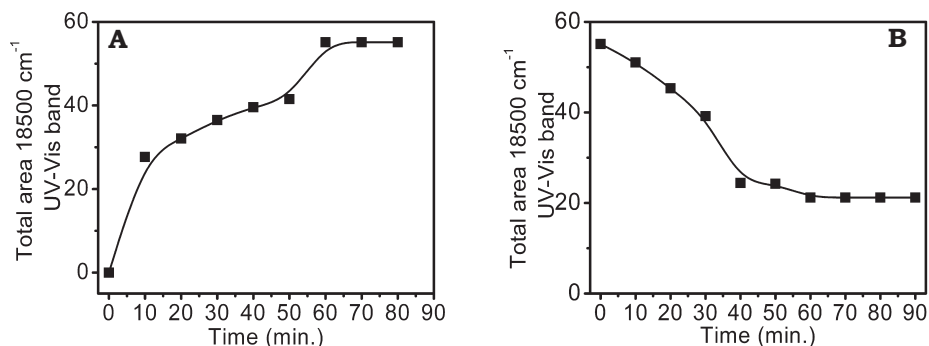


Figure 7. Evolution of the total area for the 18500 cm⁻¹ UV-Vis band during N₂O treatment measured at 10 min interval (A). Disappearance of the same UV-Vis band during NO treatment measured at the same time interval (B).

These experiments were performed using MnZ-0.15.

To check the validity of these observations, another set of experiments was performed, in which DRS spectra were measured after consecutive N₂O/NO treatment. The duration of these treatments was varied between 5 min and 45 min, where the sample was treated in the sequence 5 – 45 – 25 – 15 – 35 min in order to rule out any systematic errors. Figure 8 presents the result obtained from these experiments using MnZ-0.19. It can be observed that this set of experiments follows the same pattern as Figure 7, with the observation that after 5 min of N₂O exposure the UV-Vis band is not yet formed. It is also important to notice that the N₂O treatment is having an increasing effect on the intensity, while the NO treatment reduces the intensity to a constant value.

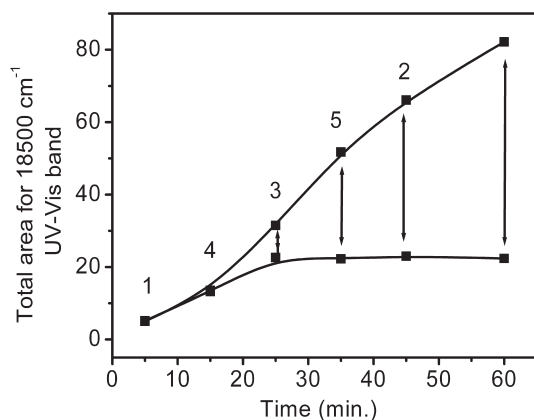


Figure 8. Evolution of the total area for the 18500 cm⁻¹ UV-Vis band for MnZ-0.19 during N₂O treatment measured at random time intervals (-■-) and the consecutive NO treatment for the same period of time (-●-). The arrows indicate the decrease of the total area of the band during N₂O/NO treatment for the same time period.

3.3.3. STEM-EELS

We have measured MnZ-0.24 with STEM-EELS. With the STEM dark field image the zeolite crystals have been mapped as indicated in Figure 9. It turned out that this sample was rapidly destroyed by the electron beam, which made it impossible to measure reliable STEM-EELS line spectra and 2D maps. Instead we have used the option to rapidly sweep over an area of the sample. Figure 9 (left) shows two areas that were measured, where the average signal over the complete area is indicated as average 1 and average 2. Average 1 is positioned exactly at the surface and measures the spectrum of the top 2 nm of the ZSM-5 crystal. The average 2 spectrum measures an area between 2 and 5 nm deep inside the sample.

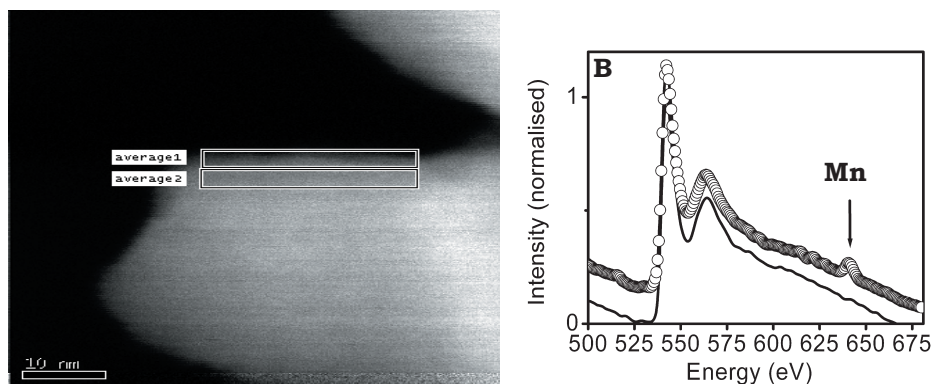


Figure 9. TEM image of MnZ-0.24, together with the corresponding Mn and Si L edge spectra of the surface particle (average 1-o-) and bulk (average 2-full line) of the zeolite.

It can be seen in Figure 9 (right) that the surface spectrum shows the presence of Mn, while the spectrum taken at 2-5 nm inside the ZSM-5 shows no Mn. We have measured a total of five different surfaces, where similar results have been found for three surfaces. Two other surfaces did not show a visible Mn signal for both its surface and subsurface spectrum, indicating that not all the ZSM-5 surfaces contain Mn in a detectable amount.

3.4. Catalytic tests

N_2O decomposition

Before the Mn-ZSM-5 samples were tested, we performed a series of blank experiments to rule out (a) reaction due to the ZSM-5 itself and (b) thermal decomposition of N_2O . The experiments using a pure ZSM-5 sample show no reaction products and the experiments on the N_2O decomposition indicate that thermal decomposition of N_2O occurs only above 698 K. We therefore conclude that at our reaction conditions the N_2O decomposition takes place due to the catalyst action and also that the active phase of the catalyst is the manganese present in the ZSM-5 zeolite.

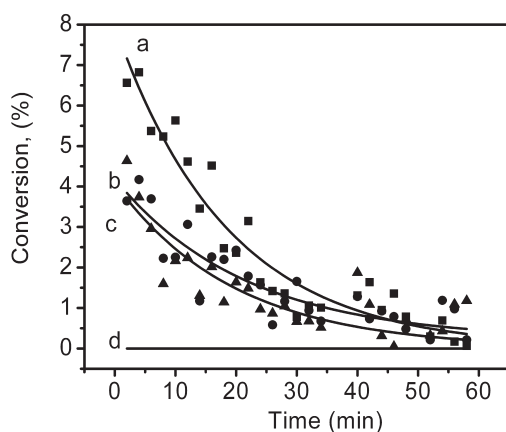


Figure 10. N_2O conversion profiles for sample MnZ-0.26 (a, -■-), MnZ-0.22 (b, -●-), MnZ-0.1 (c, -▲-) and MnZ-0.0 (d) during 1 h N_2O exposure at 623 K, 3750 ppm N_2O and 24000 GHSV (h^{-1}).

Figure 10 shows the conversion of the N_2O during the 1 h reaction time. The highest conversion is observed in the beginning of the reaction. In time the conversion decreases reaching zero after 1 h of reaction, although we note that the catalytic data are scattered.

A similar trend is observed for each sample from our series of samples. Figure 11 shows the maximum conversion in the first reaction cycle as a function of manganese loading. In addition, the second and the third reaction cycle are shown. It can be seen that during the first run the initial conversions are significantly higher than in the second and third run. The second and third runs are equivalent, indicating a stable N_2O -NO conversion cycle.

Note that the initial conversion for the MnZ-0.26 sample is significantly higher than for the other samples. The results for the second and third run follow a very gradual increase up to the MnZ-0.26, where the highest loading has a much lower conversion.

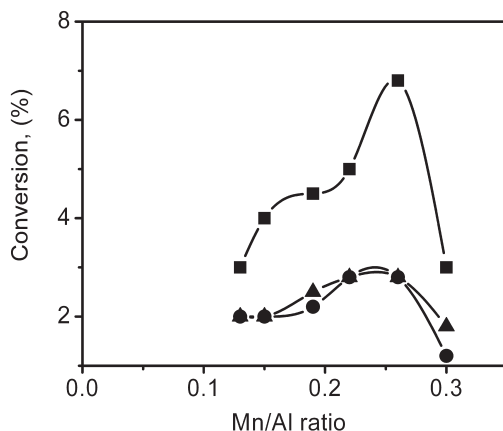


Figure 11. Conversion of N_2O as a function of Mn/Al molar ratio at 648 K, 1 h and 24000 GHSV (h^{-1}) for the first (■), second (▲) and third (●) catalytic cycle.

Figure 12 shows that during N_2O decomposition only N_2 is detected from the reactor outlet. This effect can be explained with the help of the proposed reaction mechanism. It is largely accepted that the mechanism reaction of N_2O decomposition occurs following the reactions:



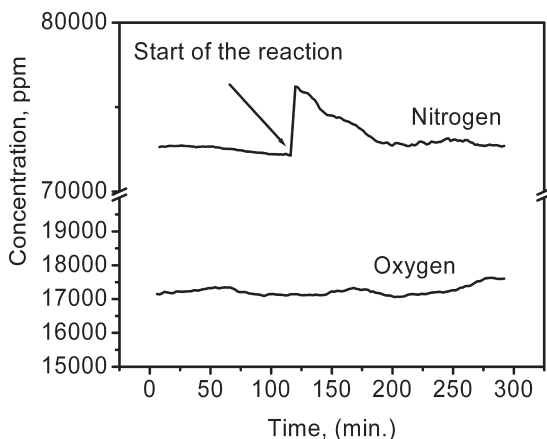


Figure 12. A typical GC signal for the N_2O exposure treatment using MnZ-0.22. N_2 and O_2 signal are presented.

According to this reaction mechanism, both N_2 and O_2 should be detected during N_2O decomposition. The absence of O_2 demonstrates that step (3) of the reaction mechanism is not taking place, which implies that the evolving O remains adsorbed to the catalyst. Knowing from blank experiments that the active phase is actually the manganese, we conclude that the O will remain adsorbed on the manganese center. The nature of the connection of this oxygen to the manganese is still to be determined.

In order to quantify the amount of oxygen deposited on the manganese centres we take in account that we know the amount of N_2O which is decomposed and that by the decomposition of a molecule of N_2O we obtain a $\frac{1}{2}$ O_2 molecule. We start these calculations by integrating the conversion profiles of each sample. This will give us the average conversion percentage of N_2O that reacts. By multiplying this value with the amount of N_2O that is introduced per minute in the reactor, we obtain the total amount of gas in grams that has disappeared during the reaction time of 1 h. From the total amount of reacted N_2O , the mass of oxygen is represented by a fraction of 0.36 ($16(1/2 \text{ mol O}_2) / 44(1 \text{ mol N}_2\text{O})$) from the total amount of N_2O . This will give us the amount of oxygen in grams obtained from the N_2O decomposition. In order to obtain the number of moles, the mass is divided by the atomic mass of oxygen (16). These numbers are presented in Table 4 as a function of the manganese loading and also as function of the catalytic

cycle.

Table 4. Quantification of the amount of O deposit on the catalyst during the N₂O exposure at 623K.

Sample code	Mol Mn *10 ⁻⁵	Mol O *10 ⁻⁷			O/Mn ratio Cycle 1
		Cycle 1	Cycle 2	Cycle 3	
MnZ-0.00	0	0	0	0	-
MnZ-0.13	1.6	26	17	15	0.22
MnZ-0.24	2.2	32	6	5	0.15
MnZ-0.26	2.4	49	9	11	0.21
MnZ-0.30	2.6	18	9	7	0.07

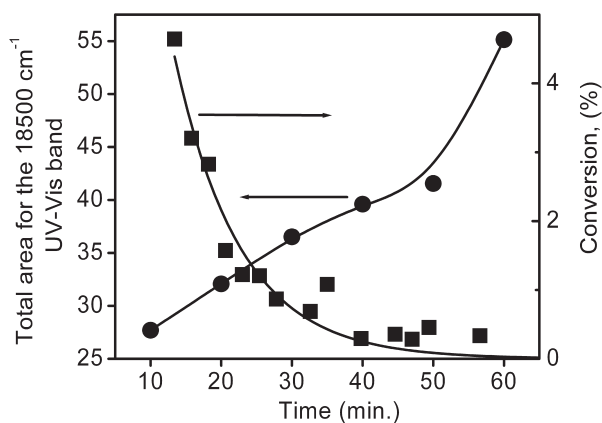


Figure 13. Total area of the UV-Vis band at 18500 cm⁻¹ (●) as a function of time under N₂O exposure compared with the N₂O conversion (■) for MnZ-0.15.

In Figure 13, we compare the N₂O conversion with the evolution of the UV-Vis band. We find that the active centers of the catalyst are consumed during conversion. This conclusion is in agreement with the reaction mechanism, taking into account that there is no oxygen detected at the output of the reactor.

In order to see if the formed oxygen can be desorbed from the active center, the sample was heated up to 773 K in a flow of inert gas. In the case of other α -oxygen generation materials, this oxygen can be desorbed at

temperatures higher the 523 K for Fe-ZSM-5 materials [12] or between 673 K to 723 K in the case of Cu-ZSM-5 [26]. No oxygen was observed desorbing from the sample indicating that the oxygen is linked through a chemical bond. The NO oxidation reaction was used as a test reaction in order to explore the possibility of using this formed oxygen to convert NO to NO₂.

NO oxidation

The NO oxidation reaction was performed after the N₂O decomposition at the same conditions of temperature and using a NO concentration of 3750 ppm. Blank experiment revealed that no reaction takes place when pure ZSM-5 was used. Also, an experiment in which the N₂O decomposition step was omitted showed no reactivity of the sample towards NO oxidation reaction. This proves that, if NO oxidation takes place, it will be due to the action of the oxygen evolved in the N₂O decomposition step. The only product observed at the output of the reactor is NO₂.

Similar to the N₂O reaction, the conversion of NO was followed during the reaction time. Figure 14 shows that the conversion has the same profile as the N₂O decomposition reaction.

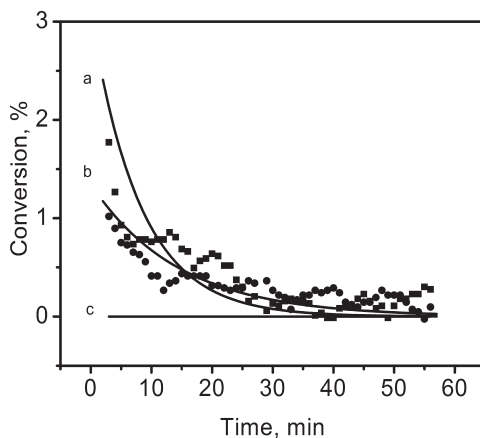


Figure 14. NO conversions profiles for sample MnZ-0.26 (a), MnZ-0.22 (b) and MnZ-0.0 (c) during 1 h of NO exposure at 623 K, 3750 ppm N₂O and 24000 GHSV (h⁻¹).

Figure 15 shows that the NO conversion rates are influenced by the manganese loading and the reaction cycle.

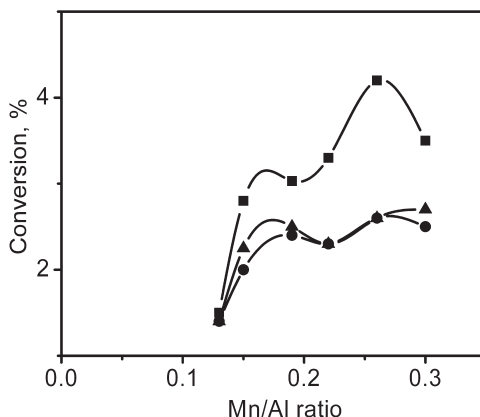


Figure 15. Conversion of NO as a function of the Mn/Al molar ratio at 648 K for the first (■), second (▲) and third (●) catalytic cycle.

To calculate how much of the deposited oxygen is extracted from the manganese centres during the NO treatments we can apply a similar principle as in the case of N_2O . We integrate the conversion profile of NO in order to have the average conversion percentage of NO that will react during the 1 hour period. We multiply this value with the amount of NO that is introduced per minute in the reactor and we obtain the total amount of NO in grams that reacts during 1 hour of treatment. Knowing that one molecule of NO will react with $\frac{1}{2} O_2$ to produce NO_2 we calculate the fraction of oxygen represented by this reaction ($16(1/2 \text{ mol } O_2) / 30(1 \text{ mol NO})$). This will give us the amount of oxygen in grams consumed by the NO oxidation. In order to obtain the number of moles we divide the mass to the atomic mass of oxygen (16). These numbers are presented in Table 5 as a function of the manganese loading and also as function of the catalytic cycle.

Table 5. Quantification of the amount of O removed from the catalyst during the NO exposure at 623 K.

Sample code	Mol Mn *10 ⁻⁵	Mol O *10 ⁻⁷			O/Mn ratio Cycle1
		Cycle 1	Cycle 2	Cycle 3	
MnZ-0.00	0	0	0	0	-
MnZ-0.13	1.6	7	13	8	0.06
MnZ-0.24	2.2	7	8	8	0.03
MnZ-0.26	2.4	9	10	13	0.04
MnZ-0.30	2.6	14	12	9	0.05

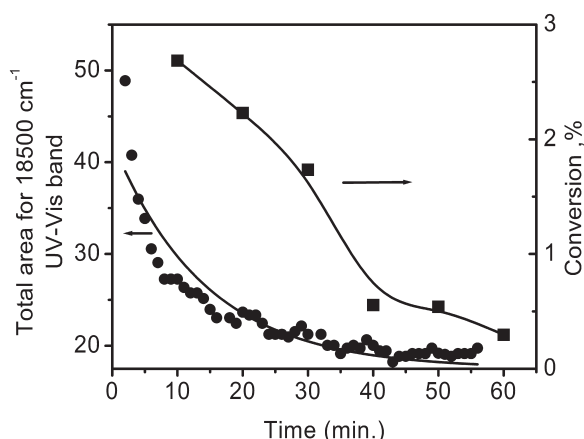
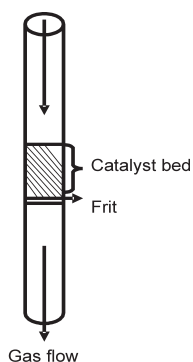


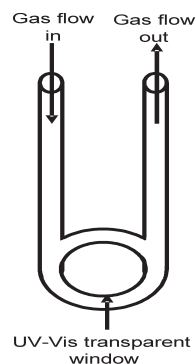
Figure 16. Total area of the UV-Vis band at 18500 cm^{-1} (●-) as a function of reaction time and the NO conversion (■-) evolution during 1 h reaction for MnZ-0.15 sample.

The observation that NO is reacting only with the oxygen bound to the Mn active site is also sustained by the comparison between the catalytic data to the UV-Vis results, where in the presence of NO the 18500 cm^{-1} absorption band decays due to the consumption of the “oxygen”, as can be observed in Figure 16.

The difference in the slope observed in Figure 16 can be explained by the fact that for the UV-Vis experiments we are using a reactor that is different from the one used during catalytic tests. In Scheme 1 we present the two types of reactor used for both experiments.



Scheme 1. Schematical representation of the types of reactors used for the catalytic tests (right) and for the UV-Vis monitoring experiments (left).



3.4 Discussion

Although XRF data proves that we are able to introduce manganese in ZSM-5 zeolites, the characteristics of these materials have to be discussed. From the XRD patterns, presented in Figure 1, we can establish that the zeolite matrix is not destroyed during the preparation and activation of the Mn-ZSM-5 samples. About the nature of the manganese present in the ZSM-5 based on the XRD measurements we can expect to have a high dispersion phase of manganese, due to the absence of characteristic peaks for manganese oxide phases. However, these results do not rule out the presence of manganese oxides phases having particle sizes under 4 nm, which represents the detection limit of the XRD technique.

In order to have a better understanding of the presence/dispersion of manganese in the zeolite, STEM-EELS experiments were performed. According to these results manganese is present at the surface of the zeolite crystal, namely in the top 2 nm of the surface. In order to determine if this manganese could exist as isolated species, we performed the following calculation.

We approximate the average zeolite crystal as a prism with dimensions of 30x30x60 nm. We calculate the total volume of the zeolite crystal, which is represented by the area of the base multiplied by the height of the crystal. This equals a value of 54000 nm³. Also, we calculate the volume represented by the top 2 nm layer of the zeolite crystal, giving us a value of 14760 nm³. This implies that the top 2 nm at the surface represents 27 % of the total volume of the crystal. If we assume that Al has a uniform distribution

over the entire crystal volume, the top 2 nm layer contains 27 % of the total amount of the Al of the zeolite crystal. By ion exchange we expect that one manganese atom will correspond to one Al atom. As observed from the STEM-EELS measurement, the manganese signal is present only at the surface. If we assume that all Al ions in the top 2 nm bind a Mn ion, we will have a sample-averaged Mn/Al ratio of 0.27. This value is close to the Mn/Al ratio obtained from XRF data (Mn/Al=0.24), which suggests that manganese could be present in the top 2 nm layer as isolated manganese sites. Here we note that the Al distribution over the zeolite crystal does not always have to be uniform. In some experimental studies, Al has a higher concentration at the top surface of the crystal [27]. It seems that during the ion exchange the manganese will interact with the first Al atom that is available, forming a region with high concentration of manganese, which acts as a barrier and stops the migration into the zeolite channels. This can explain the fact that we could not obtain higher manganese loadings, even if we use higher concentration of manganese in solution. In order to identify the oxidation state characteristic to the manganese present in the Mn-ZSM-5 samples we have to analyze the UV-Vis results. It is observed that during exposure to N_2O a relatively intense absorption band at $\sim 18500\text{ cm}^{-1}$ appears in the spectrum. Having a look at different manganese containing compounds (Table 2) we can establish that this band is more characteristic to compounds containing manganese in a Mn^{3+} oxidation state. Actually, the best model compound that fits our experimental data is represented by $Mn(PO_3)_3$ [24]. What makes this compound the best model is the fact that its UV-Vis-NIR spectrum has two main features: a broad band situated at $\sim 19500\text{ cm}^{-1}$ and another band situated at $\sim 20060\text{ cm}^{-1}$. This broad band at $\sim 19500\text{ cm}^{-1}$ is formed by the contribution on two transitions, similar to the band at $\sim 18500\text{ cm}^{-1}$ observed with our Mn-ZSM-5 samples (Figure 4). The shift of our band to a lower wavenumber can be explained by the fact that metal ions in zeolites have smaller crystal field splittings than bulk oxides, implying that the center of these peaks shifts to lower energy compared to bulk oxides, i.e. from $\sim 19500\text{ cm}^{-1}$ in $Mn(PO_3)_3$ to $\sim 18500\text{ cm}^{-1}$ in Mn-ZSM-5 systems. During NO exposure, this UV-Vis band disappears. The lack of structure in the obtained UV-Vis spectrum suggests that the new state of the manganese can be a $3d^5$ configuration that has only spin forbidden transitions characterized by a

weak intensity. Based on the reversibility nature of this UV-Vis band we can conclude that the manganese oxidation state is changing as a function of the gas exposure, from Mn^{2+} to Mn^{3+} during the N_2O exposure and from Mn^{3+} to Mn^{2+} when NO is introduced. In other words, N_2O is oxidizing the manganese to Mn^{3+} , while NO is reducing the manganese to Mn^{2+} form. However, NO exposure treatment is not reducing the entire amount of Mn^{3+} as suggested by Figure 7B and Figure 8. This correlation between the UV-Vis band and the oxidation state of the manganese were reported by Groothaert et al. [17,26,28] using Cu-ZSM-5 zeolite. They assigned the observed 22700 cm^{-1} UV-Vis band from Cu-ZSM-5 to a bis - (μ -oxo) di-copper core formed using the oxygen released during the N_2O decomposition. In this case, the oxidation state of the Cu is changing from Cu^+ to Cu^{2+} with the introduction of N_2O and back to Cu^+ after removal of the oxygen. The nature of this oxygen released the N_2O decomposition has a special nature due to the high reactivity character and is known as α -oxygen species. In the case of Cu-ZSM-5, the reactivity of this species was used to selectively oxidize methane to methanol in one step reaction [29].

In order to verify that our 18500 cm^{-1} UV-Vis band is indeed linked to the formation of α -oxygen species, we have investigated the formation of these species using the N_2O decomposition reaction. From trial experiments we observed that the lowest temperature at which the UV-Vis band is formed is 623 K. As usual in the commercial applications for catalysis, the lowest reaction temperature possible is preferred due to the energetical and economical reasons. This is why we decided to keep the 623 K temperature as a standard for all experiments. If we are to generate the α -oxygen, we will need to propose a reaction that can consume the formed α -oxygen species. One option is to use the methane as in the case of Cu-ZSM-5 materials, but due to the high temperature that we perform the test, even if we could oxidize the methane to methanol, this will not be stable at this temperature and will decompose to CO_2 and H_2O , or undergo polymerization reaction over the acidic centers of the zeolite to form different C_x compounds. Another option is to use NO, which will be oxidized by the α -oxygen to NO_2 . The results obtained from the catalytic tests confirm our supposition that indeed, the 18500 cm^{-1} UV-Vis band is linked to the formation of α -oxygen species. As seen in Table 4, we are able to deposit on the catalyst surface an average

of 0.2 moles of O per mole of Mn (with the exception of the MnZ-0.30 sample). During the NO exposure we observe that we remove only 0.06 moles of oxygen (an average of 1/3 from the deposited quantity). This fact suggests that from the ~20% of manganese sites on which the oxygen is deposited, only 1/3 is actually a α -oxygen site. That is only 1/3 of the total amount of the manganese centres is active in the second catalytic cycle, which is confirmed by the drop of the conversion rates from the first to the second catalytic cycle. However, in the second catalytic cycle we observe that we are able to remove almost the total amount of O deposit, which explains the similar values that we obtain for the second and third catalytic cycle.

This explains the presence of the 18500 cm^{-1} UV-Vis band in Figure 8, and further suggests that this UV-Vis band is linked to the presence of α -oxygen species. Also, taking as an example MnZ-0.13 we observe that during the NO exposure we are able to remove 1/3 of the deposited oxygen. However, during the second N_2O exposure we are able to deposit a quantity of oxygen much larger than what we removed during previous NO exposure. This indicates that not all the present manganese is active in the first catalytic run.

3.5. Concluding remarks

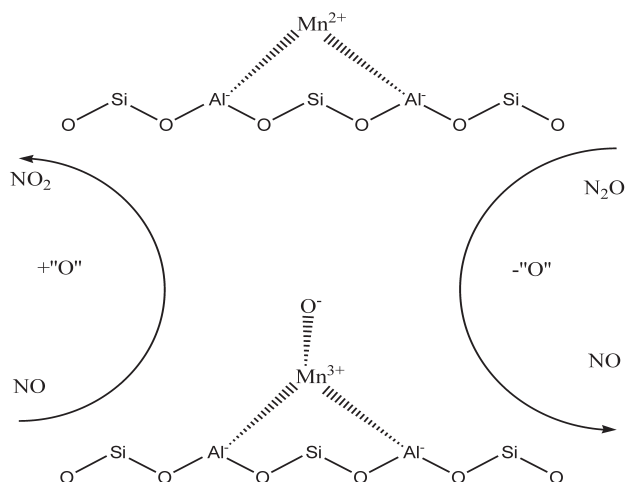
We have shown that we are able to prepare Mn-ZSM-5 zeolites that are active in the N_2O catalytic decomposition using an ion exchange procedure.

A very interesting result obtained was the generation of α -oxygen species during this reaction and the identification of a UV-Vis band located at 18500 cm^{-1} as an indication of the presence of this α -oxygen species at the active center. The reactivity of this α -oxygen species was demonstrated using NO oxidation as a test reaction.

STEM-EELS measurements show that manganese is spread in a very thin layer of maximum 2 nm over the external surface of the zeolite material as isolated manganese sites.

Based on the spectroscopic data acquired during the catalytic experiments, we are able to propose a scheme regarding the generation and removal of α -oxygen species during the N_2O decomposition/NO oxidation

reactions.



Scheme 2. Proposed scheme for the generation and removal of α -oxygen species during the N_2O decomposition/ NO oxidation reactions over Mn-ZSM-5.

Acknowledgments

Financial support was provided by the Netherlands Organisation for Scientific Research - Chemical Science (NWO-CW) and the Netherlands Research School Combination on Catalysis (NRSCC).

References

- [1] M. H. Thiemens; W. C. Troglor, *Science*, 251, **(1991)**, 932.
- [2] F. Kapteijn; J. Rodriguez-Mirasol; J. A. Moulijn, *Appl. Catal. B Envir.*, 9, **(1996)**, 25.
- [3] T. Yamashita; A. Vannice, *J. Catal.*, 161, **(1996)**, 254.
- [4] L. Singoredjo; R. Korver; F. Kapteijn; J. Moulijn, *Appl. Catal. B Envir.*, 1, **(1992)**, 297.
- [5] F. Kapteijn; A. D. Vanlangeveld; J. A. Moulijn; A. Andreini; M. A. Vuurman; A. M. Turek; J. M. Jehng; I. E. Wachs, *J. Catal. Lett.*, 150, **(1994)**, 94.
- [6] F. Kapteijn; L. Singoredjo; M. Vandriel; A. Andreini; J. A. Moulijn; G. Ramis; G. Busca, *J. Catal.*, 150, **(1994)**, 105.
- [7] F. Kapteijn; L. Singoredjo; A. Andreini; J. A. Moulijn, *Appl. Catal. B Envir.*, 3, **(1994)**, 173.

- [8] L. Singoredjo; F. Kapteijn, *Stud. Surf. Sci. Catal.*, 75, **(1993)**, 2705.
- [9] F. Kapteijn; L. Singoredjo; N. J. J. Dekker; J. A. Moulijn, *Ind. Eng. Chem. Res.*, 32, **(1993)**, 445.
- [10] A. Cimino; R. Bosco; V. Indovina; M. Schiavello. *J. Catal.*, 5, **(1966)**, 271.
- [11] F. S. Stone. *J. Solid State Chem.*, 12, **(1975)**, 271.
- [12] G. I. Panov; V. I. Sobolev; A. S. Kharitonov, *J. Molec. Catal.*, 61, **(1990)**, 85.
- [13] W. M. H. Sachtler; R. A. Van Santen; El-M.El-Malki, *J. Catal.*, 196, **(2000)**, 212.
- [14] K. A. Dubkov; V. I. Sobolev; G. I. Panov, *Kinet. Catal.*, 39, **(1998)**, 72.
- [15] B. R. Wood; J. A. Reimer; A. T. Bell; M. T. Janicke; K. C. Ott, *J. Catal.*, 225, **(2004)**, 300.
- [16] L. V. Pirutko; V. S. Chernyavsky; A. K. Uriarte; G. I. Panov, *Appl. Catal. A Gen.*, 227, **(2002)**, 143.
- [17] M. H. Groothaert; K. Lievens; H. Leeman; B. M. Weckhuysen; R. A. Schoonheydt, *J. Catal.*, 220, **(2003)**, 500.
- [18] Y. J. Li; J. N. Armor, *Appl. Catal. B Envir.*, 1, **(1992)**, L21.
- [19] G. W. Pratt; R. Coelho, *Phys. Rev.*, 116, **(1959)**, 281.
- [20] A. Mehra; P. Venkateswarlu, *J. Phys. Chem.*, 48, **(1968)**, 4381.
- [21] F. Milella; J. M. Gallardo-Amores; M. Baldi; G. Busca, *J. Mater. Chem.*, 8, **(1998)**, 2525.
- [22] D. S. McClure, *J. Phys. Chem.*, 36, **(1962)**, 2757.
- [23] N. Rajic; D. Stojakovic; S. Hocevar; V. Kaucic, *Zeolites*, 13, **(1993)**, 3849.
- [24] H. Thauern, *Phosphate des ein-und zweiwertigen Indium und Einbau von Chrom(III) und Mangan(III) in Indium(III)-phosphate*. PhD, Rheinischen Friedrich-Wilhelms-Universität Bonn, 2006.
- [25] S. Geschwind; K. M. P.; J. P. Remeika; D.L. Wood, *Phys. Rev.*, 126, **(1962)**, 1684.
- [26] M. H. Groothaert; K. Lievens; J. A. van Bokhoven; A. A. Battiston; B. M. Weckhuysen; K. Pierloot; R. A. Schoonheydt, *Chem. Phys. Chem.*, 4, **(2003)**, 626.
- [27] R. M. Dessau; E. W. Valyocsik; N. H. Goeke, *Zeolites*, 12, **(1992)**, 776.
- [28] M. H. Groothaert; A. Battiston; B. M. Weckhuysen; R. A. Schoonheydt, *J. Am. Chem. Soc.*, 125, **(2003)**, 7629.
- [29] M.H.Groothaert; P. J. Smeets; B. F. Sels; P. A. Jacobs; R. A. Schoonheydt, *J. Am. Chem. Soc.*, 127, **(2005)**, 1394.

On the Nature of Manganese in Mn-S-1 and Mn-ZSM-5 Zeolites

Abstract

Manganese-containing silicalite-1 (Mn-S-1) and Mn-ZSM-5 zeolites have been hydrothermally synthesized. The influence of the silicon source, the manganese source and the template were investigated. X-ray diffraction (XRD) shows that there is no effect of the incorporation of Mn on the crystal structure and lattice parameters. Scanning Electron Microscopy (SEM) shows that the morphology and texture of the zeolite crystals is strongly affected by the template used, but the texture is not visibly affected by the different sources of silica and manganese, nor by the addition of alumina. On the other hand, the combination of scanning transmission electron microscopy (STEM) electron energy-loss spectroscopy (EELS) shows that Mn is spread in an inhomogeneous manner over the zeolite material, including the existence of a 2-3 nm thin Mn-rich layer covering the Si-rich crystals.

4.1. Introduction

Microporous materials have great industrial importance, ranging from petroleum reforming and gas separation processes to the production of bulk and fine chemicals. This is true for pure silicalite (S-1), as well as its aluminium-doped analogue ZSM-5, both belonging to the MFI topology. In many cases, metal ions are added to the ZSM-5 structure. The preparation of these metal-doped ZSM-5 materials can make either use of direct synthesis, impregnation or ion exchange methods. Synthesis of e.g. titanium silicalite-1 [1] (TS-1) through Ti isomorphous substitution of the network silicon atoms opened a new era in the preparation and application of these metal-containing zeolites. Other important catalysts include Fe-ZSM-5 [2] and Cu-ZSM-5 [3]. In addition, a range of other metal ions is added to S-1 and ZSM-5 zeolites, for example the substitution of Si with B or Ge in the ZSM-5-zeolite yields a more selective membrane in separation of $n\text{-C}_4\text{H}_{10}/i\text{-C}_4\text{H}_{10}$ compared with S-1 [4]. The amount of the metal ions that are incorporated can strongly affect their activity, for example in the case of molybdenum incorporated in S-1, where a low loading of 0.5 wt% presents no activity, whereas a 11 wt% loading has excellent catalytic properties in the epoxidation of the olefins [5]. Cobalt-incorporated ZSM-5 has good performance in the propylene oligomerization and can be synthesized using rapid crystallization methods [6] or through direct synthesis from aqueous fluoride gels [7]. Fe-ZSM-5 systems are excellent catalysts in various applications, such as the decomposition of N_2O , the selective catalytic reduction of NO_x with hydrocarbons [8], the oxidation of benzene to phenol [9] and the oxidation of volatile organic compounds [10]. Much research is dedicated to the identification of the active sites in Cu-ZSM-5 and the NO decomposition reaction mechanism. A 100% selective conversion of NO into N_2 and O_2 can be achieved over Cu-ZSM-5 above 623 K with maximum activity in the temperature range 723– 773 K [11-13].

In contrast, only a few studies are published on Mn-doped zeolites, including the Selective Catalytic Reduction of NO_x using different hydrocarbons as propane [14] or methane [15,16], the epoxidation of styrene [17], the oxidation of SO_2 in the aqueous phase [18], the benzene hydroxylation to phenol [19], the simultaneous isomerization and dehydrogenation of n -

butane [20] or the oxidative conversion of methane [21]. A range of synthesis methods were developed, including the recrystallization of ion exchanged zeolite systems [22], direct synthesis from aqueous fluoride gels [7] and hydrothermal synthesis [23]. In this chapter the influence of the silicon source (Si), manganese source (Mn), and the structure-directing agent for MnS-1 and Mn-ZSM-5 synthesis are investigated.

Scientific questions that we would like to address include: (a) How much Mn is inserted?; (b) What is the valence state of Mn?; (c) Do the Mn ions modify the structure and morphology?; (d) How are the Mn ions spread over the material? Question (a) will be answered by elemental analysis, for example X-Ray Fluorescence (XRF). Structural characteristics have been investigated with X-Ray Diffraction (XRD) and the morphology with Scanning Electron Microscopy (SEM). The spreading of Mn over the zeolite needs a tool that has both the capability for elemental analysis and a good spatial resolution. This combination of characterization possibilities is provided by Scanning Transmission Electron Microscopy (STEM), equipped with an Electron Energy Loss Spectroscopy (EELS) detector. The combination of these characterization tools provides a detailed picture of the nature of the Mn in both S-1 and ZSM-5 zeolite and as such allows investigating the synthesis procedure on the incorporation process.

4.2. Experiment

4.2.1. Catalyst preparation

Mn-S-1 and Mn-ZSM-5 zeolite were hydrothermally synthesized from a gel containing a manganese source, a silica source, a template molecule plus an aluminium source for the ZSM-5 synthesis. In order to optimize the final structure, different sources of silica and manganese, as well as different zeolite templates were used (Table 1). The silica sources used were SiO_2 (CabOsil, Grade M5) and tetraethyl orthosilicate (TEOS), from Aldrich (> 98%). As manganese sources we have used tetrahydrated manganese acetate ($\text{Mn}(\text{ac})_2 \cdot 4\text{H}_2\text{O}$), from Acros (> 99%) and manganese nitrate ($\text{Mn}(\text{NO}_3)_2 \cdot 9\text{H}_2\text{O}$), from Aldrich (> 98%). Aluminium nitrate ($\text{Al}(\text{NO}_3)_3 \cdot 9\text{H}_2\text{O}$), from Aldrich (98%+) was used as Al source. Two different templates were

used, tetraethyl ammonium hydroxide (TEAOH) (Alfa Aesar, 35% w/w in water) and tetrapropyl ammonium hydroxide (TPAOH) (Alfa Aesar, 40% w/w in water). In addition, NaCl (Alfa Aesar, > 99%) and H₂O were used in the synthesis. The molar composition ratio of Mn-S-1 was 1:50:15 for MnO: SiO₂: template dissolved within 2000 units of water. When ZSM-5 is prepared the same ratio was used, were 1 unit of Al₂O₃ was added.

In case CabOsil was used as silica source, the gel was prepared by dissolving the NaCl in 2/3 of the total amount of the water. The template molecules (TEAOH or TPAOH) were added and 90% of the silica source was added dropwise during heating and steering in order to facilitate the dissolution of the silica. The Mn(ac)₂, respectively, Mn(NO₃)₂ was dissolved in the remaining 1/3 of the water and, in case of ZSM-5, Al(NO₃)₃ was added. When the composition containing the silica source becomes a clear solution and all the silica was dissolved, the manganese solution was added dropwise under continuous steering. After the manganese addition, the remaining 10% of the silica source was added and the gel was kept under steering for another hour in order to have a homogeneous gel. When TEOS was used as silica source, a different gel preparation method was used. NaCl was added to the TEOS and the template solution. The Mn and (if used) the Al sources were dissolved in the total volume of water. The Mn/Al solution was dropwise added to the Si/template solution under continuous steering for 1 h. The gel resulting from both methods was transferred to a Teflon autoclave, which was heated in static conditions for 3 days at 448 K. The template was removed by pyrolysis in a dried flow of nitrogen at 793 K for 2 h and consecutive calcination in a flow of air at the same temperature for another 2.5 h.

Table 1. Samples obtained by combining different parameters as silica source, manganese source and template molecules, associated with their corresponding sample code. The code **CEA** stands for e.g. **C**abOsil-**TEA**OH-**A**cetate, etc.

Al source	Si source	Template	Mn source	Sample code
-	CabOsil	TEAOH	Acetate	MnS1 ^{CEA}
			Nitrate	MnS1 ^{CEN}
-	TEOS	TEAOH	Acetate	MnS1 ^{TEA}
			Nitrate	MnS1 ^{TEN}
-	CabOsil	TPAOH	Acetate	MnS1 ^{CPA}
			Nitrate	MnS1 ^{CPN}
-	TEOS	TPAOH	Acetate	MnS1 ^{TPA}
			Nitrate	MnS1 ^{TPN}
Nitrate	TEOS	TPAOH	Acetate	Mn-ZSM5 ^{TPA}
			Nitrate	Mn-ZSM5 ^{TPN}

4.2.2. Characterization techniques

X-ray fluorescence spectroscopy

Elemental analysis was carried out using a Goffin Meyvis X-lab 2000 X-Ray Fluorescence (XRF) spectrometer in order to determine the Mn loading and the Si and Al content in the synthesized materials.

X-ray diffraction

X-Ray Diffraction (XRD) was measured using an Enraf-Nonius CPS 120 powder diffraction apparatus with Cu K α radiation ($\lambda=1.540$ Å). XRD patterns were measured of Mn-S-1 and Mn-ZSM-5 materials *as-made* and template free. The XRD patterns were collected in the 2θ range of 5-35 degree in steps of 0.01 degree with 2s/step.

Scanning electron microscopy

The size and morphology of as-synthesized and template free crystals were investigated using a Scanning Electron Microscope (SEM). Scanning Electron Micrographs were obtained on a JEOL 840 electron microscope at an accelerating voltage of 15 kV. The samples were sputtered with gold before taking the images.

Transmission electron microscopy and electron energy loss spectroscopy

Scanning Transmission Electron Microscopy (STEM) - Electron Energy-Loss Spectroscopy (EELS) measurements were performed in Orsay (France) with a 100 keV STEM instrument (VG HB 501) equipped with a field emission electron source. Mounted on the STEM instrument was a parallel electron energy-loss spectrometer (Gatan 666) optically coupled to a CCD camera generating an EELS spectrum with a 0.5-0.7 eV energy resolution and 0.5 nm spatial resolution within a typical acquisition time down to 1 ms per pixel [24]. In these experiments, the oxygen K edge, silicon L edge and manganese L edge were monitored. The solids were first sonicated in ethanol and then dropped on a holey amorphous carbon film supported on a copper grid. After the sample was scanned, appropriate areas were selected for the measurement of detailed 2-D STEM-EELS images. An energy range of 15 eV was used to quantify the EELS spectra.

Diffuse reflectance UV-Vis-NIR spectroscopy

After template removal, the samples were introduced in a quartz flow cell equipped with a UV-Vis-NIR transparent window. Two O-ring valves were used in order to make the cell airtight and allow us to make in-situ measurements. UV-Vis-NIR diffuse reflectance (DR) spectra were recorded on a Varian Cary 500 spectrometer in the range 5000 – 50000 cm⁻¹ (200-2000 nm).

Table 2. Overview of the characterization techniques used for each of the prepared samples.

Sample code	XRF	XRD	SEM	STEM - EELS	UV-Vis
MnS1 ^{CEA}	am	am, tf	am		
MnS1 ^{CEN}	am	am, tf	am		
MnS1 ^{TEA}	am	am, tf			
MnS1 ^{TEN}	am	am, tf			
MnS1 ^{CPA}	am	am, tf			
MnS1 ^{CPN}	am	am, tf			tf,N ₂ O/NO
MnS1 ^{TPA}	am	am, tf	am		
MnS1 ^{TPN}	am	am, tf			tf,N ₂ O/ NO
Mn-ZSM5 ^{TPA}	am	am, tf	tf	tf	
Mn-ZSM5 ^{TPN}	am	am, tf			

am=as-made; tf= template free; N₂O/NO= after treatment with N₂O/NO

Catalytic testing

Catalytic activity was measured using a quartz flow reactor in which typically 0.1 g catalyst was placed on a frit. The reactor was placed in an oven that can be controlled within ± 1 K from the desired temperature using a West 6810 temperature controller. Concentrations and flow rate (total flow rate of 80 ml/min) were controlled by means of Brooks mass flow controllers. The inlet concentration of N₂O was 3750 ppm balanced with He until the desired flow. Before each run, the catalyst was pre-treated by heating up to 673 K in a He flow for 1 h. Then the catalyst was cooled down to the reaction temperature. A typical catalytic experiment consists of exposures to N₂O for 1 h, followed for 10 min flushing with He in order to eliminate the traces of N₂O from the system. At the end of the flushing period, 3750 ppm of NO was introduced in the gas flow for 1 h, followed again by a 10 min period of flushing with He. These steps were repeated three times, generating three consecutive cycles of N₂O/NO treatments. Product analysis was carried out using an Interscience Compact GC system, equipped with two different columns (a Molsieve 5A and a Porabond Q) each having a TCD detector. In

addition, a Thermo Environment Instruments 42C NO_x chemoluminescence analyzer was connected in parallel with the GC in order to determine the NO and NO_x concentrations and could be operated simultaneously.

4.3. Results

4.3.1. Synthesis using TEOAH and TPAOH

In the first part of the work, the synthesis methods using respectively TEOAH and TPAOH as structure directing agents are compared, using XRD, XRF and SEM.

Table 3 shows the XRF analysis of the Mn-S-1 and Mn-ZSM-5 samples under investigation. The largest effect on the Si/Mn ratio is the nature of the Mn source, with nitrate yielding a Mn content of only 33%-38% of the corresponding acetate source. We conclude that with nitrate only one third of the Mn incorporates compared to acetate. The difference between CabOsil and TEOS is small (~15%), and the effect of aluminium is small, yielding a reduction of the Mn content by ~15%.

Table 3. Elementary analysis by XRF of the MnS-1 and Mn-ZSM-5 samples prepared using TPAOH. In case of ZSM-5, Al₂O₃ is added to the overall weight percent.

Sample	wt % Si	wt% Mn(/Al)	wt % SiO ₂ +MnO*	Si/Mn (Si/Al)
Start*	45.6	1.8	100	50
MnS-1^{CPA}	40.5	2.7	90	30
MnS-1 ^{CPN}	31.2	0.9	68	68
MnS-1 ^{TPA}	36.7	2.1	81	34
MnS-1 ^{TPN}	35.2	0.8	76	86
Start*	44.8	1.8/(0.8)	100	50/(50)
Mn-ZSM-5 ^{TPA}	32.1	1.5/(0.5)	72	42/(37)
Mn-ZSM-5 ^{TPN}	38.0	1.0/(0.5)	84	74/(43)

* The 'start' numbers have been calculated from the theoretical amounts of the start-materials used.

The use of TEAOH as template

Tušar et al. [23] reported for the first time the synthesis of Mn-ZSM-5 materials using TEAOH as a structure directing agent. Figure 1 shows the XRD pattern and SEM image of MnS-1^{CEA}. The broad rising background in XRD shows the presence of an amorphous phase and the superimposed sharp lines indicates the simultaneous presence of a crystalline phase. In addition, the SEM image shows the presence of amorphous-looking small particles. The MnS-1^{CEA} sample has been synthesized a number of times and Figure 2 presents XRD patterns for different samples prepared using the same preparation protocol. It is observed that the reproducibility of the method is poor. The top XRD pattern indicates mainly an amorphous phase, whereas the bottom spectrum shows mainly the crystalline phase with a minor amorphous fraction.

In the case of TEOS as silica source and Mn nitrate as Mn source, things got even worse and Figure 3 shows that for those samples only an amorphous phase was synthesized.

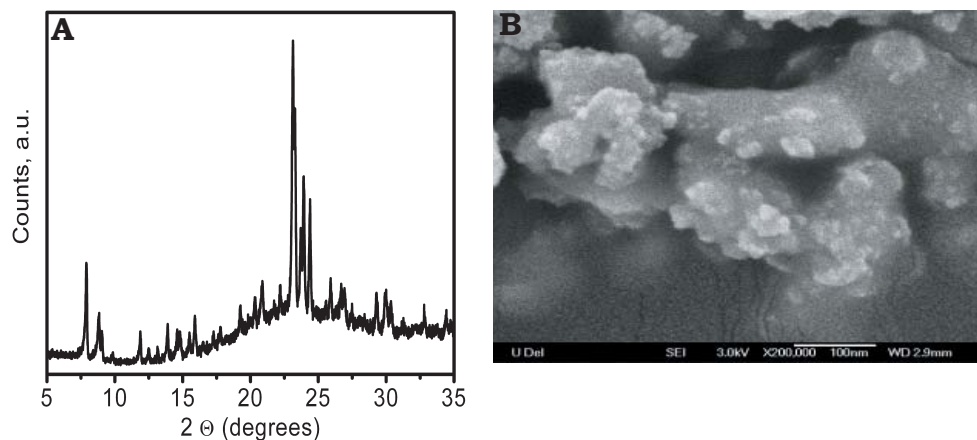


Figure 1. XRD pattern (A) and SEM picture (B) of the as-synthesized MnS-1^{CEA} sample when TEAOH is used as a structure directing agent.

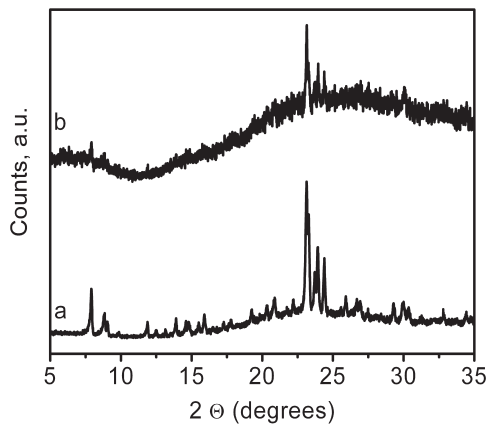


Figure 2. XRD patterns of the as-synthesized MnS-1^{CEA} sample obtained when reproducibility was investigated.

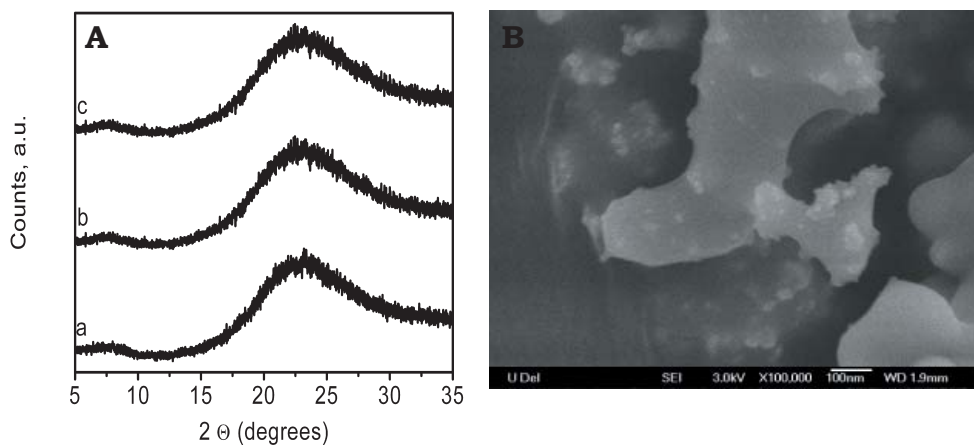


Figure 3. (A) XRD patterns of the as-synthesized MnS-1^{TEA} (a), MnS-1^{TEN} (b) and MnS-1^{CEN} (c) samples obtained using TEAOH as a structure directing agent. (B) SEM image of the as-synthesized MnS-1^{TEA} corresponding to the XRD pattern (a).

The use of TPAOH as template

Searching through the zeolite synthesis literature it was observed that there is another compound, which can be used for making MFI zeolites: This is TPAOH. Figure 4 shows that the use of TPAOH yields a single-phase crystalline material. The SEM image shows beautiful rounded crystals of approximately 200 nm diameter. Figure 5 shows that this single-phase material was also obtained when the alternative silica and manganese sources were used indicating that the TPAOH template is in all cases a successful directing agent for the synthesis of MnS-1 materials.

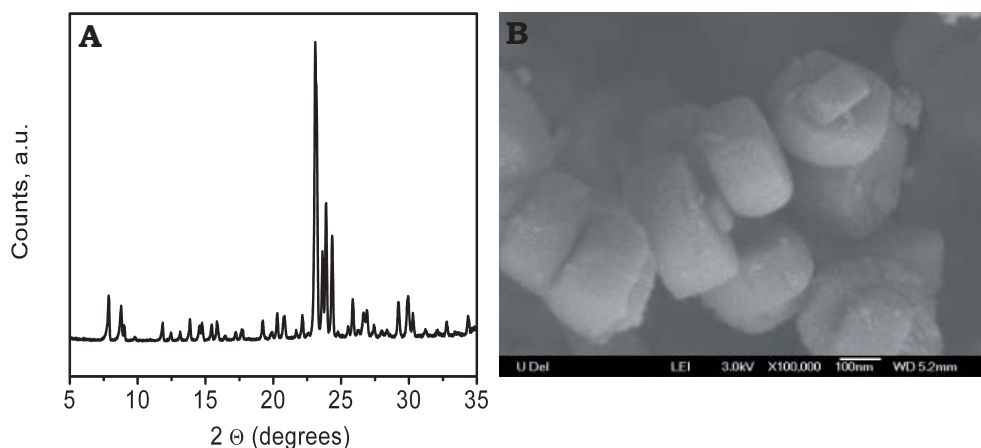


Figure 4. XRD pattern (A) and SEM picture (B) of the as-synthesized MnS-1^{CPA} sample when TPAOH is used as a structure directing agent.

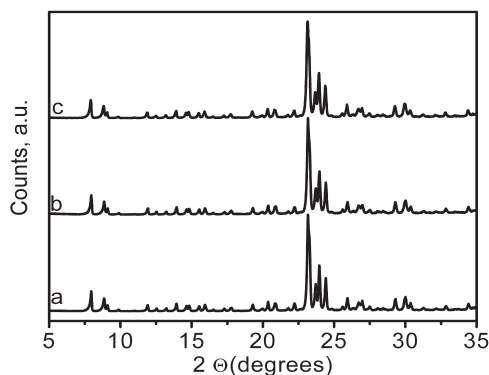


Figure 5. XRD patterns of the as-synthesized MnS-1^{CPA} (a), MnS-1^{TPN} (b) and MnS-1^{TPA} (c) samples obtained using TPAOH as a structure directing agent.

The XRD patterns have been further analyzed. Figure 6 presents the diffraction pattern of a pure ZSM-5 phase [25] along with the diffraction pattern for manganese oxide phases MnO (99%, Aldrich), Mn_2O_3 (99%, Aldrich) and MnO_2 (99.99%, Aldrich) and compared with $\text{MnS-1}^{\text{TPA}}$ and $\text{Mn-ZSM-5}^{\text{TPA}}$ samples.

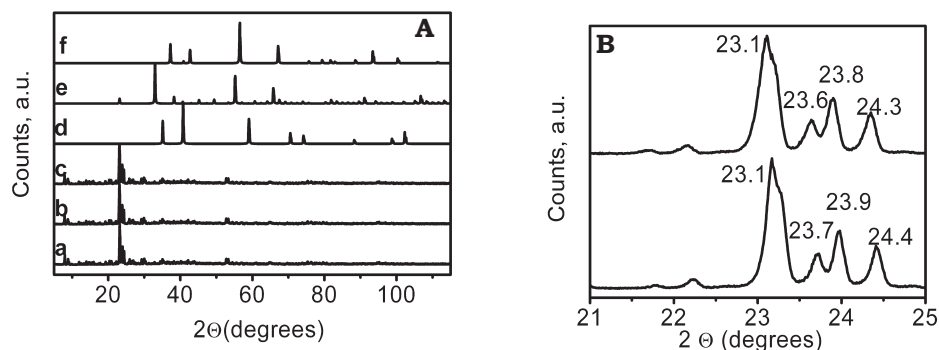


Figure 6. (A) XRD patterns of $\text{MnS-1}^{\text{TPA}}$ (a) and $\text{Mn-ZSM-5}^{\text{TPA}}$ (b) compared with diffraction pattern of pure phase compounds as ZSM-5 [25] (c) structure and different manganese oxide phases-MnO (d), Mn_2O_3 (e) and MnO_2 (f). (B) Zoom in the region of 23 to 25 theta for $\text{MnS-1}^{\text{TPA}}$ (top pattern) and $\text{Mn-ZSM-5}^{\text{TPA}}$ (bottom pattern).

No evidence for the presence of other manganese oxide phases is obtained and the MFI structure is confirmed as seen from the characteristic MFI region between of 23 to 25 degrees (Figure 6B). The small systematic shift of 0.07 2θ degrees observed lies within the experimental accuracy.

Figure 7 shows the XRD pattern and SEM picture of $\text{Mn-ZSM-5}^{\text{TPA}}$ after template removal. As seen, the removal of the template has no detectable influence over the peak positions. The intensity of the small-angle peaks (7 to 10 degrees) is increased, while the intensity of the wide angle peaks, (23 to 25 degrees) is decreased. These intensity changes can be viewed as an increase in the long range order and a decrease in the short range order. This behaviour is expected to occur when the structure directing agent is removed. Also, from SEM picture we can observe a large distribution of crystal sizes, having dimensions between 200 to 600 nm.

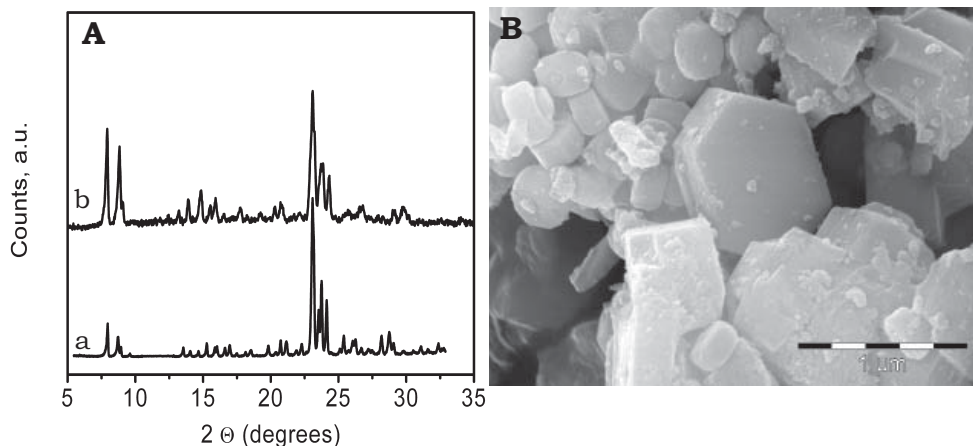


Figure 7. XRD pattern (A) of Mn-ZSM-5^{TPA} as synthesized (a) and Mn-ZSM-5^{TPA} template free (b) along with a SEM picture (B) of Mn-ZSM-5^{TPA} after template removal.

4.3.3. Scanning transmission electron microscopy electron energy-loss spectroscopy

STEM-EELS measurements were performed in order to determine the distribution of manganese in the zeolite crystals. STEM has a spatial resolution of 0.5 nm and detailed Oxygen K edge (530 eV), Silicon L edge (100 eV) and Manganese L edge (640 eV) EELS spectra have been measured. Quantification of the EELS spectra allows for a detailed 2D scan of the relative amounts of O, Si and Mn. Energy ranges of 15 eV at the O, Si and Mn edges have been used to quantify their relative amounts. In Figure 8 we show the 100 nm by 100 nm EELS chemical maps of Mn-ZSM-5^{TPA} after template removal. Maps are given for oxygen (top-left), manganese (top-right), silicon (bottom-left) and the Si/Mn ratio (bottom-right). The Mn/Si ratio has been quantified by first normalizing the Mn and Si maps to 1.0, followed by the calculation of $(\text{Mn}-\text{Si})/(\text{Mn}+\text{Si})$. This yields the excess Mn, respectively Si for each pixel. It is noted that the STEM-EELS experiments are performed in transmission and hence indicate elemental columns through the crystals. This implies that one only obtains a clear distinction between a Mn-rich

domain and a Si-rich domain if their interface lies in the vertical direction of the electron beam.

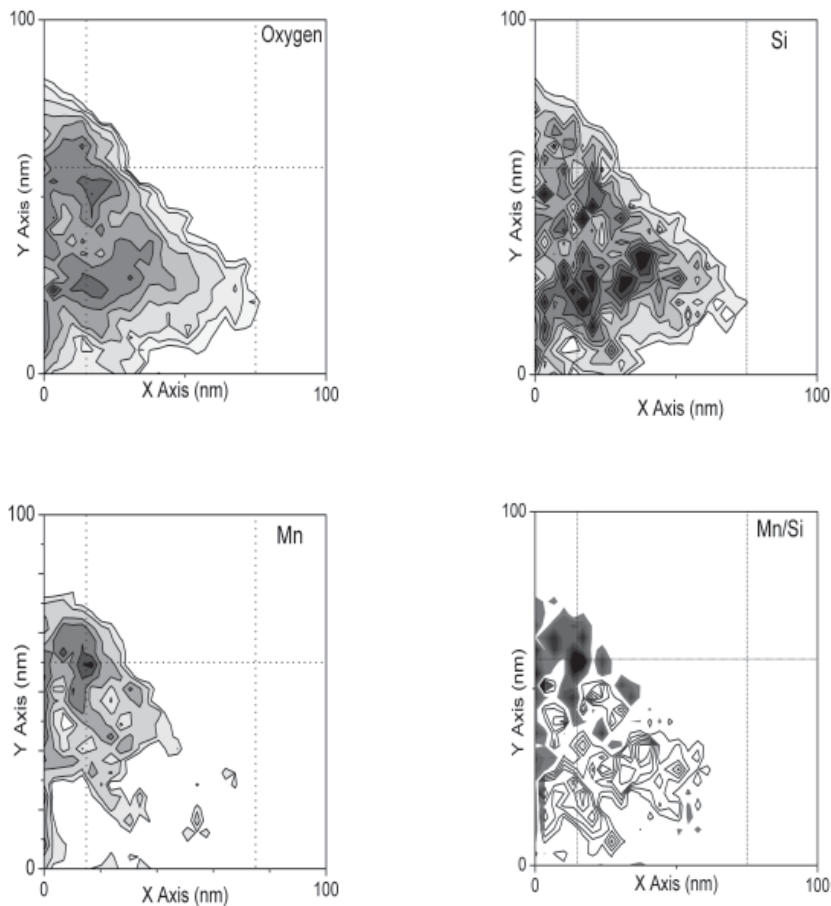


Figure 8. Top: Chemical maps of Mn-ZSM-5^{TPA} showing O (top-left), Mn (top-right), Si (bottom-left) and the Mn/Si ratio (bottom-right). A 100x100nm cross-section is shown. The dashed lines are a guide to the eye and indicate a Mn nanoparticle (top-left) and the boundary of the crystal. A comparison of the Mn/Si ratio calculated as $(\text{Mn}-\text{Si})/(\text{Mn}+\text{Si})$ with relative excess Mn given in gray-scale and excess Si with contour lines.

The oxygen map shows the distribution of oxygen atoms. The outer boundary of the oxygen map can be interpreted as the edge of the Mn-ZSM-5^{TPA} particle and the intensity as the samples thickness. At first inspection, the Si map seems to follow the oxygen map, indicating the SiO₂ bulk material of the zeolite. The manganese map shows high Mn concentration in the top left of the zeolite particle. At the position indicated at the crossing of the dashed lines, the Mn concentration is highest and exactly at this point the Si concentration has a minimum. This effect is highlighted by the (normalized) Mn/Si ratio map. One observes areas of excess of Mn, where the Mn seems to be interwoven with Si, suggesting the intergrowth of MnO_x particles with the zeolite. Similar intergrowth and MnO_x particles were seen for different position for five different zeolite crystals.

4.3.4. UV-Vis-NIR Diffuse Reflectance Spectroscopy

Figure 9 shows that UV-Vis-NIR DRS measurements of the template free MnS1^{TPA}. An absorption band at 20200 cm⁻¹ was observed, which is characteristic for a ${}^5E_g \rightarrow {}^5T_{2g}$ transition of (distorted) trivalent manganese. A similar band has been observed for Mn^{III}/Al₂O₃ [26] and Mn(PO₃)₃ [27]. More details are given in Table 2 of Chapter 3. Treatments of the sample with N₂O and with NO have no effect on the shape and intensity of the UV-Vis-NIR DRS spectrum. This is illustrated in Figure 9. The Mn-ZSM-5^{TPA} sample shows similar UV-Vis-NIR DRS spectra, with the mention that the band at 20200 cm⁻¹ has a lower intensity (not shown). During N₂O and NO treatments, the Mn-ZSM-5^{TPA} sample shows also the same inert behavior as in the case of the silicalite.

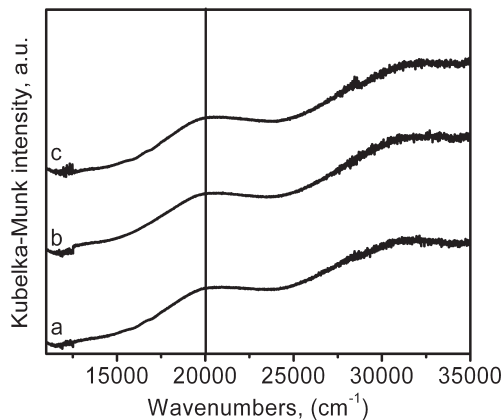


Figure 9. UV-Vis-NIR DR spectra of the MnS-1^{TPA} (tf) sample at 623 K (a) and after 1 h N₂O (b) and 1 h NO (c) treatments.

4.4. Catalytic testing

N₂O decomposition

Figure 10 presents the conversion profiles for N₂O decomposition reaction for MnS-1^{TPA} and Mn-ZSM-5^{TPA} both synthesized materials and a blank sample that consist of commercially available ZSM-5. As is evident from the figure, the data are scattered, making an accurate analysis difficult.

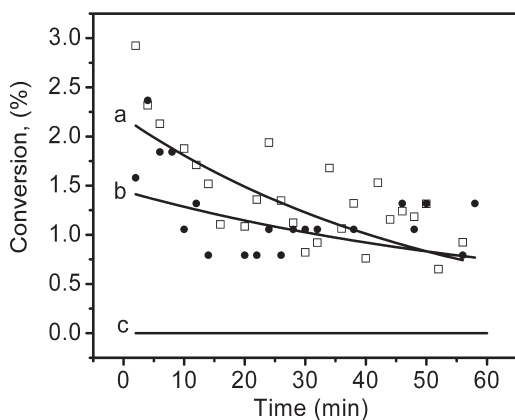


Figure 10. N₂O conversion profiles for sample MnS-1^{TPA} (a-□-), Mn-ZSM-5^{TPA} (b-●-) and ZSM-5 (c) during 1 h of N₂O decomposition reaction at 623 K, 3750 ppm N₂O and GHSV of 24000h⁻¹.

It is noticed that the blank sample presents no activity towards N_2O decomposition, while MnS-1^{TPA} presents a somewhat higher activity than Mn-ZSM-5^{TPA}. As notice in the N_2O conversion profiles after 10 minutes a steady state level is reached with a conversion value of 1.5 % for MnS-1^{TPA} and 1% for Mn-ZSM-5^{TPA}.

The only observed products formed during these catalytic tests were nitrogen and oxygen, according to the decomposition reaction:



During multiple catalytic cycles, no significant decrease in the activity is observed for both MnS-1^{TPA} and Mn-ZSM-5^{TPA}. Figure 11 shows the results from MnS-1^{TPA}, which again are rather scattered preventing a firm conclusion.

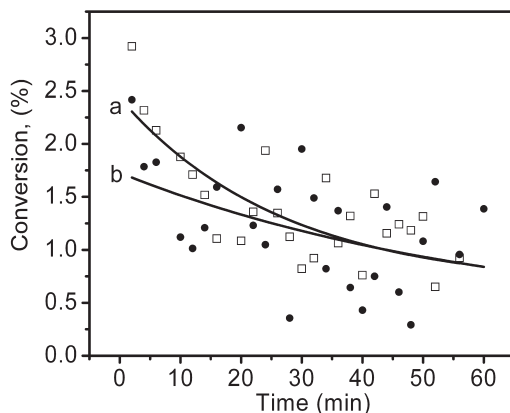


Figure 11. N_2O conversion profiles for sample MnS-1^{TPA} during 1 h of N_2O decomposition reaction at 623 K, 3750 ppm N_2O and GHSV of 24000h⁻¹ for the first (a-□-) and second (b-●-) catalytic cycle. The third cycle has a similar behavior as the second catalytic cycle (not shown).

NO oxidation

As stated in the experimental section, the introduction of NO takes place after the N_2O exposure and is carried out at the same reaction conditions as the N_2O decomposition reaction.

As we can observe in Figure 12, MnS-1^{TPA} sample presents a higher activity compared to Mn-ZSM-5^{TPA} for the oxidation on NO. However, both samples show the same profile, with an induction time of about 5 min, after which the activity of these materials reaches a stable value.

The low activity observed for Mn-ZSM-5^{TPA} sample is maintained also during multiple catalytic cycles, while the MnS-1^{TPA} sample presents a small

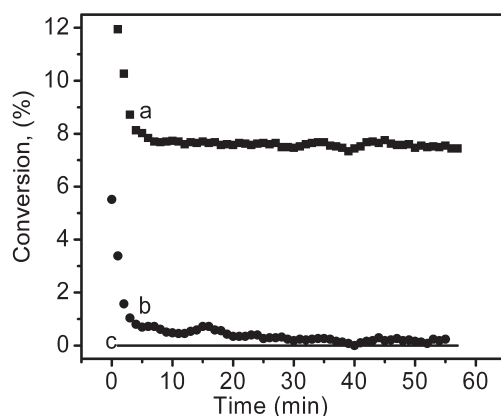


Figure 12. NO conversion profiles for sample MnS-1^{TPA} (a), Mn-ZSM-5^{TPA} (b) and ZSM-5 (c) during 1 h of NO exposure at 623 K, 3750 ppm NO and GHSV of 24000h⁻¹.

decrease of the activity with an increasing number of catalytic cycles.

An unexpected result was observed during this reaction, namely, that the only products of this reaction were NO_2 and N_2O . The presence of N_2O in the reactor output gas indicates the possibility that NO is involved in a disproportionation reaction.

Figure 13 presents the concentrations observed for the N_2O and NO_2 compared with the amount of NO consumed during this reaction.

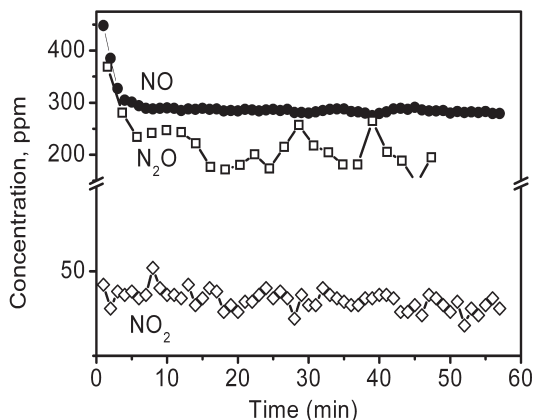


Figure 13. Concentration profiles for N_2O (\square -) and NO_2 (\diamond -) as observed at the output of the reactor, compared with the amount of NO (\bullet -) consumed for sample $MnS-1^{TPA}$ during 1 h of NO exposure at 623 K, 3750 ppm NO and GHSV of 24000 h^{-1} .

A similar behavior has been observed by Bell et al. [28], who investigated NO adsorption over Mn-ZSM-5 samples and observed traces of N_2O and NO_2 while desorption of NO was carried out at different temperature .

Discussion

1. Comparison of TEOH and TPAOH

Hydrothermal synthesis of MnS-1 using TEOH as a template showed that the material that we obtained is characterized by the presence of both amorphous and crystalline phases (Figure 1), similar to results obtained by Tusar et al [23]. The simultaneous formation of both amorphous and crystalline phase can be explained by the fact that TEOH exists in solution in two conformations, tt. tt and tg. tg as demonstrated by Naudin et al.[29]. This hypothesis was confirmed recently by O'Brien et al. [30] who found that depending on the conformation isomer of TEOH present in solution, different types of molecular sieves can be obtained. The influence of these two isomers can explain also the poor reproducibility observed for this

preparation procedure. On the other hand, the use of TPAOH during the synthesis procedure yields a single-phase crystalline material (Figure 4). Based on this result it can be stated that the use of TPAOH as a structure directing agent is not successful for the synthesis of MnS-1 materials.

2. Position of the Mn in Mn-ZSM-5 and MnS-1

For a better understanding of the nature of the manganese in these materials, a Rietveld refinement of the XRD patterns was performed. The results are presented in Table 4.

Table 4. Results of the Rietveld refinement for MnS-1^{TPA} and Mn-ZSM-5^{TPA} as compared with pure ZSM-5 presented in the crystallographic database [25]. The Rietveld refinement has been explained in Chapter 2.

Sample	Mn Loading	Cell parameters			
	(wt %)	α	a	b	c
MFI[25]	0	90	20.02	19.89	13.38
MnS-1 ^{TPA}	1.8	90	20.02	19.90	13.38
Mn-ZSM-5 ^{TPA}	1.5	90	20.02	19.91	13.39

These results imply that no detectable influence of Mn on the lattice was observed. The inclusion of transition metal ions has been correlated with a change in the unit cell dimensions as discussed by Weckhuysen et al. [31]. Assuming a similar effect on MFI compared to the microporous aluminophosphate materials as discussed in reference [31] one would expect a change of the cell parameter (a) from 20.02 to 20.06 for a 1.8 wt% loading. This increase would have been detectable from the Rietveld analysis. The absence of this influence on the lattice parameters suggests that the loading of the manganese in the zeolite framework is less than the total loading of the sample.

Using STEM-EELS measurement we were able to construct chemical maps for the Mn-ZSM-5^{TPA} sample. Having the individual maps for manganese and silicon one can construct a relative comparison of the Mn/Si ratio by using a mathematical procedure as presented in the STEM-

EELS section. After normalization to 1 of the EELS signal, by calculating the $(\text{Mn-Si})/(\text{Mn+Si})$ ratio, we obtain values in the range of -1 and 1. The values included in the -1 to 0 range are representing regions where silicon have a higher concentration than Mn, where the values contained in the 0 to 1 range are representing the regions where manganese has a higher concentration compared to silicon. By plotting these values we obtain a relative Mn/Si ratio map (see Figure 11 bottom-right). This map provides the answer to the question regarding the position of the manganese in Mn-ZSM-5 samples indicating the presence of manganese-rich domains along with silicon-rich domains, implying a non-equal distribution of Mn throughout the Mn-ZSM-5^{TPA} sample.

The UV-Vis spectra revealed an absorption band situated at 20200 cm^{-1} , which is characteristic for compounds containing Mn^{3+} (Table 2 of Chapter 3). The exposure of the samples to N_2O and NO has no effect on the observed UV-Vis band, indicating that these materials are not able to produce α -oxygen species.

This speculation is confirmed by the catalytic testing of the materials. During exposure to N_2O , MnS-1^{TPA} and Mn-ZSM-5^{TPA} are presenting modest conversion values (Figure 10).

However, an unexpected result was obtained when MnS-1^{TPA} was exposed to NO. It seems that NO is involved in a disproportionation reaction, as suggested by the presence of both N_2O and NO_2 in the output gas (Figure 13). With a conversion rate of ~8 %, this material has a selectivity to N_2O of ~75 % and to NO_2 of 16 %. These high selectivities suggest that this material could potentially be used as a novel NO catalyst removal, where N_2O can be transformed to N_2 and O_2 by another type of catalyst, while NO_2 can be purified and used further on.

4.5. Concluding remarks

We have shown that the Mn source is important for the synthesis, with Mn-acetate yielding the highest degree of incorporation. SEM showed that the texture of the crystals is strongly affected by the template used, but the texture is not affected by the different sources of silica and manganese, nor by the addition of alumina or the template removal. The same conclusion

applies to the crystal structure as revealed by XRD.

A very interesting result was obtained on the spreading of Mn over the material. One would expect that in a set of materials with a single-phase XRD pattern and equivalent SEM images with clean-shaped crystals of ~200 nm size these materials have a uniform distribution of their constituents. The STEM-EELS results clearly show the opposite. The Mn/Si ratio changes drastically throughout the same crystal. The STEM-EELS images show, for example, the existence of thin Mn-rich layers covering the Si-rich crystals. The thickness of these Mn-rich layers is only in the order of a few nanometers. Actually, the fact that they are only a few nm thin, prevents their detection as a separate phase in XRD. Because these Mn-rich layers seem to either cover crystallites or fill holes in other crystallites, this also implies that, the overall texture of the crystals does not degrade, implying similar SEM images.

An important lesson from this analysis is that if one studies the inclusion of metal ions in zeolites, identical XRD patterns and equivalent SEM images cannot be used to assume that the metal ions have been incorporated in a uniform, or almost uniform, manner. These results on Mn-ZSM-5 show the opposite. This implies that the distribution of metal ions in zeolites can only be determined from an element specific microscopic technique with (sub)nanometer resolution.

Although these materials are not able to form α -oxygen species, the MnS-1^{TPA} sample opens the door to a possible novel catalyst for NO removal.

Acknowledgements

Dr. R. F. Lobo of the Department of Chemical Engineering, University of Delaware is kindly acknowledged for his hospitality during the visit in his department and the valuable input that led to the synthesis of the materials presented in this Chapter. Financial support was provided by the Netherlands Organization for Scientific Research – Chemical Sciences (NWO-CW) and the Netherlands Research School Combination on Catalysis (NRSCC).

References

- [1] M. Taramasso; G. Perego; B. Notari, *U.S. Patent 4410501*, 1983.
- [2] A. K. Uriarte; M. A. Rodkin; M. J. Gross; A. S. Kharitonov; G. I. Panov, Direct hydroxylation of benzene to phenol by nitrous oxide. In *3rd World Congress on Oxidation Catalysis*, 1997; Vol. 110; pp 857.
- [3] M. Iwamoto; H. Furukawa; Y. Mine; F. Uemura; S. Mikuriya; S. Kagawa, *J.Chem. Soc. Chem. Commun.*, **(1986)**, 1272.
- [4] V. A. Tuan; J. L. Falconer; R. D. Noble, *Micropor. Mesopor. Mat.*, 41, **(2000)**, 269.
- [5] M. Masteri-Farahani; F. Farzaneh; M. Ghandi, *J. Mol. Catal. A Chem.*, 192, **(2003)**, 103.
- [6] T. Inui; J. B. Kim; T. Takeguchi, *Zeolites*, 17, **(1996)**, 354.
- [7] C. I. Round; C. D. Williams; C. V. A. Duke, *Chem. Commun.*, **(1997)**, 1849.
- [8] H. Y. Chen; W. M. H. Sachtler, *Catal. Today*, 42, **(1998)**, 73.
- [9] G. I. Panov; A. S. Kharitonov; V. I. Sobolev, *Appl. Catal. A Gen.*, 98, **(1993)**, 1.
- [10] J. Halasz; M. Hodos; I. Hannus; G. Tasi; I. Kiricsi, *Colloids Surf. A: Physicochem. Eng. Aspects*, 265, **(2005)**, 171.
- [11] M. H. Groothaert; J. A. van Bokhoven; A. A. Battiston; B. M. Weckhuysen; R. A. Schoonheydt, *J. Am. Chem. Soc.*, 125, **(2003)**, 7629.
- [12] H. Yahiro; M. Iwamoto, *Appl. Catal. A Gen.*, 222, **(2001)**, 163.
- [13] M. H. Groothaert; K. Lievens; H. Leeman; B. M. Weckhuysen; R. A. Schoonheydt, *J. Catal.*, 220, **(2003)**, 500.
- [14] A. De Lucas; J. L. Valverde; F. Dorado; A. Romero; I. Asencio, *J. Mol. Catal. A Chem.*, 225, **(2005)**, 47.
- [15] M. C. Campa; D. Pietrogiamomi; S. Tuti; G. Ferraris; V. Indovina, *Appl. Catal. B Envir.*, 18, **(1998)**, 151.
- [16] Q. Sun; W. M. H. Sachtler, *Appl. Catal. B Envir.*, 42, **(2003)**, 393.
- [17] Q. H. Zhang; Y. Wang; S. Itsuki; T. Shishido; K. Takehira, *J. Mol. Catal. A Chem.*, 188, **(2002)**, 189.
- [18] J. Garcia-Martinez; D. Cazorla-Amoros; A. Linares-Solano, *Appl. Catal. B Envir.*, 47, **(2004)**, 203.

- [19] J. S. Choi; T. H. Kim; M. B. Saidutta; J. S. Sung; K. I. Kim; R. V. Jasra; S. D. Song; Y. W. Rhee, *J. Ind. Eng. Chem.*, 10, **(2004)**, 445.
- [20] Y. X. Wei; G. W. Wang; Z. M. Liu; P. Xie; Y. L. He; L. Xu, *Catal. Lett.*, 91, **(2003)**, 35.
- [21] P. Kovacheva; N. Davidova, *React. Kinet. Catal. Lett.*, 53, **(1994)**, 277.
- [22] Y. H. Ko; S. J. Kim; M. H. Kim; J. H. Park; J. B. Parise; Y. S. Uh, *Micropor. Mesopor. Mat.*, 30, **(1999)**, 213.
- [23] N. N. Tusar; N. Z. Logar; I. Arcon; F. Thibault-Starzyk; A. Ristic; N. Rajic; V. Kaucic, *Chem. Mater.*, 15, **(2003)**, 4745.
- [24] O. Stephan; A. Gloter; D. Imhoff; M. Kociak; C. Mory; K. Suenaga; M. Tence; C. Colliex, *Surf. Rev. Lett.*, 7, **(2000)**, 475.
- [25] H. van Koningsveld; H. van Bekkum; J. C. Jansen, *Acta Crystallogr.*, B43, **(1987)**, 127.
- [26] D. S. McClure, *J. Phys. Chem.*, 36, **(1962)**, 2757.
- [27] H. Thauern, *Phosphate des ein-und zweiwertigen Indium und Einbau von Chrom(III) und Mangan(III) in Indium(III)-phosphate*. PhD, Rheinischen Friedrich-Wilhelms-Universität Bonn, 2006.
- [28] A. T. Bell; A. W. Aylor; L. J. Lobree; J. A. Reimer, *J. Catal.*, 170, **(1997)**, 390.
- [29] C. Naudin; F. Bonhomme; J. L. Bruneel; L. Ducasse; J. Grondin; J. C. Lassegues; L. Servant, *J. Raman Spectrosc.*, 31, **(2000)**, 979.
- [30] M. G. O'Brien; A. M. Beale; C. R. A. Catlow; B. M. Weckhuysen, *J. Am. Chem. Soc.*, 128, **(2006)**, 11744.
- [31] B. M. Weckhuysen; R. R. Rao; J. A. Martens; R. A. Schoonheydt, *Eur. J. Inorg. Chem.*, **(1999)**, 565.

5

High-resolution Mn K edge X-ray absorption of Mn-ZSM-5 systems

Abstract

We have measured K α -detected X-ray absorption (XAS) spectra of the Mn-ZSM-5 samples that are prepared by both hydrothermal treatment (HTS) and ion exchange. We analyze the pre-edge region and edge region of the Mn K XAS spectrum and conclude that in case of high-resolution XAS spectra, the pre-edge analysis of the valence is the most reliable. Sharp spectral features and the influence of the normalization-procedure negatively affect the edge analysis. The pre-edge analysis learns that the hydrothermally as-synthesized samples and the ion-exchanged samples are all mainly Mn²⁺ ions in an octahedral surrounding. The template free hydrothermally synthesized samples have been modified to an average valence of 2.5 and an average surrounding close to 5. Heating the systems in He to 623 K creates a very large coordination change for the ion exchanged samples, whereas the hydrothermally synthesized samples show little change in coordination. This suggests that the removal of water creates on average one free coordination site for the ion exchanged samples, whereas the HTS samples have little free sites. This result seems to indicate that the α -oxygen sites are to be found on these under-coordinated Mn ions that are found on the ion exchanged samples. In the hydrothermally synthesized samples, such sites are not prepared or they are destroyed during template removal.

5.1. Introduction

Zeolites have proven to be good hosts for active species of transition metals. The aluminum substituted MFI zeolite, ZSM-5, presents an important set of catalysts, in particular in the forms of Fe-ZSM-5 and Cu-ZSM-5. The metal elements can either be introduced during the zeolite synthesis or through post-synthesis treatments. In this paper we study the introduction of Mn into ZSM-5 systems, where both routes, ion exchange on a pre-synthesized H-ZSM-5 system and direct hydrothermal synthesis of Mn-ZSM-5 will be compared with respect to their structural and electronic properties.

In **chapter 3**, it has been described that ion exchanged Mn-ZSM-5 zeolites are active in the decomposition of N_2O . The oxygen atom from the N_2O molecule gives rise to an α -oxygen species, which is identified with UV-vis spectroscopy as having a band at $\sim 18500\text{ cm}^{-1}$, where this band appears during the decomposition of N_2O and disappears during the reaction with NO or methane. In **chapter 4**, it has been described that the hydrothermal synthesis of Mn-ZSM-5 does not yield such dynamic UV-vis band. Instead a static band is visible, indicating that a significant proportion of the manganese is found in an inactive trivalent state.

We use X-ray Absorption Spectroscopy (XAS) to probe quantitatively the valence state and the local symmetry of the Mn atoms. Three spectral regions of the XAS spectrum will be analyzed:

- (1) The pre-edge region
- (2) The edge region
- (3) The EXAFS region

We measure the XAS spectra using the $\text{K}\alpha$ decay channel. The $\text{K}\alpha$ fluorescence is transmitted when the hole in the 1s shell is subsequently filled by a 2p electron. A high-resolution $\text{K}\alpha$ spectrum has been measured using a crystal spectrometer with an energy and width of about 1 eV. The advantage of high-resolution $\text{K}\alpha$ -detected XAS is that it shows spectral features that are sharper than in conventional XAS [1]. This implies that the pre-edge structures are much sharper and better separated from the edge region. Within the edge region, additional structure could be revealed that hinders the more traditional procedures of the edge determination. We will

compare the various methods for edge determination below. Concerning the EXAFS analysis K α -detected XAS yields essentially the same EXAFS spectrum as normal EXAFS.

The pre-edge feature of the Mn K-edge X-ray absorption spectrum is sensitive to the electronic structure and geometry of the manganese site. The pre-edge can be described from transitions into the lowest unoccupied electronic states that mainly have Mn 3d character. These 1s3d quadrupole transitions can be calculated with multiplet calculations [2]. In a centrosymmetric system those transitions are dipole forbidden and are only allowed by weak quadrupole transitions, implying low intensity. A deviation from a centrosymmetric environment enables the mixing of 3d with 4p orbitals, yielding an enhanced intensity of the pre-edge structure. This implies that variations in the pre-edge intensity reflect the changes in the local coordination sphere (geometry) of the manganese ions. As has been described in **chapter 2**, the energy position of the pre-edge is related to the oxidation state of Mn, or more precisely to the occupation of the 3d-band. In case of Mn, the pre-edge shifts approximately 1.5 eV per valence change.

The main Mn K edge is caused by transitions to the lowest empty 4p states and, at higher energies, to other Mn states with p-symmetry. Effectively the edge structure reflects the density of empty states [3]. The energy position of the edge can be related to the valence of Mn. In a theoretical analysis, de Vries et al. [4] show that the shift is caused by the effects of (a) the ionization energy variation with varying 3d-occupation and (b) the counteracting effect of the screening by other electrons upon the 1s ionization. Experimentally a shift of approximately 3.5 eV/valence is found for related manganese oxides, though large variations are found depending on the edge determining method used. Because of these variations, we will determine the Mn K edge with four different methods: (a) the inflection point, (b) the energy where the intensity is 50% of the edge jump, (c) the average of the energies at 20% and 80% of the edge jump and (d) an integration method as outlined below.

The Mn EXAFS spectra have been analyzed with the traditional single scattering EXAFS formula [5]. EXAFS analysis reveals information on the local geometry of the manganese sites, in particular the number of neighbor atoms and the distances to them.

5.2. Experiment

5.2.1. Catalyst preparation

We have prepared Mn-ZSM-5 zeolites with two preparation routes, with (a) with ion exchange and (b) via hydrothermal synthesis.

(a) Ion exchange: Mn-ZSM-5 zeolites have been prepared starting from NH_4 -ZSM-5 (ZEOLISTS, Si/Al ratio of 17.5, surface area of $361 \text{ m}^2/\text{g}$ and pore volume of $0.124 \text{ cm}^3/\text{g}$), with manganese acetate tetrahydrate ($\text{Mn}(\text{ac})_2 \cdot 4\text{H}_2\text{O}$) (99+%, Acros) as a manganese source. Details on the ion exchange procedure have been described in **chapter 3**. Two samples, MnZ-0.24 and MnZ-0.30, have been studied with XAS, as indicated in Table 1.

(b) Hydrothermal synthesis: Mn-S-1 and Mn-ZSM-5 zeolite were synthesized from a gel containing a manganese source, a silica source, a template molecule plus an aluminum source for the ZSM-5 synthesis. In order to optimize the final structure, different sources of silica and manganese, as well as different zeolite templates were used. The X-ray absorption experiments have been performed on the most optimum procedure that uses tetraethyl orthosilicate (TEOS) as Si source, tetrapropyl ammonium hydroxide (TPAOH) (Alfa Aesar, 40% w/w in water) as template and manganese acetate ($\text{Mn}(\text{ac})_2 \cdot 4\text{H}_2\text{O}$), from Acros (> 99%) as Mn source.

Table 1. The Mn-ZSM-5 samples that have been studied with XAS. Mn-S-1 contains no aluminum implying a Mn/Al ratio of infinity.

Sample code	Mn loading (wt %)	Mn/Al ratio
MnZ-0.24	1.2	0.24
MnZ-0.30	1.4	0.29
Mn-S-1 ^{TPA}	2.1	∞
Mn-ZSM-5 ^{TPA}	1.5	1.14

5.2.2. Catalyst in-situ treatments

Treatment of the MnZ-0.24 and MnZ-0.30 samples consists of dehydration of the sample at 623 K for 1 h. After dehydration a succession of gas treatments were applied, starting with a mixture flow formed from

N₂O (30 ml/min, 1% N₂O in He) and He (50 ml/min), for 1 h, followed by NO (50 ml/min, 1% NO in He) and 50 ml/min He at 623 K. These two distinct treatments were repeated three times. The Mn-S-1^{TPA} and Mn-ZSM-5^{TPA} samples were measured in their as-synthesized (as) and template free (tf) forms.

5.2.3. X-ray absorption experiments

XAS experiments were performed at beamline ID-26 of the European Synchrotron Radiation Facility (ESRF) in Grenoble, France. The energy of the incoming synchrotron radiation beam was selected with a Si (111) monochromator. The energy bandwidth of the incident X-ray beam was approximately 1.0 eV at 6500 eV and the (maximum) incident flux was 10¹³ photons/s. The incident energy was calibrated using tabulated values for the K edge features of a MnO standard. A focusing mirror was used in order to reject the higher harmonics. The Mn K α fluorescence emission from the sample was collected using four spherically bent Si (440) crystal analyzers in connection with an APD detector. The samples were pressed into self-supported wafers and placed in an airtight fluorescent cell at a position of 30° with respect to the incoming beam. XAS spectra measured with Mn K α fluorescence are called High-Energy-Resolution Fluorescence Detection (HERFD) XAS, or HERFD-XAS, spectra, to distinguish them from normal XAS spectra [6]. The in-situ cell has a continuous gas flow during the measurements, allowing in-situ XAS experiments.

5.2.4. XAS data treatment

The edge jump of the K α XAS spectra was normalized to 1. Software PeakFit4 (AISN Software, 1995) was used to model the pre-edge region of the spectra. The pre-edge region was fitted using three Pseudo-Voigt functions for all the spectra and also for the reference spectra. The first two functions were used in order to fit the pre-edge shapes of the spectrum, while the third pseudo-Voigt function was necessary for the fitting of the edge jump in combination with a Gaussian cumulative ascending function. The fit of the spectral shape was always with a R² value higher than 0.999. The extracted

pre-edge data were used to determine the centroid energy position and integrated intensity. The extracted pre-edge data were used to determine the characteristics of the pre-edge, that is the centroid energy position and integrated intensity using the peak fitting results of the pre-edge feature. The centroid energy position is defined as the center of the gravity of the components, and is calculated from the average position of the pseudo-Voigt functions weighted by their respective integrated areas.

5.3. Theory

The pre-edge spectral shapes of the Mn^{2+} and Mn^{3+} were calculated with charge transfer multiplet calculations [1]. In octahedral symmetry, the pre-edge shape is given by the $1s3d$ transitions, where an $\text{Mn}^{2+} 3d^5$ ground state is excited to a $1s^1 3d^6$ final state. The shape for the tetrahedral symmetry is given by the contributions of the quadrupole and dipole transitions, where the intensity of the quadrupole transitions is assumed to be half of the intensity of the dipole transitions. This implies that the intensity of a tetrahedral symmetry peak is twice the intensity of an octahedral peak. The quadrupole final state is $1s^1 3d^6$ and the dipole final state $1s^1 3d^5 4p^1$. These states are not allowed to mix, unless the inversion symmetry is broken [7]. The crystal field splitting for Mn^{2+} in octahedral or tetrahedral symmetry is assumed to be respectively +1.2 eV and -0.9 eV. For Mn^{3+} in octahedral and tetrahedral symmetry, a $10Dq$ value of respectively +1.8 and -1.2 eV has been used. Due to the relative broad spectra, small variations in these values will not significantly modify the spectral shapes.

5.4. Results

5.4.1. X-ray absorption spectra

The Mn K edge XAS spectra of $\text{Mn-S-1}^{\text{TPA}}$ and $\text{Mn-ZSM-5}^{\text{TPA}}$ have been measured in He at room temperature. Figure 1 shows the HERFD-XAS spectra of *as-synthesized* (as) and template-free (tf) $\text{Mn-S-1}^{\text{TPA}}$ and $\text{Mn-ZSM-5}^{\text{TPA}}$ in comparison with the spectra of the reference compounds MnO (Mn^{2+}) and Mn_2O_3 (Mn^{3+}). One observes that both *as-synthesized* samples have an

edge between MnO and Mn_2O_3 , while the template free samples have an edge jump close to that of Mn_2O_3 . The Mn K edge XAS spectra of $\text{Mn-S-1}^{\text{TPA}}$ and $\text{Mn-ZSM-5}^{\text{TPA}}$ have also been measured after heating the template free sample to 623 K (under He), a treatment in N_2O at 623 K and a subsequent treatment in NO at 623 K. These pre-edges and edges of these spectra are analyzed below.

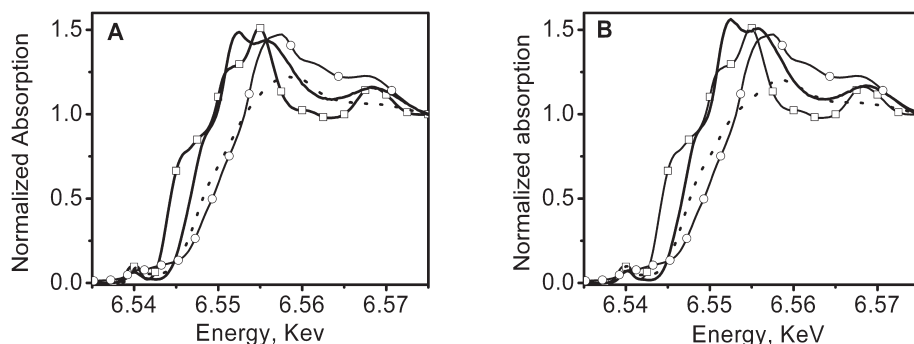


Figure 1. HERFD-XAS spectra of as synthesized (full line) and template free (dotted line) of $\text{Mn-S-1}^{\text{TPA}}$ (A) and $\text{Mn-ZSM-5}^{\text{TPA}}$ (B) samples compared with MnO (\square) and Mn_2O_3 (\circ) reference compounds.

The Mn K edge XAS spectra of MnZ-0.30 and MnZ-0.24 have been measured at room temperature under He, after heating to 623 K (under He) and after each of the three N_2O and NO treatments. Figure 2 shows the XAS spectra, measured with $\text{K}\alpha$ HERFD technique. Heating to 623 K (a to b) decreases the white line. Also the edge shifts slightly and the pre-edge becomes smaller. The first N_2O treatment gives an edge shift of 1.83 eV, hence a slight oxidation, while the first NO treatment shows an inverse behavior and a slight reduction. In order to have a better understanding of the changes that occur during reaction time in-situ HERFD-XAS measurements were performed at an interval of 5 min. This will give us the chance for a more detailed analysis of the two interesting regions (the edge region and the pre-edge region) as a function of reaction time. A full analysis of these regions will be presented below.

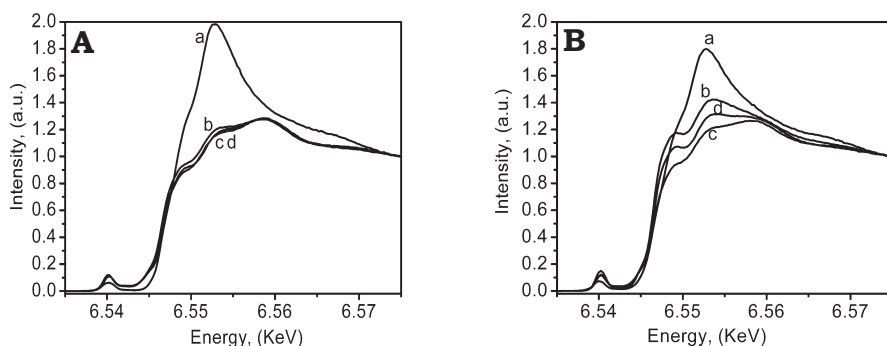


Figure 2. XAS spectra at RT (a), 623 K (b) and after 1 h of N₂O (c) and NO treatment (d) of MnZ-0.24 (A) and MnZ-0.30 (B).

Figure 3 presents the HERFD-XAS features of MnZ-0.30 at the starting point of the N₂O treatment (b) and the XAS spectrum at the end of the treatment (c). For a better observation of the changes that occurs in time, the initial spectrum of the treatment (a) was chosen as a reference that was subtracted from all the spectra. During the N₂O treatment, it is observed that the white line decreases in time. The insert of the figure follows the changes in the pre-edge region, where we can observe a decrease of the main feature of this region, while a new feature is observed to be formed and to increase in time. In the case of NO treatment, an opposite effect was observed with increasing white line intensity (Figure 4).

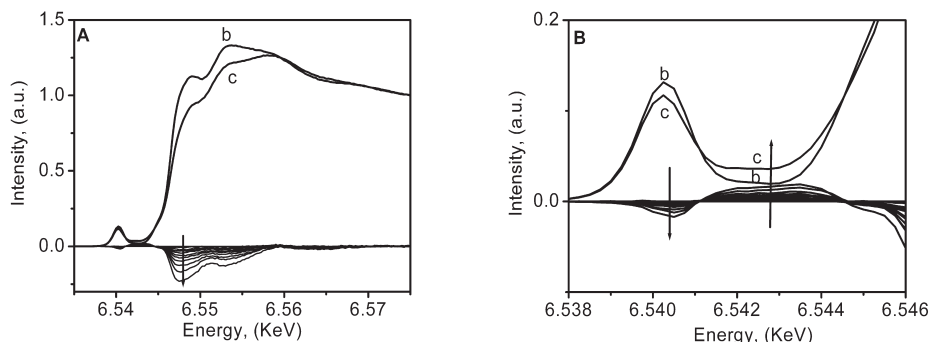


Figure 3. (A) XAS spectra of MnZ-0.30 at the beginning (b) and the end (c) of 1 h of N_2O treatment. Difference spectra following the in-situ evolution of XAS spectra. (B) Magnified view of the pre-edge region.

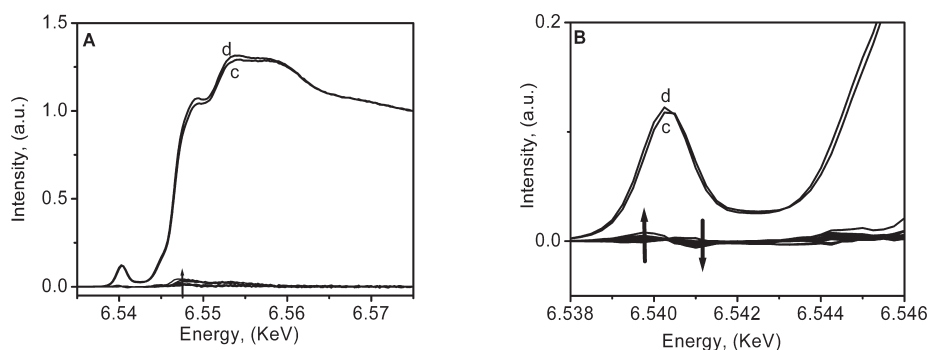


Figure 4. (A) HERFD-XAS spectra of MnZ-0.30 at the beginning (c) and the end (d) of 1 h of NO treatment. Difference spectra following the in-situ evolution of XAS spectra. (B) Magnified view of the pre-edge region.

We will further analyze the various portions of these HERFD-XAS spectra below, respectively the pre-edge region, the edge region and the EXAFS region.

5.4.2. Pre-edge analysis

In a detailed and extensive XAS study on Mn-bearing minerals, Farges et al. [8] presented a correlation of the changes of the Mn K pre-edge with the oxidation state and local symmetry. The pre-edge features of Mn in some thirty oxide materials were studied using this method. In order to make a quantitative determination of changes in the coordination of Mn based on variation of the pre-edge features high-resolution spectra are required for a well resolved pre-edge structure and also a precise isolation of the pre-edge from the main edge. Using conventional XAS measurements inaccuracy is introduced due to the poor separation of the pre-edge region from the main edge, making a reliable and systematic background subtraction difficult. With the superior spectral resolution of HERFD-XAS a clear separation of these two regions is found, minimizing the inaccuracy. As an example, a comparison of the results (centroid position) obtained from the pre-edge analysis of two reference spectra (MnO and Mn₂O₃) measured using conventional, RIXS and HERFD-XAS techniques is shown in Table 2.

Table 2. Comparison between the centroid positions of two reference compounds calculated based on different measuring XAS techniques. *This value has been determined as 2.0 eV by Glatzel et al. [9].

Method	Reference	MnO	Mn ₂ O ₃	ΔE
XAS	Farges et al. [8]	6540.62	6540.91	0.3
HERFD-XAS	This work	6539.9	6541.6	1.7*

In the case of Mn²⁺ the pre-edge feature has a distinct shape corresponding to the real spectrum and is situated at a low energy, which can be separated from the main edge. As we will show bellow, the Mn³⁺ pre-edge feature consists of two strong features split by ~3 eV, due to the large 3d3d multiplet interactions within the 1s¹3d⁵ final state. In this case, the second feature is situated at a higher energy, and with normal XAS this feature will not be visible and be included in the main edge. This explains the small shift between the two consecutive oxidation states compared with normal XAS to the high-resolution techniques.

The pre-edge spectrum of Mn^{2+} spectrum can be calculated from the transition from $3d^5$ to $1s^1 3d^6$ and the Mn^{3+} spectrum is calculated from $3d^4 \rightarrow 1s^1 3d^5$. Figure 5 shows the results obtained from multiplet calculations, which corresponds well to reference compounds [2]. The calculated stick spectra are convoluted with a 1.1 eV Lorentzian and 1.2 eV Gaussian line shape to simulate respectively the life time broadening and the overall experimental resolution [9]. The broadened Mn^{2+} pre-edge has a single peak (with this resolution; but there are actually two sticks split by the crystal field of 1.2 eV). The Mn^{3+} $1s 3d^5$ spectrum shows two features that are split by 3.0 eV. The first feature is close to the Mn^{2+} peak and the second feature appears at 6542 eV.

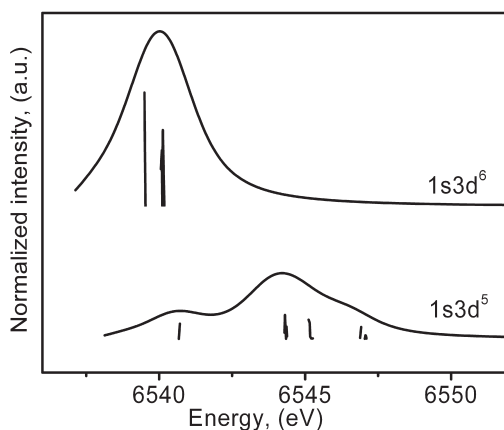


Figure 5. TT Multiplet calculations of Mn^{2+} (top) and Mn^{3+} (bottom) compounds.

Figure 6 shows the addition of the Mn^{2+} and Mn^{3+} calculated spectrum in comparison with an experimental spectrum. The Mn^{2+} is clearly visible as the pre-edge peak and presence of Mn^{3+} can be related to the shoulder at 6542 eV.

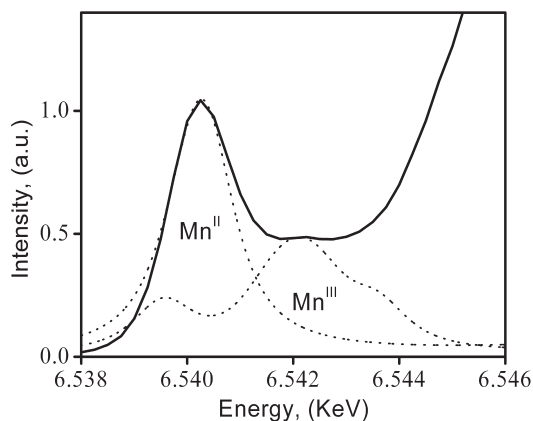


Figure 6. Charge transfer multiplet calculations for 1s to 3d quadrupole transitions of Mn^{2+} and Mn^{3+} compared to an experimental XAS spectrum of Mn-ZSM-5.

Figure 7 shows an enlargement of the pre-edge regions of the XAS spectra as given in Figure 2. At room temperature, the sample is characterized by the presence of divalent manganese in a 6-fold coordination symmetry (spectrum a). At 623 K, the increase of the intensity in the pre-edge region shows that manganese is changing its symmetry, going from a 6-fold coordination to a 4-fold coordination [10,11] (spectrum b). This change from 6-fold to 4-fold symmetry is due to the elimination of the coordinated water. The N_2O or NO treatments keeps the main pre-edge feature unchanged, while the second feature at 6543 eV has an oscillating behavior function of the gas treatments (spectrum c). In order to identify the nature of the features present in the pre-edge region multiplet calculations were performed for different oxidation states of manganese, i.e. a divalent and trivalent oxidation state.

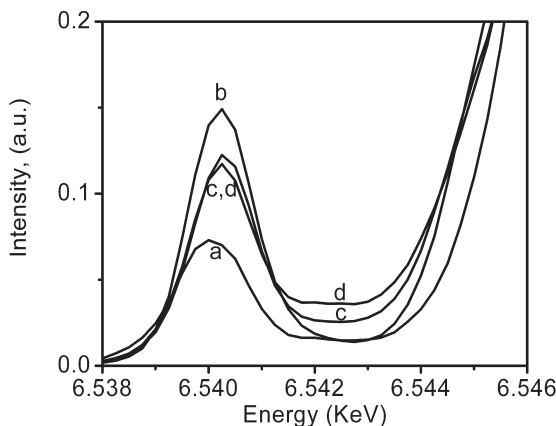


Figure 7. HERFD-XAS of MnZ-0.30 spectra at RT (a), 623 K (b) and after 1 h of N₂O (d) and NO treatment (c).

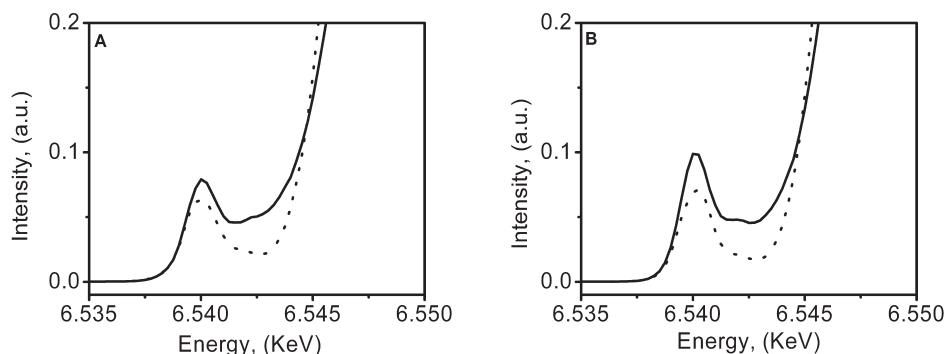


Figure 8. Pre-edge peak of the prepared Mn-S-1^{TPA} (A) and Mn-ZSM-5^{TPA} (B) sample as synthesized (dotted) and after template removal (solid).

Figure 8 shows the HERFD-XAS pre-edges of Mn-S-1^{TPA} (A) and Mn-ZSM-5^{TPA} (B). It turns out that template removal increases the pre-edge intensity in both cases. As discussed above, this implies a change in the coordination number, namely a transition from octahedral to distorted octahedral. The centroid position energy is shifted to higher energies, corresponding to an oxidation to Mn³⁺.

Table 3 presents the centroid positions and total integrated area obtained from the pre-edge analysis of the Mn-S-1^{TPA} and Mn-ZSM-5^{TPA} samples, plus the first series of measurements (RT, 623 K, N₂O, NO) on

the MnZ-0.30 sample. The MnZ-0.30 and MnZ-0.24 samples have been measured through three N₂O-NO cycles and the Mn-S-1^{TPA} and Mn-ZSM-5^{TPA} have been measured, as-synthesized, template free, 623 K, plus one cycle of N₂O and NO. The full set of data is summarized in Figure 9. The center of gravity of Mn²⁺ has been set to the value of MnO (6539.9 eV) and Mn³⁺ to the value of Mn₂O₃ (6541.6 eV). The integrated intensity has been set to 0.13 for 6-fold (octahedral) and 0.37 for 4-fold (tetrahedral) symmetry. In particular the intensities should be taken with some reserve and should only be used as a rough guide.

Table 3. Comparison between the centroid positions and the total integrated areas of the prepared Mn-S-1^{TPA}, Mn-ZSM-5^{TPA} and Mn0.30 samples. The full set of data is given in Figure 9.

Sample	Centroid (eV)	Total integrated area	Valence
Mn-S-1 ^{TPA} am	6540.1	0.137	2.13
Mn-S-1 ^{TPA} tf	6541.2	0.231	2.76
Mn-ZSM-5 ^{TPA} am	6540.3	0.155	2.24
Mn-ZSM-5 ^{TPA} tf	6540.7	0.205	2.47
Mn0.30 RT	6540.1	0.131	2.13
623 K	6540.8	0.268	2.58
N2O	6541.2	0.267	2.76
NO	6541.2	0.265	2.76

Figure 9 shows that the ion exchanged samples start essentially as 6-fold Mn²⁺ at room temperature. They change to 5-fold Mn^{2.5+} at 623 K and then slightly oxidize further during the N₂O treatments, partly compensated by the NO cycles. The hydrothermal synthesized samples also start as 6-fold Mn²⁺ in their as synthesized form, but after template removal their average valence is already Mn^{2.5+} to Mn^{2.7+} with also a less than 6-fold surrounding. This implies that already at room temperature these samples are largely oxidized and less than 6-fold surrounded. During the heating, from room temperature to 623 K, the Mn-ZSM-5 valence is constant and the coordination goes slightly down, while for Mn-S1 the coordination is constant and the valence fluctuates slightly. The large change in coordination of the

ion exchanged samples indicates the loss of water bound to the Mn sites. In case of the hydrothermal synthesized samples, there is less water and also the coordination numbers remain higher.

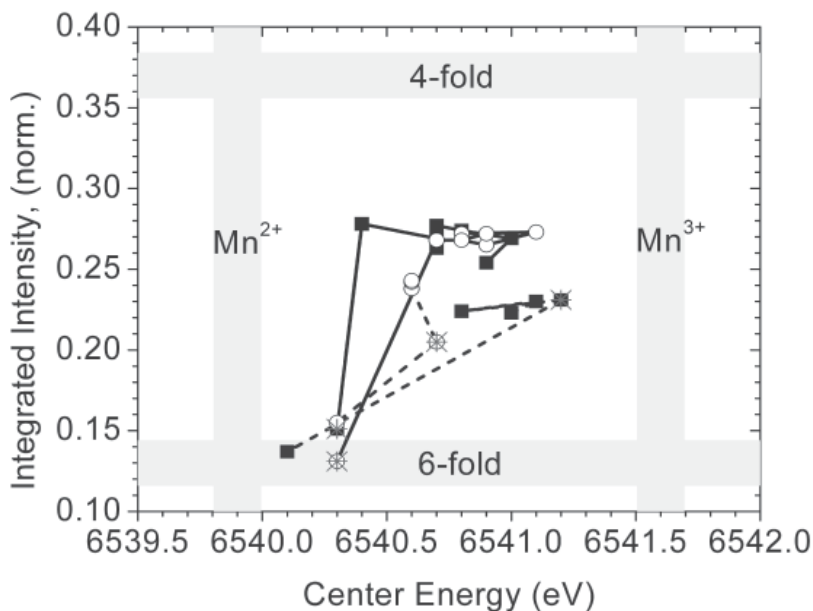


Figure 9. The integrated intensities and the center of gravity of the pre-edge of the 4 series of samples, Mn-S-1^{TPA} (dashed, closed squares), Mn-ZSM-5^{TPA} (dashed, open circles), MnZ-0.30 (line, open circles) and MnZ-0.24 (line, closed squares). The samples that are measured at room temperature before heating to 623 K are indicated with an asterisk (*).

5.4.3. XAS edge analysis

The traditional procedure to determine the valence from an XAS spectrum is to analyze the edge position. There are a range of procedures to determine the edge position, depending also on the goal of the analysis, where here we opt for the analysis of a particular set of materials (Mn-

ZSM-5 systems) with the help of closely related reference compounds (Mn oxides). Because we use K α -detected XAS this has the advantage of a better resolution, yielding more precise numbers.

In order to determine the valence state of Mn in the samples, the energy at the edge has been determined. However, there are, at least, four different methods to define the energy of the edge:

- a. The inflection point;
- b. The energy where the intensity is 50% of the edge maximum;
- c. The average of the energies at 20% and 80% of the edge maximum; and
- d. The Equivalent Integrated Area (EIA) method [12].

The inflection point is well defined and can be determined from the maximum of the first derivative. In case of a single, non-structured edge, all methods (a) to (d) will find the same energy. The situation becomes more complicated with a spectrum for which a shoulder is visible on the leading edge. The inflection point might lose its value in such a case and, in fact, there can be two or more inflection points. The EIA method to determine the edge energy is the most accurate, but at the same time the least known method. The EIA method involves the following procedure: (1) the spectrum is normalized to the edge jump; (2) also a reference spectrum, for example MnO, is normalized; (3) the energy at which the reference spectrum crosses 1.0 is determined and the spectrum is integrated from a value below the edge to this energy. This yields a reference integrated intensity (RII); (4) one sets the RII value to a certain percentage of this value, where we use 80% of RII; (5) The edge of a spectra is determined by integrating it from below the edge to an integrated value of $0.8 \cdot \text{RII}$. To increase the accuracy of the method, the experimental spectra have been interpolated with an energy step of 0.01 eV. It is noted that effectively the pre-edge intensity is also part of this integration method. Because this EIA method uses integration, the obtained results can be expected to be very accurate. All these four methods were applied in order to determine the edge energy and the results are shown in Table 4.

Table 4. Energy values at edge position calculated using different methods.

Sample	Energy value at the edge determined using different method (eV)			
	(a) inflection	(b) 50%	(c) 20%-80%	(d) 0.8*RII
MnO	6550.3	6540.7	6545.0	6547.8
Mn ₂ O ₃	6553.8	6549.7	6549.6	6552.4
Mn-S-1 ^{TPA} (as)	6550.7	6546.6	6546.6	6550.0
Mn-S-1 ^{TPA} (tf)	6547.5	6548.1	6548.5	6551.4
Mn-ZSM-5 ^{TPA} (as)	6550.9	6546.6	6546.6	6550.0
Mn-ZSM-5 ^{TPA} (tf)	6546.9	6547.6	6548.0	6550.1

Table 4 shows that the edge positions obtained from the four methods are different, but they keep an average shift of about 3.5 to 4 eV [13] between the consecutive oxidation states, except the 50% method that has a 9 eV shift. In our case, the most reliable values are obtained using the methods (c) and (d), the inflection point method being unreliable due to the visible structure present in the leading edge.

Knowing these energy values, and using a linear interpolation between Mn²⁺ and Mn³⁺ we estimate the percentage of divalent and trivalent manganese present in the samples during different preparation steps. From the values obtained using methods (c)/(d) in Table 5 one can conclude the as-synthesized samples have an average valence of 2.3/2.5. Calcination brings the samples closer to a trivalent situation, respectively to 2.8 for the Mn-ZSM-5^{TPA} sample. Another important conclusion from this table is that the methods to determine the valence from the XAS edge structure show significant variation. We conclude that the EIA method and the 20-80 method reach consistent results. The inflection point and 50% methods are too dependent on spectral details to yield reliable results. It is noted that for reliability of the absolute numbers for the valence, the normalization to the edge jump is the most critical parameter.

Table 5. Valence determined from the energy value at edge determined using different method, calibrated to MnO.

Sample	Valence determined from the energy value at edge determined using different method			
	(a) inflection	(b) 50%	(c) 20%-80%	(d) EIA method
MnO	2	2	2	2
Mn ₂ O ₃	3	3	3	3
Mn-S-1 ^{TPA} (as)	2.1	2.7	2.3	2.5
Mn-S-1 ^{TPA} (tf)	<2	2.8	2.8	2.8
Mn-ZSM-5 ^{TPA} (as)	2.2	2.7	2.3	2.5
Mn-ZSM-5 ^{TPA} (tf)	<2	2.8	2.7	2.5

5.4.4. EXAFS analysis

We have measured the EXAFS spectra of the Mn-S-1^{TPA} (as, tf) and Mn-ZSM-5^{TPA} (as, tf). The quality of the EXAFS spectra was only sufficient for a partial analysis and essentially we only could determine the nearest neighbor distances with sufficient reliability. In Table 6 we present a list of manganese compounds with the corresponding Mn-O length bonds and the corresponding coordination symmetry.

Table 6. A list of various manganese compounds in bivalent and trivalent state and in various coordination environments and the corresponding Mn-O bond length.

Compound	Manganese oxidation state	Coordination symmetry	Mn-O length bond	Reference
MnO	2 ⁺	O _h	2.22	[9]
Mn ₂ O ₃	3 ⁺	O _h	2.02	[9]
MnCr ₂ O ₄	2 ⁺	T _d	2.03	[9]
Mn-ALPO18	3 ⁺	T _d	1.86	[14]
Mn-AlPO	3 ⁺	T _d [*]	1.86	[15]
Mn-S-1	3 ⁺	T _d	1.93	[16]
Mn-S-1 ^{TPA} (as) at 298 K	2 ⁺	O _h	2.22	This work
Mn-S-1 ^{TPA} (tf) at 623 K	3 ⁺	T _d	1.86	This work
Mn-ZSM-5 ^{TPA} (as) at 298 K	2 ⁺	O _h	2.24	This work
Mn-ZSM-5 ^{TPA} (tf) at 623 K	2 ⁺ / 3 ⁺	T _d	1.93	This work

O_h=Octahedral; T_d= Tetrahedral.

From Table 6 we can conclude that for *as-synthesized* materials (Mn-S-1^{TPA} and Mn-ZSM-5^{TPA}) the predominant manganese site is the Mn²⁺ in octahedral coordination. In this context we note that the EXAFS method offers less detailed information on the valence because the analysis yields distances and the translation from distance to valence is not uniquely defined. In general a shorter distance implies a higher valence but this rule is only valid if the distances are mainly determined by the metal ion (as in bulk oxides). In more complex systems, such as metal ions/clusters in zeolites, a less direct relation between valence and distance could exist. Therefore the valences given should only be interpreted as an initial suggestion for the (dominant) valence.

Removal of the template produces different changes for the Mn-ZSM-5^{TPA} and Mn-S-1^{TPA} materials. In the case of Mn-S-1^{TPA} this process produces a shortening from 2.22 to 1.86 Å, suggesting the oxidation of Mn²⁺ to Mn³⁺ in

combination with the change in the coordination symmetry from octahedral to tetrahedral. This observation is consistent with the Mn-O bond length of 1.86 Å observed by Beale et al. in Mn-AlPO-18 [14] and with calculations of a tetrahedral site containing Mn^{3+} [15]. The Mn-O bond determined for Mn-ZSM-5^{TPA} is 1.93 Å, which corresponds with the Mn-O distance in Mn-S-1 by Tusar et al. [16]. This bond is longer than that observed for Mn-S-1^{TPA} and shorter than Mn^{3+} octahedral compounds. A possible explanation for this length is a combination between Mn^{3+} in tetrahedral coordination and possible some Mn^{2+} in tetrahedral coordination.

5.5. Discussion

Table 7 presents a comparison of the valence numbers from the pre-edge and edge analysis. We can observe that we obtained similar data from the pre-edge and edge analysis for the Mn-S-1 and Mn-ZSM-5 samples.

Table 7. Overview of the valence determined from the edge and the pre-edge.

Sample	Valence	
	Pre-edge	Edge (method c)
Mn-S-1 ^{TPA} am	2.13	2.3
Mn-S-1 ^{TPA} tf	2.76	2.8
Mn-ZSM-5 ^{TPA} am	2.24	2.3
Mn-ZSM-5 ^{TPA} tf	2.47	2.7

A source for systematic errors in case of edge determination of the valence is the errors introduced by the normalization of the references used as well as the samples themselves. To determine a valence of a system, in total three spectra must be calibrated and normalized, where the normalization error (in first approximation) is transferred linearly to the valence determination. This applies to the methods b to d. The derivative method (a) is not dependent on normalization. However, as discussed above,

the derivative method as well as the 50% method is very sensitive to the detailed spectral structure.

Because of the normalization problem, there will always remain a certain systematic error uncertainty, in particular when the references (bulk oxides) are different in nature from the studied systems (zeolites). The pre-edge does not suffer from a normalization error; there the major cause for systematic errors is the separation between pre-edge and edge. In case of $K\alpha$ -detected XAS, this separation is straightforward and leaves room for only very small errors. Therefore, we suggest that in case of HERFD detected XAS spectra, the pre-edge analysis of the valence is the most reliable.

5.6. Concluding remarks

The pre-edge analysis learns that the four samples Mn-S-1^{TPA} (as), Mn-ZSM-5^{TPA} (as), MnZ-0.30 (RT) and MnZ-0.24 (RT) are mainly Mn²⁺ ions in an octahedral surrounding. The Mn-S-1^{TPA} (tf) and Mn-ZSM-5^{TPA} (tf) systems have been modified to an average valence of 2.5 and an average surrounding close to 5. This implies that the starting materials from hydrothermal synthesis (HTS) (Mn-S-1^{TPA} (tf) and Mn-ZSM-5^{TPA} (tf)) have quite different characteristics than the starting materials from ion exchange (MnZ-0.30 (RT) and MnZ-0.24 (RT)).

Heating the systems in He to 623 K creates a very large coordination change for the ion exchanged samples combined with a small oxidation change. In contrast, Mn-S-1^{TPA} (tf) shows no change in coordination and Mn-ZSM-5^{TPA} (tf) shows only a minor change. This suggests that the removal of water creates on average one ‘free’ coordination site for the ion exchanged samples, whereas the HTS samples have little to none new free sites due to water removal. These samples have already a close to 5-fold surroundings at room temperature, but this suggests that these sites are not available for coordination.

This result seems to indicate that the α -oxygen sites are to be found on these under-coordinated Mn ions that are found on the ion exchanged samples. The potential sites on the HTS samples seem to be destroyed (as potential α -oxygen sites) during the removal of the template, or alternatively

these sites are not created at all in the HTS procedure that was used. A large change in coordination between room temperature and 623 K can be seen as an indication that there are many undercoordinated Mn sites available.

Acknowledgements

The HERFD-XAS experiments were performed in collaboration with Dr. P. Glatzel (ESRF, Grenoble, France). Financial support was provided by the Netherlands Organization for Scientific Research – Chemical Sciences (NWO-CW) and the Netherlands Research School Combination on Catalysis (NRSCC).

References

- [1] F. M. F. de Groot, *Chem. Rev.*, 101, **(2001)**, 1779.
- [2] F. M. F. De Groot, *American Institute of Physics Conference (AIP)*, 882, **(2007)**, 35.
- [3] A. L. Ankudinov; B. Ravel; J. J. Rehr; S. D. Conradson, *Phys. Rev. B*, 58, **(1998)**, 7565.
- [4] A. H. de Vries; L. Hozoi; R. Broer, *Int. J. Quantum Chem.*, **(2003)**, 57.
- [5] J.A. van Bokhoven; T. Ressler; F.M.F. de Groot; A. Knop-Gericke *In-situ spectroscopy of catalysis*, Ed. B.M. Weckhuysen; American Scientific Publishers, 2004.
- [6] P. Glatzel; U. Bergmann, *Coord. Chem. Rev.*, 249, **(2005)**, 65.
- [7] T. E. Westre; P. Kennepohl; J. G. DeWitt; B. Hedman; K. O. Hodgson; E. I. Solomon, *J. Am. Chem. Soc.*, 119, **(1997)**, 6297.
- [8] F. Farges, *Phys. Rev. B*, 71, **(2005)**, 155109.
- [9] P. Glatzel; U. Bergmann; J. Yano; H. Visser; J. H. Robblee; W. Gu; F. M. F. d. Groot; G. Christou; V. L.Pecoraro; S. P.Cramer; V. K.Yavhandra, *J. Am. Chem. Soc.*, 126, **(2004)**, 9946.
- [10] M. Wilke; F. Farges; P. E. Petit; G. E. Brown; F. Martin, *Am. Mineral.*, 86, **(2001)**, 714.
- [11] W. M. Heijboer; P. Glatzel; K. R. Sawant; R. F. Lobo; U. Bergmann; R. A. Barrea; D. C. Koningsberger; B. M. Weckhuysen; F. M. F. de Groot, *J. Phys. Chem. B*, 108, **(2004)**, 10002.
- [12] T. W. Capehart; J. F. Herbst; R. K. Mishra; F. E. Pinkerton, *Phys. Rev.*

B, 52, **(1995)**, 7907.

[13] T. Ressler; S. L. Brock; J. Wong; S. L. Suib, *J. Synchrotron Radiat.*, 6, **(1999)**, 728.

[14] D. A. Fletcher; R. F. McMeeking; D. Parkin, *J. Chem. Inf. Comput. Sci.*, 36, **(1996)**, 746.

[15] A. M. Beale; G. Sankar; C. R. A. Catlow; P. A. Anderson; T. L. Green, *Phys. Chem. Chem. Phys.*, 7, **(2005)**, 1856.

[16] N. N. Tusar; N. Z. Logar; I. Arcon; F. Thibault-Starzyk; A. Ristic; N. Rajic; V. Kaucic, *Chem. Mat.*, 15, **(2003)**, 4745.

Summary, Conclusions and Future Perspectives

The main goals of this PhD-thesis were:

- (1) the synthesis of a Mn-ZSM-5 material capable to generate α -oxygen species and to use it in a catalytic reaction. Mn-ZSM-5 materials have been prepared by two routes: (a) the post synthesis method and (b) hydrothermal synthesis.
- (2) to determine the Mn active site using advanced characterization tools. This includes the electronic structure and geometric structure under in-situ conditions. A number of spectroscopic techniques were used, and by interpretation of the resulting data we can compose a detailed picture of the phenomena that occur during catalytic reactions.

In what follows, we will summarize the main findings, make some conclusions and present some prospects for future research.

A. Summary

Chapter 2 presents an introduction of the characterization techniques, which are important to obtain detailed information about the catalyst materials under study. A fundamental basis is provided as a background for the experimental chapters in which these techniques have been used. The characterization methods selected to study the catalyst materials discussed in this PhD - thesis offers a wide range of information. These includes bulk crystallographic information from X-Ray Diffraction (XRD), the elemental composition from X-Ray Fluorescence (XRF), the surface texture from Scanning Electron Microscopy (SEM) and the oxidation state from X-ray Absorption Spectroscopy (XAS) and diffuse reflectance UV-Vis (UV-Vis) spectroscopy. Two novel tools have been discussed in more detail. High-Energy-Resolution Fluorescence Detection - X-ray Absorption Spectroscopy (HERFD-XAS) provides a higher-resolution version of XAS spectra, which can be used to derive more detailed information on the oxidation state and site geometry from the pre-edge and edge structure. Scanning transmission electron microscopy - Electron energy-loss spectroscopy (STEM-EELS) yields elemental and oxidation state information with a spatial resolution of 0.5 nm.

Chapter 3 is presented as a complete research report on Mn-ZSM-5 materials obtained using the post synthesis method. The first part of this chapter discusses the preparation of these Mn-ZSM-5 materials using the *ion exchange* procedure. A detailed description of the preparation procedure together with its activation treatment is presented.

A second section investigates the catalytic activity of the ion exchanged Mn-ZSM-5 materials in two reactions, (a) the catalytic N_2O decomposition and (b) the NO oxidation reaction. These catalytic tests reveal that these materials are capable to decompose N_2O with the formation of N_2 and a α -oxygen species. A linear relation was observed between the Mn loading and the observed catalytic activity, for Mn loadings between 0.64 and 1.3 wt %. The reactivity of the generated α -oxygen species was studied using the NO oxidation as a test reaction. The NO oxidation demonstrates the possibility to use this special oxygen species in chemical reactions. UV-Vis measurements revealed that generation of α -oxygen species increases the

oxidation state of Mn^{2+} to Mn^{3+} , while the removal of the generated α -oxygen species reduces the oxidation state of Mn^{3+} to a Mn^{2+} . These changes in the coordination sphere and the oxidation states gives rise to an absorption band centered at 18500 cm^{-1} during the N_2O exposure. During NO oxidation the disappearance of the UV-Vis band is observed, a clear indication that the α -oxygen species is removed from the catalyst surface. From further experiments we can state that this band is characteristic to the generation of α -oxygen species.

The final part discusses the characterization of these materials under in-situ conditions and presents a proposal for the active centre. The results show that, upon generation of α -oxygen species under N_2O exposure, the coordination environment and oxidation state of manganese is changing.

Chapter 4 deals with the preparation of Mn-MFI materials (as Mn-ZSM-5 and Mn-S-1) using the hydrothermal synthesis method. The preparation procedure has been optimized starting from a published preparation method. In an attempt to reproduce this preparation procedure with TEOH we obtained a low quality sample with a poor crystallinity and reproducibility. By changing the structure directing agent from TEOH to TPAOH we were able to obtain crystalline materials.

Using a combination of XRD and Rietveld refinement we were able to prove that our materials possess the MFI structure. STEM-EELS revealed that the Mn-ZSM-5 crystals are covered with alternating manganese-rich and silicon-rich domains, indicating a non-equal distribution of manganese over the crystal. Regarding the catalytic activities we show that Mn-S-1 possesses a high activity for N_2O decomposition, but without the generation of α -oxygen species. As a confirmation for the absence of α -oxygen species NO oxidation reaction did not take place and instead a disproportionation reaction of NO to N_2O and NO_2 was observed. The high selectivity towards N_2O (75%) can suggest that this material can be used as a novel NO catalyst removal, where N_2O can be transformed to N_2 and O_2 by another type of catalyst, while NO_2 can be purified and used further on for the preparation of fertilizers.

Chapter 5 presents a complete analysis for high-resolution Mn K edge X-ray absorption spectra of the Mn-ZSM-5 samples that are prepared by both hydrothermal treatment (HTS) (**Chapter 4**) and ion exchange (**Chapter 3**). The pre-edge analysis learns that both types of samples are mainly Mn^{2+}

ions in an octahedral surrounding at room temperature. By removing the template, the hydrothermal synthesized samples have been modified to an average valence of 2.5 and an average surrounding close to 5. This implies that the starting materials from hydrothermal synthesis have quite different characteristics than the starting materials from ion exchange. Heating the systems in helium to 623K creates a very large coordination change for the ion exchanged samples combined with a small oxidation. In contrast, the HTS shows no change/or minor changes in coordination. This suggests that the removal of water creates on average one 'free' coordination site for the ion exchanged samples, whereas the HTS samples have little to none new free sites due to water removal. These samples have already a close to 5-fold surroundings at room temperature, but this suggests that these sites are not available for coordination. This result seems to indicate that the α -oxygen sites are to be found on these under-coordinated Mn ions that are found on the ion exchanged samples. The potential sites on the HTS samples seem to be destroyed (as potential α -oxygen sites) during the removal of the template, or alternatively these sites are not created at all in the HTS procedure that was used. A large change in coordination between room temperature and 623K can be seen as a signal that there are many under coordinated Mn sites available.

B. Conclusions

We are now able to answer two questions regarding the generation of α -oxygen species in Mn-ZSM-5 zeolites:

- 1) What are the requirements that a zeolite material needs to possess in order to generate α -oxygen species?
- 2) What characterization techniques can be used in order to reveal the properties of the active centre for N_2O decomposition and the related formation of α -oxygen species?

In order to address the first question, two types of materials were prepared presenting different properties from the geometric and electronic structure point of view. The ion-exchanged Mn-ZSM-5 materials presented in **Chapter 3** are characterized by a dynamic geometric and electronic structure, as is evident from the changes in the coordination sphere and

oxidation state of the manganese during the catalytic reactions. An opposite conclusion can be drawn for the Mn-ZSM-5 materials presented in **Chapter 4**. Due to the presence of large manganese-rich domains which incorporate the majority of the present manganese, the overall systems present a static geometric and electronic behavior. An overview of the main characteristics of the two types of samples is presented in Table 1.

Table 1. Characteristics of synthesized Mn-ZSM5 samples obtained from different characterisation techniques.

Techniques	Sample	MnZ-0.30 ion exchanged	Mn-ZSM5 ^{TPA} hydrothermal synthesis
XRD		MFI structure	MFI structure
XRF		Mn wt%=1.4 Mn/Al=0.3 (Si/Al)=17.5	Mn wt%=1.5 Mn/Al=1.1 (Si/Al)=64
XAS	RT	Mn ²⁺ ; Oh; 6-fold	Mn ^{2.5+} ; Td; 4-fold
	643 K	Mn ²⁺ ;Td; 4-fold	Mn ^{2.5+} ; Td; 4-fold
	N ₂ O	Mn ²⁺ /3 ⁺ ; 5-fold	Mn ^{2.5+} ; Td; 4-fold
	NO	Mn ²⁺ /3 ⁺ ; 5-fold	Mn ^{2.5+} ; Td; 4-fold
STEM-EELS		~ 2-3 nm layer MnO enrichment on some external surfaces	Alternate Mn-rich with Si-rich domains indicating Mn-oxide particles
UV-Vis		UV-Vis band at 18500 cm ⁻¹	UV-Vis band at 20200 cm ⁻¹
Catalysis	N ₂ O	α -oxygen generation during N ₂ O decomposition	N ₂ O decomposition
	NO	Oxidation to NO ₂	Disproportionation to N ₂ O and NO ₂

We can conclude that the generation of α -oxygen species is made possible by fulfilling a number of factors related to the Mn - cluster:

- Dynamic divalent and trivalent oxidation states with the possibility to easily exchange between them.
- The possibility to contain different coordination environments and the possibility to exchange between them.

- c. The dispersion of the active phase should be high in order to hinder the formation of particles which can influence in a negative way the possibility to change the coordination state of the active centre.

Concerning characterization techniques, the challenge to identify the active species lies in the diversity of the species present in the catalyst materials, so discrimination between spectator and active species is necessary. In order to do that we need to identify the characterization techniques capable of determining the characteristics presented as an answer to the first question.

It is well-known that the K edge XAS spectra of the 3d transition are used to determine the nature of neighbors, their number and their distances. The energy position of the K edge varies with the valence, at least if the structure and the nature of the neighbors do not vary too much. The pre-edge region gives valuable information on the average valence and site symmetry of the metal sites. However, it has been shown that the energy position of the centroid is related to the valence and that the integrated intensity is related to the site symmetry, where as the determination of both these quantities depends crucially on the proper isolation of the pre-edge from the edge. One of the advantages of the HERFD-XAS technique is the improved separation of the pre-edge region to the edge jump region, allowing for a detailed analysis of this region. Comparing the pre-edge characteristics from the in-situ data with the references can give valuable information on the local coordination and valence of the active centre.

Another technique which proved to be very helpful in understanding the morphology of the active material is STEM-EELS. This technique combines the strength in spatial resolution of electron microscopy techniques with the possibility to quantitatively identify the chemical nature (i.e. element and valence state) of the measured phase given by EELS. It was observed that in the case of Mn-ZSM-5 samples, as presented in Chapter 3, the presence of the manganese was detected in particular regions of the external surface of the zeolite having a high distribution. Taking into account the loading of these samples, STEM-EELS was the only technique capable of giving information regarding the distribution of manganese over the zeolite crystal. This information does not provide a clear identification of the active phase,

but reduces the number of possible active phases to two possibilities, i.e.,
 (1) the active phase can be the observed Mn phase; and
 (2) the active phase is represented by the invisible highly dispersed Mn phase.

The preparation and characterization of the catalyst materials presented in Chapter 4 revealed the presence of larger manganese-rich and silicon-rich domains. The observed manganese - rich phase suggests the presence of larger manganese-oxide crystals. Taking into account the poor catalytic activity of this material one can conclude that the presence of large manganese domains do not contain the active phases for the generation of α -oxygen species. Based on the above-described discussion one can conclude that we were able to identify the experimental conditions, i.e. the introduction of the metal should be done using ion exchange procedure, while activation of the sample needs to be done using mild conditions in terms of ramp temperature and gas flow conditions, in order to arrive at a catalyst material capable of generating α -oxygen species in a Mn-based zeolite.

In order to see if our observation can be extended to the series of material formed by Me-ZSM-5 (Me = transition metal) a parallel should be made between our materials and a representative of this class of materials; i.e. CuZSM-5.

Looking at the proposed active structure presented until now in the literature, we can observe two main interpretations:

1. A centre based on the two or more types of isolated copper cation sites presented by Wichterlova [1,2] in which the isolated active species Cu^{2+}O^- and Cu^+ are created from two $[\text{Cu}^{2+}(\text{OH})]^+$ by dehydration [3]; or
2. A centre based on the presence of adjacent copper atoms, which can be formed from two $[\text{Cu}^{2+}(\text{OH})]^+$ ions which condense first in a $\text{Cu}^{2+}\text{-O}^{2-}\text{-Cu}^{2+}$ oxocation and then a $\text{Cu}^+\cdots\text{Cu}^+$ pair upon high-temperature [4-6].

However, regardless of the nature of the active species, both models present the same behavior during the NO decomposition reaction. This behavior consists of adsorption of two molecules of NO on $\text{Cu}^+/\text{Cu}^+\cdots\text{Cu}^+$ species generating a molecule of N_2O and a $\text{Cu}^{2+}\text{O}^-/\text{Cu}^{2+}\text{-O}^{2-}\text{-Cu}^{2+}$ species. The formed N_2O can further react, generating N_2 and $\text{Cu}^{2+}\text{O}_2^-/\text{Cu}^{2+}\text{-O}^{2-}\text{-Cu}^{2+}$ which are responsible for the generation of the α -oxygen.

It is to mention that the generation of α -oxygen takes place due to the formation of N_2O and its interaction with the active centre, and not from the direct interaction of NO with the active phase.

From the presented case we can identify that:

- the active phase has a high dispersion – regardless of the isolated or pair proposed model;
- for both models the generation of α -oxygen is accompanied by changes in both the oxidation state and coordination sphere of Cu;
- the removal of α -oxygen as molecular oxygen restores the active phase, making it available for another catalytic cycle.

These observations are in concordance with the proposed factors for Mn-ZSM-5, indicating that, indeed the generation of α -oxygen species is made possible by fulfilling a number of factors, which can be common for Me-ZSM-5 materials.

Concerning the concept presented in Chapter 1, where we discussed the potential analogs of metal ions in ZSM-5 with biological systems, we are able at this point to complete the picture presented there, and given in Table 1.

Table 1. The comparison between the three enzyme systems with ZSM-5 systems. Columns 2 and 6 give the metal atom and cluster size, columns 3 and 7 the redox couple in the reaction, and columns 4 and 8 the main neighbor atom.

Enzyme	Metal	Redox	Main Ligand	Zeolite	Metal	Redox	Main Ligand
sMMO	Fe ₂	2-3	O	Fe-ZSM5	Fe _n	2-3	O
pMMO	Cu ₂	1-2	N	Cu-ZSM5	Cu _n	1-2	O
PSII	Mn ₄	3-4	O	Mn-ZSM5	Mn _n	2-3	O

We can conclude that in the case of Mn-ZSM-5 and PSII a crucial difference is presented by the different redox couple, namely 2-3 for Mn-ZSM-5 versus 3-4 for PSII.

This implies that the closest analogies can be found for the comparison between Fe-ZSM-5 and sMMO.

C. Look into the future of Mn-based zeolites containing α -oxygen species

The studies presented in this PhD-thesis deal with the identification of optimal parameters for the preparation of Mn-containing ZSM-5 zeolites capable of generating α -oxygen species. Once these parameters are identified, the possibilities of usage of these materials are numerous. Based on the history of similar materials like Cu-ZSM-5 and Fe-ZSM-5, Mn-ZSM-5 can be used for hydrocarbon oxidation or SCR reactions.

However, we believe that more applications could be achieved for these types of materials if a larger pallet of zeolite types can be used. In order to demonstrate that not only ZSM-5 zeolite-types are capable to generate α -oxygen species, Mn - containing mordenite (MOR) materials were investigated.

For the preparation of these materials, an identical preparation procedure as Mn-ZSM-5 materials was used (ion exchange), yielding a number of samples whose characteristics are presented in Table 2.

Table 2. Mn-MOR samples prepared using the ion exchange technique, including their sample codes together with the Mn loadings as measured by XRF and Mn/Al ratios.

Sample name	Mn wt%	Mn/Al ratio
Mn-MOR-0.08	0.41	0.08
Mn-MOR-0.12	0.60	0.12
Mn-MOR-0.16	0.82	0.16
Mn-MOR-0.21	1.06	0.21

These samples were exposed to the same treatments as the Mn-ZSM-5 materials (as presented in Chapter 3). It was observed that using the same activation procedure as Mn-ZSM-5 we generate a stable UV-Vis band situated at 21000 cm^{-1} , which is characteristic for the presence of Mn^{3+} . By lowering the oxygen flow from 200 ml/min used during the activation procedure to 20 ml/min we were able to reproduce a dynamic UV-Vis band, which was attributed to the formation of α -oxygen species in Mn-ZSM-5 materials. In the case of Mn-ZSM-5 samples the UV-Vis band has been analyzed with

two main contributions centered at $\sim 16000\text{ cm}^{-1}$ and at $\sim 20000\text{ cm}^{-1}$. In case of Mn-MOR samples the best fit was obtained with these contributions shifted to a lower wavenumber, respectively $\sim 15000\text{ cm}^{-1}$ and $\sim 19000\text{ cm}^{-1}$ (see Figure 1). Due to the large contribution of the 23500 cm^{-1} band the centroid position of the band is shifted to a value of $\sim 19500\text{ cm}^{-1}$. In case of the Mn-ZSM-5 materials this 23500 cm^{-1} contribution was negligible (cf. Figure 5 in **chapter 3**).

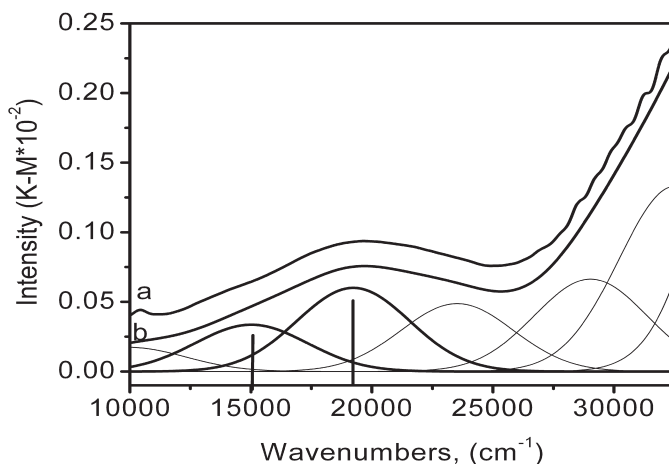


Figure 1. UV-Vis-NIR spectra of the Mn-MOR-0.08 (a) together with the result of fitting (b) and the main contributions of the observed transitions.

The lines indicate the centre of the main contributions for the UV-Vis band, while the Gaussians functions presented in thinner lines are used in order to obtain the final fit of the spectra.

Regardless of the shift that was observed for the Mn-MOR samples, during gas treatment with $\text{N}_2\text{O}/\text{NO}$ this UV-Vis band behaves similar to the Mn-ZSM-5 samples, i.e. the appearance of the band during N_2O treatment and disappearing when NO was put in contact with the sample. Figure 2A present UV-Vis spectra for Mn-MOR-0.21 after 1 h of N_2O treatment (a) and subsequent 1 h of NO treatment (b). Figure 2B compares the total area of the 18500 cm^{-1} UV-Vis band obtained for the Mn-MOR samples loaded with different amounts of Mn and treated in N_2O at 623 K for 1 h.

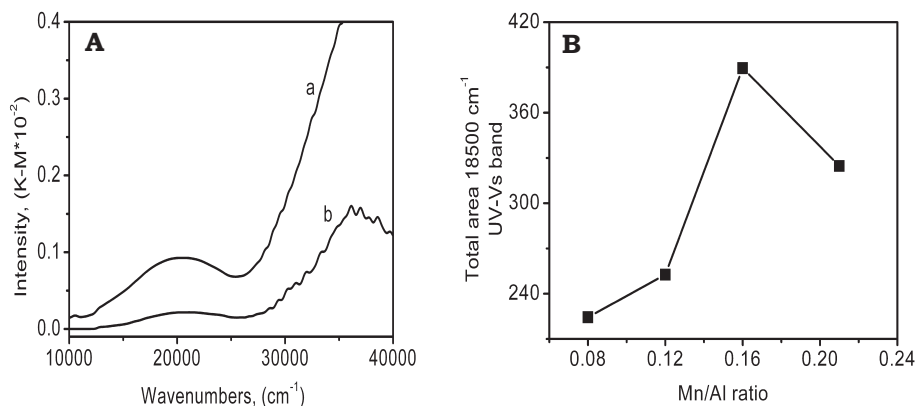


Figure 2. A UV-Vis spectra for Mn-MOR-0.21 after 1 h of N₂O treatment (a) and 1 h of NO treatment (b), B Total area for the UV-Vis band given by the contributions at 15000 cm⁻¹ and 19000 cm⁻¹ as a function of Mn/Al molar ratio in Mn-MOR samples.

These experiments prove that it is indeed possible to generate α -oxygen species in other Mn - containing zeolite types than MFI. Also, it was found that the Mn-species presented in Mn-MOR sample are easier oxidized to Mn³⁺ than in case of Mn-ZSM-5. The shift in the experimental peak position from 18500 cm⁻¹ to 19500 cm⁻¹ suggests that the Mn ions in MOR have a larger crystal field splitting (implying an increased Mn-O bonding strength) than ZSM-5 zeolite, which stabilizes the Mn³⁺ ions in Mn-MOR, with respect to Mn-ZSM-5. This also implies that with the large oxygen flow from 200 ml/min, the α -oxygen species can only be generated in Mn-ZSM-5 because of its reluctance to oxidize its Mn sites. Another conclusion that can be drawn is that the increase of the Mn-loading of the sample will not yield a higher concentration of active species after a critical point. In both cases there was a maximum in the total area of the band at a certain wt.% loading of the sample, for Mn-MOR was this around 0.85 wt.% and for Mn-ZSM-5 was this around 1.3 wt.%.

Acknowledgements

Johnny van Meurs is kindly acknowledged for performing the Mn-MOR experiments. A full description of the experiments is presented in his bachelor thesis: 'An UV-Vis Study on Mn-containing Mordenite', from Utrecht University 2006. Financial support was provided by the Netherlands Organization for Scientific Research – Chemical Science (NWO-CW) and the Netherlands Research School Combination on Catalysis (NRSCC).

References

- [1] J. Dedeczek; B. Wichterlova, *Phys. Chem. Chem. Phys.*, 1, **(1999)**, 629.
- [2] B. Wichterlova; J. Dedeczek; Z. Sobalik; A. Vondrova; K. Klier, *J. Catal.*, 169, **(1997)**, 194.
- [3] S. C. Larsen; A. Aylor; A. T. Bell; J. Reimer, *J. Phys. Chem.*, 98, **(1994)**, 11533.
- [4] M. H. Groothaert; J. A. Van Bokhoven; A. A. Battiston; B. M. Weckhuysen; R. A. Schoonheydt, *J. Am. Chem. Soc.*, 125, **(2003)**, 7629.
- [5] G. T. Palomino; P. Fisicaro; S. Bordiga; A. Zecchina; E. Giamello; C. Lamberti, *J. Phys. Chem. B*, 104, **(2000)**, 4046.
- [6] J. Sarkany; J. L. D'itri; W. M. H. Sachtler, *Catal. Lett.*, 16, **(1992)**, 241.

Samenvatting

De belangrijkste doelstellingen van dit proefschrift zijn:

- (1) Het maken van een geschikt Mn-ZSM-5 materiaal voor het produceren van α -zuurstof en het gebruik hiervan in een katalytische reactie.
De Mn-ZSM-5 materialen zijn bereid via twee routes:
 - (a) de postsynthese methode.
 - (b) hydrothermale synthese.
- (2) Het bepalen van de actieve plaats in de katalyse met behulp van geavanceerde karakteriseringhulpmiddelen. Dit omvat de elektronische structuur en geometrische structuur. Een aantal spectroscopische technieken werden gebruikt, en door interpretatie van de resulterende gegevens kan een gedetailleerd beeld worden geven van de fenomenen die tijdens de katalytische reacties plaatsvinden.

In wat volgt zullen wij de belangrijkste bevindingen samenvatten, de belangrijkste conclusies geven en suggesties doen voor toekomstig onderzoek.

Hoofdstuk 2 introduceert de karakteriseringstechnieken die voor het verzamelen van gedetailleerde informatie over de katalysatormaterialen in deze studie belangrijk zijn. Een fundamentele basis wordt gegeven als achtergrond voor de experimentele hoofdstukken waarin deze technieken zijn gebruikt. Deze omvat kristallografische informatie uit röntgendiffractie (XRD), de elementaire samenstelling van het materiaal uit röntgenfluorescentie (XRF), de oppervlaktetextuur met de roster elektronen microscopie (SEM), de oxidatietoestand met röntgenabsorptie spectroscopie (XAS) en de elektronische overgangen met diffuse reflectie UV-vis spectroscopie (UV-vis). Twee technieken zijn niet standaard en deze zullen meer in detail worden besproken.

Dit betreft:

- (1) Het gebruik van hoge energieresolutie in röntgenfluorescentie detectie van een röntgenabsorptie spectrum (HERFD-XAS). Deze techniek geeft een sterk verbeterde resolutie van het XAS spectrum, dat kan worden gebruikt om de oxidatietoestand nauwkeuriger te bepalen.
- (2) De tweede techniek is het gebruik van de Transmissie Elektronen Microscopie (TEM) voor het meten van een elektronverlies (EELS) spectrum. Met TEM-EELS kan informatie worden verkregen over de aanwezige elementen en hun oxidatietoestand met een plaatsresolutie van 0.5 nm.

Hoofdstuk 3 is een volledig onderzoeksrapport over Mn-ZSM-5 materialen verkregen met de postsynthese methode. Het eerste deel van dit hoofdstuk bespreekt de bereiding en activeringsbehandeling van deze Mn-ZSM-5 materialen gebruikmakend van de ionenuitwisselingsprocedure. Het tweede deel van dit hoofdstuk onderzoekt de katalytische activiteit van deze Mn-ZSM-5 materialen in twee reacties:

- (a) De katalytische decompositie van N_2O
- (b) De oxidatiereactie van NO.

Deze katalytische tests leiden tot de conclusie dat deze materialen N_2O omzetten in N_2 en α -zuurstof, waarbij alleen de N_2 als product detecteerbaar is.

Een lineaire relatie werd waargenomen tussen de Mn belading en de waargenomen katalytische activiteit, voor beladingen tussen de 0.64 en 1.3 gewichtsprocent. De reactiviteit van de geproduceerde α -zuurstof werd bestudeerd via de oxidatie van NO als testreactie. De oxidatie van NO toont aan dat het mogelijk is om deze speciale zuurstofsoort in chemische reacties te gebruiken. De resultaten tonen aan dat α -zuurstof wordt gevormd onder N_2O blootstelling, waarbij tegelijkertijd de coördinatie en de oxidatietoestand van mangaan veranderen.

Gebruikmakend van HERFD-XAS is aangetoond dat de actieve soorten mangaanatomen zich binnen de zeolietkanalen bevinden en dat hun oxidatietoestand veranderd van tweewaardig tot driewaardig, samen met de verandering in hun coördinatie van een viervoudige omringing naar een vijfvoudige. De verwijdering van geproduceerde α -zuurstof brengt de oxidatietoestand (gedeeltelijk) terug van Mn^{3+} tot Mn^{2+} .

De UV-Vis metingen gaven een absorptieband bij 18500 cm^{-1} tijdens de N_2O blootstelling. Uit andere experimenten blijkt dat deze band aan α -zuurstof kan worden toegeschreven. Tijdens NO oxidatie verdwijnt deze 18500 cm^{-1} band, wat een duidelijke aanwijzing is dat de α -zuurstof wordt verwijderd uit het katalysatoroppervlak.

Samenvattend, dit hoofdstuk geeft de succesvolle bereiding van een nieuw Mn-ZSM-5 materiaal wat geschikt is voor de productie van α -zuurstof, die in de toekomst gebruikt zou kunnen worden voor katalytische toepassingen.

Hoofdstuk 4 behandelt de bereiding van Mn-MFI materialen (Mn-ZSM-5 en MnS-1) gebruikmakend van de hydrothermale synthesesmethode. De bereidingsprocedure is geoptimaliseerd uitgaande van een gepubliceerde bereiding. In een poging deze bereidingsprocedure met TEOAH te reproduceren verkregen wij materialen met een slechte kristalliniteit en een slechte reproduceerbaarheid. Door het template molecuul te veranderen van TEOAH naar TPAOH konden wij kristallijne materialen bestaande uit één enkele fase verkrijgen.

Gebruikmakend van XRD kon worden aangetoond dat de materialen de MFI structuur hebben. Met XAS is bepaald dat de gemiddelde oxidatietoestand van het mangaan ongeveer 2.8 was in het geval van MnS-1, terwijl voor Mn-

ZSM-5 een gemiddelde oxidatietoestand van 2.5 werd bepaald. De TEM-EELS spectra lieten zien dat de Mn-ZSM-5 kristallen afwisselende mangaanrijke en siliciumrijke domeinen bevatten, die wijzen op een niet homogene distributie van mangaan over het kristal. Betreffende de katalytische activiteit is aangetoond dat MnS-1 een hoge activiteit voor N_2O decompositie heeft, echter zonder de generatie van α -zuurstof. Als bevestiging voor de afwezigheid van α -zuurstof werd geen activiteit gevonden in de NO oxidatiereactie. In plaats daarvan trad een disproportioneringsreactie op van NO tot N_2O en NO_2 .

Dankwoord

The time to say goodbye has come. There were four years full of new experiences. It was a pleasure to work in the Inorganic Chemistry and Catalysis group of Utrecht University as well as to live in the Netherlands. In the last pages of my PhD thesis I would like to show my gratitude to all the people who had contributed to this work as well as to those who had helped in making this period pleasant and enjoyable.

Bert, my promoter, I thank you for the chance of having a PhD position in your group. We always had a professional relationship and I hope you are satisfied with the results of my research.

Frank, my co-promoter, I am deeply grateful for your support through all these years. It was a pleasure working under your supervision. You introduced me to the mysteries of the X-ray world and helped me to unravel them, one by one.

I am grateful to professor Lobo from the Department of Chemical Engineering, University of Delaware, for his hospitality, during the visit in his department, and for his valuable input that led to the synthesis of the materials presented in Chapter 4.

I could not forget my room mates. I had the luck of knowing and having more colleagues than usual. Jaap, we both remained faithful to our office, while every year we had new colleagues. I thank you for the nice atmosphere and I wish you good luck with your new job. Moniek, although the time we shared office was short and you were very busy with your PhD thesis I thank you for your kind words. Anne, it was a pleasure having you as a room mate. I thank you for the pleasant discussions that we had during the coffee breaks. Marianne, I am sorry that in the last months I let you alone in the office and I wish you success with your research.

My 4 years adventure included many trips to different synchrotrons - Berlin, Grenoble and Hamburg- which I really enjoyed. I like to thank colleagues with whom I shared the 12 hours shifts (especially the night ones): Didier, Pieter, Fernando, Willem, Ingmar, Agnieszka and Alwies. Special thanks to Andy who had the patience to teach me all the “tricks” from Excurv98 program and who had always an open door for me and my questions.

Ad^E, thank you for all the great time that we spend at the synchrotrons.

You always knew how to create a pleasant work environment during the long EXAFS experiments. I enjoyed the long drives to Grenoble and the conversations during the late dinners. Fouad, Ferry, Gerbrand, Jelle, Stefan, Bibi and all the members of the “Katalyse sterren” team, thank you for the great time we had during the NIOK soccer tournaments.

Mulumiri speciale domnului profesor Parvulescu, care m-a introdus in lumea catalizei. A-ti crezut in mine si pentru asta va sunt recunoscator. Un salut calduros prietenilor mei de acasa si din Olanda. Roxana, Ed, Floor si Arjen, ati facut din ultimii 3 ani de stat in Olanda o adevarata placere, in special petrecerile si escapadele noastre spontane. Sper ca indiderent unde vom ajunge sa ramanem prieteni.

Mihai, iti multumesc de sfaturi, vorbe bune si de incurajari, si sper sa ne vedem sa sarbatorim. Nu as putea sa uit fostii colegi de master alaturi de care am impartasit emotiile fiecarui examen si cu care sper sa mai am ocazia sa ma revad. Asa ca :”Ramane cum am stabilit!”.

Nu in utimul rand as dori sa multumesc Elenei si Cristinei, fara de care nu as fi putut exersa limba romana.

Mulumesc din suflet parintilor mei. Taticu, mereu m-ai incurajat sa-mi urmez visul si sa fac ceea ce imi place indiferent unde. Mami, stiu ca ai trecut prin mari emotii inca din prima zi cand am inceput acest drum. Iti multumesc ca ai avut incredere in mine. Surioarei mele cu care am impartasit pasiunea pentru chimie iti multumesc ca m-ai incurajat sa-mi urmez visul.

Ultima, dar nu in cele din urma as dori sa multumesc unei persoane care mi-a fost sufleteste alaturi acesti ani si care m-a sustinut neconditionat. Flory, a venit timpul ca visele noastre sa devina realitate.

Daniel

Curriculum Vitae

Cornel Daniel Radu was born on 28th of May 1979 in Ramnicu Sarat, a small town situated in the Eastern part of Romania. In 1997, he graduated from the mathematics-physics section at “Alexandru Vlahuta” high school. From autumn of the same year, he studied Chemistry at Bucharest University, graduating in 2001. Two years later, in June 2003, under coordination of prof. Vasile Parvulescu he obtained his M.Sc. degree in Catalysis and Catalytic Processes at the same university. During his master he studied asymmetric sulfoxidation of thiol-pyrimidine compounds over titanium-silicalite Ti-SBA-15 and Ta/Si catalysts. He was also involved in collaboration with the group of Zdeněk Sobalík from the J. Heyrovsky Institute of Physical Chemistry, Czech Republic, where he used FTIR spectroscopy in order to investigate acidic properties of Ru-BEA zeolite and reveal the external acidic properties of Ir-BEA zeolite used in fine chemical processes.

In 2003 he enters as a PhD student in the Inorganic and Catalysis Group at Utrecht University under the supervision of Bert Weckhuysen and Frank de Groot. His research included the synthesis of Mn-ZSM-5 materials capable to reproduce a highly desired property of some enzymes, i.e. the generation of α -oxygen species, and determination of the electronic structure, geometric structure and its dynamics by means of advanced characterisation techniques.

The results of his research are described in this PhD thesis and published in scientific journals.

List of Publications and Presentations

Publication List

- ◆ Mn and Fe ions and oxo-clusters in ZSM-5: Pushing the limits of X-Ray spectroscopy, D. C. Radu, P. Glatzel, W. M. Heijboer, H. J. Bitter, F. M. F. de Groot and B. M. Weckhuysen, *Studies in Surface Science and Catalysis* 2007, *in press*.
- ◆ Investigation of acidic properties of Ir-*BEA zeolites by Py-, DTBP-, and Qu-FTIR, D. C. Radu, S. M. Coman, V. I. Parvulescu, D. E. De Vos, P. A. Jacobs, Z. Sobalik, *Studies in Surface Science and Catalysis*, 2005, 158, 909-916.
- ◆ Hydrogenation of prostaglandin unsaturated ketones over Ru-containing *BEA zeolites, S. N. Coman, D. C. Radu, V. I. Parvulescu, Z. Sobalik, D. E. De Vos, P. A. Jacobs, *Studies in Surface Science and Catalysis*, 2004, 154 2696-2702.
- ◆ Chemoselective oxidation of 2-thiomethyl-4,6-dimethyl-pyrimidine and 2-thiobenzyl-4,6-dimethyl-pyrimidine over titania-silica catalysts, D.C. Radu, V. Parvulescu, V. Câmpeanu, E. Bartha, A. Jonas, P. Grange and V. I. Parvulescu *Applied Catalysis A: General*, 2003, 242, 77-84.
- ◆ Oxidation of 2-thiobenzyl-4,6-dimethyl-pyrimidine with hydrogen peroxide over Mo oxides, Mo suboxides and mixed Mo-Sb oxides catalysts, D. C. Radu, V. Campeanu, F. Bertinchamps, E. M. Gaigneaux and V. I. Parvulescu, *Catalysis Communications*, 2003, 4, 5-9 .
- ◆ Oxidation of methyl-propyl-thioether with hydrogen peroxide using Ti-SBA-15 as catalyst, D.C. Radu, A. Ion, V. I. Parvulescu, V. Campeanu, E. Bartha, D. T. On, S. Kaliaguine, *Studies in Surface Science and Catalysis*, 2003, 146, 609-612.
- ◆ Stereoselective oxidation of 2-thiomethyl-4,6-dimethyl-pyrimidine and 2-thiobenzyl-4,6-dimethyl-pyrimidine over titania-silica catalysts, R. Mihaie, D. C. Radu, V. Parvulescu, V. Campeanu, E. Bartha, M. T. Caproiu, A. Jonas, P. Grange and V. I. Parvulescu page 7, Proc.- "4th World Congress on Oxidation Catalysis, Vol.II, "Ed.DECHEMA e.V, 16-21 September 2001 Berlin/Potsdam, Germany

Oral Presentations

◆ Revealing the reaction mechanism of combined N_2O decomposition/
NO oxidation reactions on Mn-MFI systems by spectroscopic means

D.C. Radu, B. M. Weckhuysen and F. M. F. de Groot

Netherlands' Catalysis and Chemistry Conference VIII, 5-7 March 2007,
Noordwijkerhout, the Netherlands.

◆ Reactive oxygen in Mn-MFI Zeolite

D.C. Radu, F. M. F. de Groot, J. H. Bitter, B. M. Weckhuysen

2nd CONCORDE Conference, Nucleation, growth, microstructure and
matrices for creating highly dispersed redox oxide catalysts in Oxidation
Catalysis, 26-28 January 2006, Thessaloniki, Greece.

Poster Presentations

◆ Mn and Fe ions and oxo-clusters in ZSM-5: Pushing the limits of X-
Ray spectroscopy

D. C. Radu, P. Glatzel, W. M. Heijboer, H. J. Bitter, F. M. F. de Groot and B.
M. Weckhuysen

15th International Zeolite Conference, 12-17 August 2007, Beijing, China.

◆ A UV-Vis and XAFS study of the active center in Mn-ZSM-5

D. C. Radu, H. J. Bitter, F. M. F. de Groot and B. M. Weckhuysen

Netherlands' Catalysis and Chemistry Conference VII, 6-8 March 2006,
Noordwijkerhout, the Netherlands.

◆ Investigation of acidic properties of Ir-*BEA zeolites by Py-, DTBP-,
and Qu-FTIR

D. C. Radu, S. M. Coman, V. I. Parvulescu, D. de Vos, P.A. Jacobs, Z.
Sobalík, 3Rd International FEZA Conference, 23-28 August 2005, Prague,
Czech Republic.

◆ New synthesis routes of Mn-ZSM-5 and MnS-1 Zeolites

D. C. Radu, R. F. Lobo, B. M. Weckhuysen and F. M. F. de Groot

Netherlands' Catalysis and Chemistry Conference VI, 7-9 March 2005,
Noordwijkerhout, the Netherlands.
